University of California
Los Angeles

# On the Characterization and Exploitation of Wireless Channels

A dissertation submitted in partial satisfaction
of the requirements for the degree
Doctor of Philosophy in Electrical Engineering

by

**Robert Dale Thrasher**

2004

The dissertation of Robert Dale Thrasher is approved.

Kirby Baker

Kung Yao

Babak Daneshrad

Greg Pottie, Committee Chair

University of California, Los Angeles

2004

*To my mother, father,*

*wife, and daughter*

# Table of Contents

# List of Figures

# List of Tables

# Acknowledgments

I would like to express my love and thanks to my parents who recognized that I was one of those born engineers. In addition to doing the usual child raising activities that parents perform, they also were attuned to my particular varied interests and would partially (or wholly) subsidize some of my projects. Among my interests was an interest in the electronics field, which I pursued at my leisure. Observing this interest, my parents suggested I should enroll in an electrical engineering program in college. So naturally, I enrolled and earned a Bachelors and Masters in Civil and Structural Engineering from the University of California at Irvine. But my later career path and pursuits led me in a different and more rewarding direction back to the electronics field in the development of Global Positioning receivers. Thanks Mom and Dad, you should have told me to be a Civil Engineer instead! Anyway, I have finally conceded that they were right after all.

The main reason I started on this path in the first place was due to the inspiration of my wife. I have always admired my lovely wife Rosie for her beauty, charm, and brains. She received her Ph.D. in Mathematical Probability and Statistics from the University of California at Irvine. In fact, our mutual attendance at UCI is partly why we met. So, as a consequence of her inspiration and my own enthusiasm for the subject of electrical engineering, I embarked on this program with her full support. Her support through this program has continued, unabated, in every dimension. From supporting the family with her job as a statistician, to proofreading this dissertation, her support has been tangible and unwavering. Sometimes she even helps with statistics questions. Too many nights I have started a conversation with: "I have a statistics question for you." I don't think I'll have too many of those questions hereafter.

I would also like to express my thanks to the thesis committee and all of my instructors over the course of my studies. I have benefited greatly from their desire to provide a rigorous and uncompromised level of instruction and research. They are truly what make UCLA the great institution that it is.

Finally, I owe a great deal of credit and appreciation to my advisor Greg Pottie for his support. From the time I first visited him in 1999 until the culmination of this effort his encouragement, understanding, expertise, guidance, and concern were freely offered.

# Vita

| | |
|---|---|
| 1958 | Born, Syracuse, New York, USA. |
| 1981 | B.S. (Engineering), UCI, Irvine, California. |
| 1981–1983 | Programmer, Structural Mechanics Associates, Newport Beach, California. |
| 1985 | M.S. (Structural Engineering), UCI, Irvine, California. |
| 1983–1996 | Systems Engineer, Interstate Electronics Corp., Anaheim, California. |
| 1996 | M.S. (Electrical Engineering), UCI, Irvine, California. |
| 1996–1999 | Systems/Software Department Manager, Axiom Navigation, Anaheim, California. |
| 1999-2001 | Software Manager, NavCom Inc., Redondo Beach, California. |
| 2001–present | Graduate Student Researcher, UCLA, Los Angeles, California. |

# Publications

Robert Thrasher and Gregory Pottie, "Performance of OFDM in High-Mobility Environments", *Proceedings SPIE Annual Meeting, Advanced Signal Processing*

*Algorithms, Architectures, and Implementations XIII*, vol. 5205, pp. 21-27, San Diego, CA, USA., August, 2003.

Abstract of the Dissertation

# On the Characterization and Exploitation of Wireless Channels

by

**Robert Dale Thrasher**

Doctor of Philosophy in Electrical Engineering

University of California, Los Angeles, 2004

Professor Greg Pottie, Chair

The analysis and subsequent design of wireless systems depend on a comprehensive understanding of the channel through which the transmissions will pass. In this thesis we study the modelling of wireless channels from the phenomenological perspective. In other words, we begin with an analysis of the physical underpinnings and proceed to derive our models as directly as possible from their physical roots. We also consider the effect of these models on several channel equalization strategies. The strategies considered are OFDM, diversity combining for a RAKE receiver, and MLSE (by sequential detection).

# CHAPTER 1

# Introduction

## 1.1 Introduction

In the sciences and engineering, when confronted with a particular phenomena, the natural question to ask is if we can explain the phenomena by some mathematical model. Prior to the development of such a model it is necessary to make many observations of the phenomena in question under controlled conditions (if possible). Then, after assembling the necessary repertoire of underlying theory, an attempt may be made to find an "appropriate" mathematical model. An appropriate model is one that is able to make accurate predictions in the absence of additional observations under unique conditions. This prediction-making capability is an indispensable requirement since it will form the foundation upon which additional theories or applications may be built. As engineers, although we are primarily interested in applications, we must also have a clear understanding of the phenomenological environment in which the application must operate. The selection of an appropriate mathematical model will provide the phenomenological environment useful to application development. In this thesis we will be investigating and developing the mathematical models used in describing wireless channel models and also consider the implications of those channel models and, better yet, how they may in some cases be exploited.

## 1.2 Electronic Communications - A Motivation

The desire to "telecommunicate", that is, to communicate over large distances has been present for as long as one person has wanted to communicate with another. Consequently, the digital telecommunications revolution has been largely been motivated by the desire for clear voice connections over large distances. More recently, driven by the ascendency of the electronic computer, telecommunications between networked computers has motivated further improvements in digital communications to accommodate ever-higher bandwidth needs. From a philosophical perspective, the desire to telecommunicate is driven by the desire for "synchronicity." By synchronicity we mean that information that is collected by remote sensors may be observed almost simultaneously either by a central decision-making node or in a distributed way by the entire network. Additionally, the decisions of the central or distributed system can be disseminated with similar simultaneity followed by synchronized execution. The reason for this desire for synchronicity is that we live in a competitive world and whether the particular subject be business or military competition (war), the competitor who can perceive accurately and provide an appropriate response most rapidly will increase his odds of survival.

Initially, computer applications were largely restricted to the scientific and military communities. Such information was often rather condensed in comparison to the data types we will mention shortly. Then, as computational speeds increased, computers were perceived as useful in business applications which process voluminous amounts of data. Applications of these more capable machines enabled increases in economic productivity resulting from the automation of what were previously routine human tasks. Once computers became indispensable in the business/military context, the attendant desire to network larger numbers of

computers necessitated the development of the means to transfer data over large distances either by telephone networks or satellite "bent-pipe" methods. These developments were, in turn, spurred by the geographic distribution of databases.

At these larger distances it was impossible to reliably communicate simply by a direct conversion of the sampled data to symbol decisions. In order to interface reliably with the physical medium it became necessary to develop means to compensate for noise, self-interference and echo-cancelling (as necessary). These methods are collectively known as channel coding and equalization. The choice of such methods is inherently dependent on the natural medium over which the electronic information is transmitted. This thesis will specifically focus on the wireless medium to the purpose of advancing our knowledge of this medium.

### 1.2.1 Communications Networks

Many similarities exist between the area of wireless communications and the area of wired communication networks. While there are many similarities, many differences exist as well. It would be safe to say that in this area we have a greater degree of complexity in designing wireless systems due to additional considerations not present in the wired systems design domain. Such considerations include the cost of spectrum along with the attendant governmental control of spectrum allocation, possible issues associated with base station antenna siting, the requirement for fundamentally different equalization approaches (with respect to already-existing approaches for wired equalization), and energy and power considerations of wireless networks to name a few. As we can see, some of the issues mentioned are theoretical while others are of a more pedestrian nature. Nonetheless, all must be adequately addressed to successfully deploy a wireless network.

Initially, computer to computer file transfers were only capable of delivering rather small data-file payloads. Then, as equalization methods improved with the attendant increased transmission speeds, larger volumes of data were able to be transferred. This development led to the idea that data could be shared between multiple computers without significant competition for bandwidth. In order for this development to be realized, the concept of network protocols had to be developed which we will now discuss.

The concept of a network protocol was developed to provide a systematic means to transport data from one application to another application hosted on another computer within a network of computers. As the most ubiquitous network protocol, TCP/IP[1] has been applied to both wired and wireless networks. This protocol was developed with the idea in mind that an almost limitless numbers of computers (or nodes) would be interconnected. With this goal in mind, it was recognized that direct interconnection between all computer pairs within the network would be impossible. Since each computer would have a limited number of connections to other computers, each network node would have to provide the facility to "route" data packets coming from a neighboring node to a destination node. Hence, a fundamental characteristic of a network protocol is that there must exist some way to provide packet routing to the destination.

The TCP/IP network protocol is organized as a set of functional "layers." The purpose of this functional layering is to organize the functions into a logical and modular hierarchy. Each layer presents an interface representing the allowable functions which may be accessed by the superior layer. The lowest layer is known as the physical layer which simply describes the point-to-point transmission over the physical media (e.g. CDMA, OFDM, etc.). The next layer is the

[1]The acronym TCP/IP stands for Transport Control Protocol/Internet Protocol.

Data Link layer and is divided into two sub-layers. The Medium Access Control (MAC) sub-layer controls the access to the physical layer. Consequently, for each different physical transmission protocol, a unique MAC layer is required. The Logical-Link control sub-layer controls frame synchronization, flow control and error checking. Next, the Internet Protocol/Internet Control Message Protocol layer provides services by which individual data packets may be transmitted over the network without any guarantee as to the reliability or correctness of the data transmission - this task is reserved for the next layer. This layer is also responsible for providing an "intelligent" method for routing data packets by accepting a packet from an adjacent node and attempting to forward that packet to another adjacent node which is closer to the packet's destination. The next layer is actually composed of two parallel functions known as User Data Protocol (UDP) and Transmission Control Protocol (TCP). The UDP provides direct access to the lower IP layer with all its limitations. The UDP interface may be used as a means for development of new network systems without the overhead that would be involved involved if all layers were present. The purpose of the TCP is twofold. First, it creates a reliable transport mechanism that guarantees all packets are correctly delivered to the destination. Second, TCP provides, what appears to the user as, a "virtual circuit" capability. At the user level, a collection of data packets may be cumbersome to work with but the TCP's job is to reassemble the data packets (even though they may take different routes through the network) so that to the user it appears that a direct connection exists between the source and destination nodes. Finally, the highest layer is the application layer. Within the application layer is hidden all the application-specific details such as data compression and encryption. Examples of specific applications are the well known TELNET (a terminal emulation program for connecting with a remote node) and File Transfer Protocol (FTP) (a program for transferring files between

nodes) applications.

### 1.2.2 A Vision for Communications in the Future

Having made this cursory review of our past and present we may ask what holds for the future in the field of communications. At this point it seems to be clear that it will be one of revolution followed by evolution. That is, as new theoretical breakthroughs are made that enable substantial performance increases in a particular technological area for similar cost, we can expect new applications to be developed that will eventually fully utilize whatever new performance capacity exists. Furthermore, in keeping with the spirit of evolution, competing technological solutions will be vetted based on a combination of cost/benefit, time-to-market, and marketing muscle and ingenuity. A prime example is the competition in the personal communications market between land-based infrastructure and satellite-based. While the land-based solution has conquered this market, the satellite-based solution has retained a small, but relatively safe, niche.

So what can we say about the future of communications? Presently, the trends in consumer electronic appliances appears to be on an evolutionary track as we mentioned above. In other words, what we can expect from this point forward (until the next technological breakthrough) is continued integration of communication capabilities such as telephony, internet, GPS, etc., into single handsets. A field which has largely been untouched by these evolutionary advances in communications has been in the area of home automation. While some products exist, there has not been a large-scale adoption of this technology within the home. This is partly due to the lack of infrastructure penetration within the home environment. Penetration is largely limited to PC's with internet connectivity - perhaps including wireless connectivity to the home network along with similar

connectivity with hand-held devices.

When we consider such an application as home automation, the larger picture we see here is that of the increasing pervasiveness of communications and computing. To a large degree this vision will be realized by the application of very short-range wireless communication devices which provide the "last meter" of connectivity to either more capable wireless or wired telecommunication backbones. Fulfillment of this vision will also be aided by converting from the present last mile wired solutions to optical which will enable increased bandwidth for new communications capabilities such as video telephony.

From the perspective of technological advances required to enable the trends mentioned above, we note, for example, that there are possible breakthroughs on the horizon in the area of optical computing. This will lead to a marked improvement in the power efficiency of computing. This improvement in computational efficiency can be harnessed by applying it to implement some of the more effective, but presently computationally complex, equalization strategies. Furthermore, we are seeing advances in the development in high frequency analog components [YL00] that will allow spectrum formerly considered "junk" to be useable for "last meter" wireless applications.

## 1.3 Channel Characteristics of the Wireless Communications Mediums

Having motivated the need for the development of mathematical models for the wireless medium we would now like to consider what are some of the properties of wireless channels. There are an incredible variety of environmental scenarios that we need to consider. To begin with, there are the indoor, urban, suburban,

and mountain environments. Then there are the various complications that may be involved in each of the previous basic environments. We could consider walls, floors, cubicle partitions, foliage, weather events, just to name a few. Then there are the mobility considerations such as fixed, moderately or highly mobile. Finally, we have to consider the effect of carrier frequency. As result of this vast combination of environments and operational scenarios it would be ideal if we could distill the effects of these environments for the purposes of model-building. In short, this may be done and we have attempted to depict this classification in Fig. 1.1.

| Vehicle Dyn. / Symbol Size | "Low" Dynamic | "High" Dynamic |
|---|---|---|
| "Long" Period | Frequency Non-selective Slowly Fading | Frequency Non-Selective Fast Fading |
| "Short" Period | Frequency Selective Slowly Fading | Frequency Selective Fast Fading |

Figure 1.1: Fundamental Channel Classifications

In the case of mobility, the nature of the fading rate is determined by the required interval between training packets to support a minimum of fading distortion. In other words, a high fading rate channel requires that training packets come at frequent intervals with respect to data packets. In the case of the channel impulse response (CIR) characteristics the first branch is determined by the bandwidth of the transmitted data or, equivalently, by the symbol period. From

this we can determine if the channel possesses a flat-fading or time-dispersive characteristic. Within the time-dispersive characteristic, we can further sub-characterize a channel as either having a short or long CIR (as measured in samples of delay) and whether the impulses are clustered or not. In the next chapter we will return to this subject and provide more concrete definitions, but for now we will summarize by saying that it is the choice of transmission signal characteristics that determine the appropriate choice of channel model.

## 1.4 Primary Equalization Methods In Wireless Communications

Depending on the channel characteristics likely to be present for a particular application, there are a variety of equalization methods that can be successfully employed. In digital communications the term equalization simply refers to the method by which the signal processed by a receiver obtains an estimate of the transmitted data. To accomplish this, there are essentially four approaches we may take. There are a large number of variations on these methods, but the fundamental ones are: linear equalization (LEQ), decision-feedback equalization (DFE), maximum-likelihood sequence estimation (MLSE), and orthogonal frequency division multiplexing (OFDM). In this thesis we will apply the OFDM and MLSE approaches to specific channel models. Furthermore, the approaches we have mentioned here are applicable to single-antenna systems. Consequently, we will not be considering multi-antenna methods such as multiple-input multiple output (MIMO).

There are two basic forms of linear equalization depending on the criterion used in designing the linear filter within the receiver. The first form, as shown

in Fig. 1.2, simply performs a channel inversion in the frequency domain. If we assume a channel normalized to unit energy, the noise energy output from the equalizer is given as:

$$\sigma_n^2 = \frac{TN_o}{2\pi} \int_{-\pi/T}^{\pi/T} \frac{d\omega}{X(e^{j\omega T})} \tag{1.1}$$

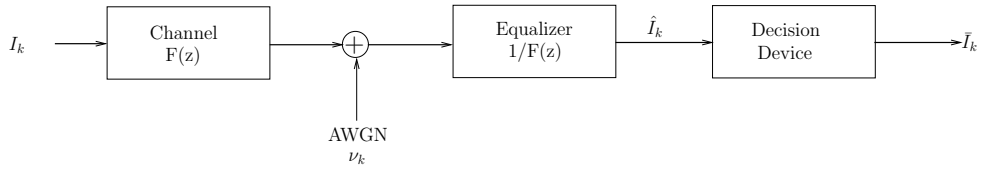


Figure 1.2: Channel Equalization by Channel Inversion (Zero Forcing)

where $X(z) = F(z)F^*(z^{-1})$ and $F(z)$ is the z-transform of the sampled CIR $f_n$. The SNR for this equalizer can be expressed as:

$$\gamma_\infty = 1/\sigma_n^2 \tag{1.2}$$

Assuming we have obtained an accurate estimate of the channel, computing the SNR within an operational receiver is usually done by computing the average of the squared difference between the decisions and the input to the decision device and taking the ratio with the average received signal power. The SNR may also be obtained using equation (1.1) if we have an accurate channel estimate. It is clear that this equalizer will seek to compensate by providing a compensating gain such that the overall transfer function from input to output will exhibit a flat frequency response. Because of this, if the sampled (also known as the folded spectrum) $X(e^{jw})$ contains any spectral zeros then the noise power which exists at these frequencies will have the same gain applied as was used to normalize the corresponding signal at that frequency. Consequently, when deep depressions

exist in the sampled spectrum $X(e^{jw})$ we can expect the resulting SNR to be quite low. For this reason, linear equalization by channel inversion is rarely used.

The second form of linear equalization involves invoking the minimum mean square error (MMSE) criterion. Optimal equalization by this method requires the determination of an infinite-length transversal filter for equalization. Since this is clearly impractical, the next best approximation would be to choose a filter of some practical length which performs nearly as well as the infinite-length filter. This can be done by choosing the filter tap weights such that we minimize the performance measure:

$$J(K) = E|I_k - \hat{I}_k|^2 = E|I_k - \sum_{j=-K}^{j=K} c_j v_{k-j}|^2 \tag{1.3}$$

where $v_k$ is the received signal, $I_k$ and $\hat{I}_k$ represent the transmitted and estimated data respectively, $c_j$ is the set of tap weights in the equalizer, and $K$ determines the length of the equalizing filter. The minimum of $J(K)$ occurs when the estimation error $I_k - \hat{I}_k$ is orthogonal to the signal samples. This leads to the following set of simultaneous equations (in matrix form):

$$\Gamma C = \zeta \tag{1.4}$$

Where $\Gamma_{ij} = x_{i-j} + N_o\delta_{ij}$ for $(|i-j| \leq K)$ and $\Gamma_{ij} = 0$ otherwise. Also $\zeta_i = f^*_{-i}$ for $(-K \leq i \leq 0)$ and $\zeta_i = 0$ otherwise. Finally, $x$ is the autocorrelation of $f$. The MMSE tap coefficients are found by solving equation (1.4) for $C_{opt}$. The resulting MMSE is:

$$J_{min}(K) = 1 - \zeta^H \Gamma^{-1} \zeta \tag{1.5}$$

Where the $H$ represents the Hermitian transpose. As the number of taps ap-

proaches infinity, the limiting MMSE is:

$$J_{min} = \frac{T}{2\pi} \int_{-pi/T}^{pi/T} \frac{N_o}{X(e^{j\omega T}) + N_o} d\omega \tag{1.6}$$

There are a couple of remarks we can make at this point. The first is that the set of "optimal" tap coefficients is specific to the chosen length of the filter. Secondly, we note that for long filter lengths and high SNR conditions, the MSE criterion yields tap coefficients which are close to those obtained by channel inversion (provided the channel is invertible). Consequently, under poor channel conditions characterized by dead-zones in the sampled spectrum, linear equalization by the MSE criterion will be nearly as poor as under the channel inversion approach. Consequently, this also is an infrequently used method for equalization. As we proceed, we shall see that "optimal" must be understood in the context of the particular equalization strategy and optimality criterion being invoked.

As a final remark, the equalizers we have discussed so far concern those which sample at the symbol rate. However, in spite of knowing the optimal equalizer coefficients, if the sampling instant in the receiver does not correspond quite accurately with the symbol transition times at the receiver the ISI will result in a substantial "closing of the eye." The performance losses can often be substantial, perhaps 10 dB or more. The residual ISI in this case will result in an irreducible error floor which is a situation that we strive to avoid. To combat this situation fractionally spaced equalizers (FSE) were developed. The FSE samples the received signal at least as fast as the Nyquist rate - a rate of twice the Nyquist rate is frequently used. The resulting sampled signal is then passed through the FSE. The output of the FSE is then sampled at the symbol rate to produce final or tentative decisions for further processing as may occur in the DFE or MLSE equalizers. The advantage of this approach is that the equalization occurs

before the aliasing that occurs due to symbol-rate sampling. As a result, the FSE can compensate for an arbitrary timing phase. We will now move on to consider other fundamental equalization methods which typically provide better performance than those we have considered so far.

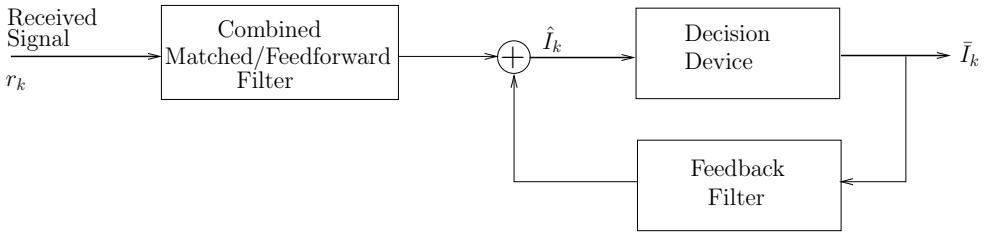


Figure 1.3: The Decision Feedback Equalizer

The decision-feedback equalizer (DFE) has proven to be a substantial improvement over the LE. Fig. 1.3 depicts the DFE. From the figure we note that the DFE is comprised of a feedforward filter, feedback transversal filter, and a decision device. We also observe that the decisions are fed back to the feedback filter (hence the name) and used to cancel the post-cursor response. Because the cancellation of the post-cursor energy results is a performance loss, the ideal selection of feedforward coefficients will tend to result in an overall minimum-phase impulse response of the channel and feedforward filter combination. The reason for this tendency (as SNR approaches infinity the tendency is strengthened) is that of all filters having the same magnitude frequency response, minimum-phase impulse responses compress the most energy closest to the delay origin and show a monotonic decay with increasing delay. As a result of this stipulation, we can see that we may compute the feedforward coefficients prior to the feedback coefficients. With a little algebraic manipulation we note that the feedforward coefficients of the DFE are the same as those determined for the MMSE LE (provided they are of the same length). The feedback taps are given by the following

equation:

$$fb_k = -\sum_{j=-K_1}^{0} ff_j f_{k-j} \tag{1.7}$$

Where $ff$ is the feedforward vector and the length of the feedback tap vector $fb$ is (ideally) at least as long as the channel so that all the post-cursor response will be cancelled. The performance (assuming an infinite-length feedforward filter) is given by:

$$J_{min} = exp\left\{\frac{T}{2\pi}\int_{-pi/T}^{pi/T} \ln\left[\frac{N_o}{X(e^{j\omega T}) + N_o}\right] d\omega\right\} \tag{1.8}$$

It is interesting to compare this performance measure with that of the MSE LE. In the DFE's performance measure we notice that the logarithm effectively "dampens" those portions of the channel which exhibit poor performance in contrast to the MSE LE. Another item of note is the fact that equation (1.8) assumes correct decisions are available to the feedback filter. Clearly, in a practical implementation, we are not going to make correct decisions 100% of the time. Because of this we can expect that there will be a performance penalty with respect to correct decision feedback. The degree of this degradation depends on the magnitudes of the feedback coefficients. Large magnitude coefficients correlate positively with large degradation.

The DFE belongs to a class of equalizers known as the nonlinear equalization class. In the case of the DFE, since the decision device is itself nonlinear and incorporated within the loop filter, the overall equalization process is itself nonlinear. The maximum-likelihood sequence estimation (MLSE) approach to equalization is also a part of this class. The MLSE approach is a substantial departure from the LE or DFE we considered previously in that, rather than performing symbol-by-symbol detection, the MLSE algorithm performs detec-

tion of an entire sequence. MLSE is also referred to as trellis decoding. The discrete-time channel model is conceived as a transversal filter which takes the information sequence as an input and outputs (to the receiver) a linear combination of the shift-register contents. The possible states for this shift register may be enumerated. Given a symbol constellation size of $b$, we note that from a particular state there are only $b$ possible states to which we may transition. Tracing the possible transitions from all states at the current time step to the corresponding possible states at the subsequent time step can be used to produce a trellis diagram. In other words, when we have finished this process we will have produced a "map" showing all the allowable state transitions. The process of decoding the received information from the received samples using the trellis diagram is called trellis decoding.

The process of MLSE is then one of estimating the state of a shift register (or finite state machine) at each time step. The algorithm which has seen the widest use in performing MLSE is the Viterbi Algorithm (VA). It is not our purpose at this point to fully describe the operation of the VA since the details this may be easily obtained [Pro95a], but we shall summarize in the following discussion. MLSE, by definition, obtains an estimate of the information sequence which maximizes the likelihood function given the corresponding set of received samples[2]. The likelihood function we are interested in is the joint conditional probability density given below (due to AWGN):

$$p(r_N|I_p) = \left(\frac{1}{2\pi N_o}\right)^N exp\left(-\frac{1}{2\pi N_o}\sum_{k=1}^{N}\left|r_k - \sum_{n=0}^{p} I_n h_{k-n}\right|^2\right) \tag{1.9}$$

where $r_k$ represents the $k^{th}$ received sample (of which there are $N$), $I_n$ is the $n^{th}$ transmitted information symbol (of which there are $p$), and $h_{k-n}$ is the CIR up

[2]In order to obtain an estimate of the transmitted sequence it is necessary to receive at least as many input samples, preferably in excess by several times the channel length.

to the Viterbi decoder at time $n$ and delay $k$. It is easily seen that finding the optimal estimate of the transmitted sequence by maximizing equation (1.9) is equivalent to minimizing the following:

$$\sum_{k=1}^{N} \left| r_k - \sum_{n=0}^{p} I_n h_{k-n} \right|^2 \tag{1.10}$$

In other words, given the sequence of $N$ samples (where $N > p$), the optimal estimate of $I_p$ is obtained by choosing the sequence which results in the minimum Euclidean distance between the received sample sequence and output sequence corresponding to our estimate. All that remains is to obtain an algorithm which is efficient in performing the aforementioned choice.

The Viterbi algorithm has found a widespread use due to its relative ease of implementation for decoding of relatively short delay systems. The VA works by selecting the path through the trellis which has the least path metric (the path metric is initially zero for all states). At each step in the process, the VA computes branch metrics corresponding to each branch departing from each state. The branch metric is computed by finding the Euclidean distance between the received sample corresponding to this branch time step and the computed channel output given the hypothetical branch symbol and path history:

$$\left| r_k - \sum_{n=0}^{p} I_n h_{k-n} \right|^2 \tag{1.11}$$

Recalling our earlier description of the trellis diagram, there are $b$ branches departing each state and $b$ merging into each subsequent state. So, tentative path metrics are computed corresponding to each possible branch by adding the branch metric corresponding to branches departing from a given state with the common path metric for that state. Since there will be $b$ branches merging into each state and only one possibly correct branch, the VA makes a choice as to the most likely correct branch. This is done simply by selecting the merging branch

| Channel Length | Channel Impulse Response | MLSE Loss | DFE Loss |
|---|---|---|---|
| 3 | 0.50 0.70 0.5 | 2.3 dB | 6.1 dB |
| 4 | 0.38 0.6 0.6 0.38 | 4.2 | 8.4 |
| 5 | 0.29 0.5 0.58 0.5 0.29 | 5.7 | 10.8 |
| 6 | 0.23 0.42 0.52 0.52 0.42 0.23 | 7.0 | 12.8 |

Table 1.1: MLSE and DFE Loss for Worst Case CIR

with the least tentative path metric associated with it. The other branches (and hence tentative paths) are rejected. This process is carried out for all possible states. Ultimately, since there will be a limited amount of memory reserved for maintaining the possible trellis paths it becomes necessary to output a decoded symbol. This is accomplished by selecting the state at the present time step with the least path metric and following the path which traverses the accepted branches back to the start of the path memory. The process of following this path is known as traceback and inevitably leads to the initial branch which is released as the decoded information symbol.

The performance of MLSE for equalization is most directly related to the $d^2_{free}$ of the channel which we will define and discuss in Chapter 5. Having said that, we note that MLSE provides the best performance for equalization for non-diversity systems. In Table 1.1 we compare the performance of MLSE decoding with DFE. In the table we selected channels having the following lengths and tap coefficients that were determined to result in the worst possible MLSE loss for that length of channel.

The modulation/equalization methods we have considered so far spread their energy indiscriminately over the entire allocated bandwidth. However, the equal-

ization performance for channels which exhibit nulls tends to suffer due to the noise-enhancing effect within the null regions. Given this weakness of the methods considered so far, a sensible question we might ask is whether it is possible to subdivide the total allocated bandwidth so that we might, for instance, equalize our way around the dead-zones. Such is the case with the final fundamental equalization method we shall consider. The method is known as orthogonal frequency division multiplexing (OFDM).

In Fig. 1.4 we have presented a block diagram of an OFDM transceiver. An OFDM transmitter takes a block of $N$ symbols to be transmitted and performs an inverse discrete Fourier transform (IDFT), in effect creating a set of $N$ orthogonal QAM-modulated carriers. Then the resulting block is cyclically extended (i.e. using samples from the beginning of the "resulting" block) by $L$ samples where $L$ is at least as long as the CIR. The cyclically-extended block is then transmitted. Assuming adequate timing and frequency synchronization with the received signal, the receiver then collects $N + L$ samples and discards the first $L$ samples. A discrete Fourier transform is performed on the remaining samples. Finally, each symbol contained in the resulting block is independently equalized.

There are a number of features that make OFDM flexible, and hence, attractive. First, there are a number of strategies that may be implemented due to the multiplicity of carriers. One strategy would be to tailor our transmitting and reception to accommodate the dead-zones in the channel's frequency response. A more aggressive equalization strategy allocates, from a fixed power budget, power to each of the carriers so as to realize an equalization of the SNR across all carriers. We might wish to assign specific carriers to specific users thereby implementing multiple access. A frequency diversity strategy might involve in-

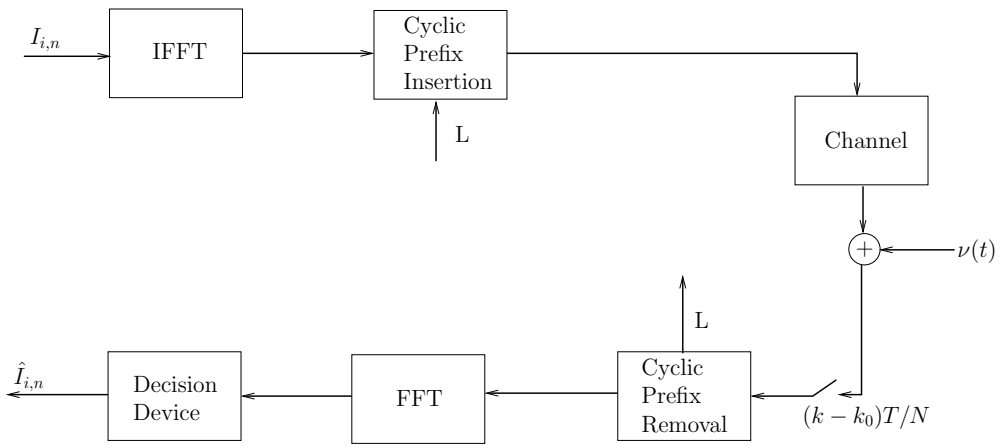


Figure 1.4: The OFDM Transceiver

corporating convolutional coding and an interleaver before the IDFT and after the DFT. The benefit derived here is due to the fact that the interleaver substantially reduces the correlation between adjacent carriers - which improves the performance of decoding convolutional codes. Apart from the multiplicity of carriers, we also note that because each symbol is transmitted over a period of $NT_s$ that if we select $N$ large enough that we will be able to achieve a flat frequency response within each of the separate carriers. This allows us to perform equalization using a single complex multiply. Thus, OFDM affords a great deal of flexibility to meet the particular application at hand.

## 1.5 Thesis Roadmap

In the following chapters we will be considering a number of models for wireless channels. Each model has implications for a particular equalization strategy and sometimes the model may suggest such a strategy. In Chapter 2 we begin our discussion of wireless channel models by introducing a particular application. The application revolves around the notion of the software-defined radio (SDR)

as it might be utilized in an land and airborne wireless communications network. The SDR concept revolves around the idea that by using software-configurable hardware we might achieve radio architectures that span the particular application domain we wish to accommodate. Within this domain we might include every application from stationary flat fading channels to high dynamic time-dispersive channels. In this particular case, our SDR is based on the OFDM modulation/equalization strategy discussed earlier.

Given this particular application as a starting point Chapter 2 considers the most demanding segment of the application domain which we refer to as the Air-to-Ground (AtG) scenario. Within this scenario we begin with a commonly accepted definition for the continuous-time CIR and, under the AtG scenario, show that an appropriate time-variant discrete-time model can be based on a tapped-delay line with each tap's phase changing linearly with time. The tapped-delay line model without the linear phase change is the generally accepted model for time-dispersive channels. However, we see in the case of the AtG scenario that inclusion of linearly changing tap phase allows us to consider ways to mitigate this effect that would otherwise be unavailable to us if we had based our system design on the generally accepted channel model. We also see that this additional fidelity of the model also allows us to improve our performance analysis should we not choose to exploit this additional modelling knowledge.

The purpose of admitting the existence of the AtG scenario is to show that if we consider the possibility of deterministic relationships over and above the essential details (i.e. the generally accepted tapped delay line) within our channel model than we will then have an opportunity to exploit them in our equalization design. This may be a rare event, but it is worth noting before we too quickly adopt a statistical model which would limit our equalization choices.

Having noted the benefits that can be obtained from a detailed accounting of deterministic channel effects, Chapter 3 returns to the more traditional statistical approach of characterizing channel models. In particular we focus on the wideband, or time-dispersive, channel model[3]. In Chapter 3 we begin by reviewing the prior research into wireless channel models with regard to inter-arrival time and channel impulse amplitude distributions. It appears from the literature that there was some attempt at basing these distributional descriptions on a physically-traceable foundation but, inevitably, these were not found to perform as well as performing an empirical fit to data taken from surveys of CIR measurements. In Chapter 3, we revisit the channel impulse amplitude distribution question in an attempt to found a model on a phenomenological basis. We do this by starting with the Suzuki's insightful observation that the combined effects of shadowing and Rayleigh fading result in a mixture distribution named after Suzuki. From this starting point, the thesis makes the assumption that interarrival times have an exponential distribution[4]. Because of this the uniformity of arrival time within a specific interval can be assumed. Then, because of the exponential decay in path loss with respect to delay between transmitter and receiver, we arrive at the assumption that the arriving impulses are uniformly distributed within some loss-range on the dB scale. Having a simple expression for path loss distribution we can then mix this with the so-called "dB-Suzuki" distribution. The dB-Suzuki distribution is simply a transformation of the Suzuki distribution, which is based on an absolute amplitude scale, to a dB scale. Next, we derive a simplified approximation for cases in which the shadowing variance is relatively large. We finally fit some empirical data using this approximated distribution

[3]This is in contrast to a narrowband modelling approach. We can always take the wideband model tap-coefficients and derive the narrowband model but not the other way around.

[4]Prior research suggests a modified Poisson process is a better fit, but the pure Poisson process provides for a mathematically tractable result.

and compare to a lognormal fit which has been suggested by a number of prior researchers and note that our distribution obtains a better fit.

In Chapter 4 we introduce another subject which has not received adequate attention with respect to the CIR. There we address some of the statistics related to the extreme impulse amplitudes contained within the CIR. These types of statistics are known as ordered statistics since they are obtained by sorting the statistics by some measure. In addition to the significance of having an accurate model of the CIR impulse distribution as we saw in Chapter 3, having a model describing what are known as the extreme statistics of the CIR is also of importance since the performance will be dominated by the largest impulses within the CIR. In this chapter we begin by introducing the basics of extreme order statistics. This introduction includes exact results corresponding to particular underlying CIR distributional assumptions as well as asymptotic results which apply to particular distributional classes. Using some of these results we derive the distribution of the sum of the $n$ ordered statistics. In a related derivation we consider the case where the energy not utilized by the equalizer acts as interference to the process and hence obtain the distribution for the signal (which is the sum of the $n$ largest energy impulses) to interference plus noise ratio. Finally, we consider a particular design problem where knowing the distribution of the sum of the largest $n$ would be useful. The particular case we chose was that of a RAKE receiver which performs maximal ratio combining (MRC) on the $n$ largest impulses within the CIR. We first derive the sum-of-extremes for an underlying exponential distribution of channel impulses amplitudes which is commonly done in diversity problems. From this we can determine the probability of non-exceedance (i.e. the probability that the required link margin will not be satisfied). Next, we perform a simulation using a lognormal distribution as the underlying distribution of channel impulse amplitudes and compare the

performance curves to the prior case. Here we note that the more realistic log-normal distribution results in a prediction that the expected performance will be worse (by about two dB for a one percent outage probability) compared with the assumed exponential case.

In Chapter 2 we considered the deterministic effects on an OFDM system. In particular, we were dealing with a scenario which could be rightly considered fast fading due to the presence of the aircraft as one of the communicating platforms. In this chapter we note that there was an optimal number of sub-carriers corresponding to the particular aircraft's dynamic behavior. However, as aircraft dynamics continue to increase we note that there is a point where the overhead of the cyclic prefix begins to dominate and throughput begins to suffer as aircraft dynamics are increased. As a consequence of this, at some point it would be advisable to abandon the OFDM modulation approach and consider a single carrier approach. With this as a motivational background, in Chapter 5 we return to analyzing the single-carrier system approach under the statistical channel model that was developed in Chapter 3. The particular equalization method we consider is the MLSE approach which we introduced above. In this chapter we noted, as we have shown in the table above, that there are particular channel realizations which present some very poor performance for a particular channel length. However, could this kind of performance be expected with any significant degree of frequency so as to eliminate MLSE as a possible equalization method? This is the fundamental question that this chapter addresses. To this end we note that $d^2_{free}$ is a useful proxy for performance of MLSE equalization. We then consider two methods for computing this quantity. The first involves a "brute-force" search of the domain of possible information sequence and error sequence combinations. To exhaustively search this domain space would be

impractical. However, we note that $d^2_{free}$ is often found by search over a small number of errors. Another method for calculating $d^2_{free}$ is given utilizing the weight-enumerating function corresponding to the convolutional code of interest. This is an alternative method, but, we quickly note that is generally only applicable to fairly short constraint length codes. Next, given the statistical channel model developed previously, we then consider the equalization loss as compared to fully utilizing the available channel energy. This equalization loss occurs because of the fact that our performance indicator $d^2_{free}$ is generally less than or equal to the channel energy. So, to assess our expected performance we create the distribution of $d^2_{free}$ and compare it with the distribution of channel energy. We note that there is very little difference which leads to the conclusion that the "worst-case" channels are probably nothing to worry about for most applications. Finally, we consider equalization using MLSE. In particular, because MLSE using the VA is impractical due to the typically long channel lengths, we utilize the T-algorithm to perform our MLSE equalization. Our simulation shows that the T-algorithm performance approaches that of a Gaussian channel having the same energy.

In Chapter 6 we consider two of the most important aspects of a power loss model, those being the average path loss and the shadowing loss. Our goal in this chapter is, as we did in Chapter 3, to place the model on a phenomenological footing rather than simply basing our model on something which seems to fit the empirical data. We first begin by reconsidering the derivation of the average path loss for the classical 2-ray path loss model. This model leads to the notion that average path loss results in $4^{th}$-power loss with distance. We begin this derivation with the same physical model as was used for the 2-ray model. We proceed by assuming that one antenna is near the ground and another is significantly higher altitude (perhaps by several times - a condition consistent with cellular systems).

The typical 2-ray model assumes a small grazing angle of the reflected signal with respect to the direct signal. However if we relax the small grazing angle assumption, we arrive at our final result for the path loss model. The interesting item to note about this model is that it predicts the "knee" which occurs in empirical signal strength surveys over varying distances. In other words, the path loss exponent does not appears to be constant, but it increases at some significant distance.

The shadowing phenomena is usually described in statistical terms as having a normal distribution about the average path loss (expressed in dB). The normal distribution is chosen because the shadowing loss is conceived to be a summation of attenuation factors having the same distribution. By the central limit theorem the conclusion is immediate. For many analyses this description of the shadowing phenomena is adequate. However, there are a number of factors that are still lacking in this description. First, shadowing is a path-dependent phenomena. That is, it is determined by the location of the transmitter-receiver pair. Secondly, shadowing tends to be localized to the specific location of the transmitter and receiver antennae. Intermediate obstructions do not contribute as much to the overall attenuation as the obstructions adjacent to the antennae. We could continue to elaborate on the differences, but, the interaction with the physical environment gives rise to the differences we are enumerating. Consequently, in this section, we propose a new shadowing model which addresses these concerns.

We conclude the thesis in Chapter 7. Included in this chapter is a summary of our new results plus suggestions for further research.

# CHAPTER 2

# Mobile Vehicle Multipath Model

## 2.1 Abstract

This chapter focuses on communications within a high-mobility context with OFDM as the modulation of choice. We first show that the Air-to-Ground (AtG) channel is the most difficult to adapt using standard channel equalization methods. We then derive a new channel model (AtGMM) for the AtG case and use it as the basis for analysis and for simulating the effects within the AtG environment. Next, we derive the optimal channel-estimation-based equalizer for the AtG channel, showing performance equivalent to a comparable time-invariant channel. We then analyze the performance of conventional OFDM-based systems using the AtG channel model and provide guidelines for maximizing the throughput within differing mobility contexts.

## 2.2 Introduction

Orthogonal frequency division multiplexing (OFDM) [WE71] has received considerable attention over the years owing to the relative simplicity of its adaptation to dispersive channels. Indeed, the ability of OFDM to, in effect, "transform" a dispersive wireless channel to a Gaussian one makes it an attractive choice when it is combined with other modulation strategies. Some notable marriages are

multi-carrier code-division-multiple-access [PH97] (MC-CDMA) and multiple input/multiple output OFDM [LWS02] (MIMO-OFDM). In the case of MC-CDMA, OFDM enables one to harness diversity [SK95] in combating frequency-selective fading when symbols are spread across widely separated sub-carriers. MIMO, in its simplest form, requires a flat channel response [Fos98] which can be easily provided by selecting sufficiently narrow OFDM sub-channels.

### 2.2.1 Internet-in-the-Sky

It is to this end that OFDM is being employed in a research project at UCLA. Our vision is to create an "Internet-in-the-sky" to support communication needs in remote areas where wired network access is not available. Fig. 2.1 illustrates the "hierarchical" network envisioned. The hierarchy imposed here is such that nodes with access to greater information bandwidth can serve as gateways for communication to nodes within other clusters that might be accessible only at high cost or not at all. With regard to a wireless "Internet-in-the-sky" concept, this implies that the higher altitude nodes should be the more capable ones. Clearly, nodes with some nominal altitude will have a definite path-loss-rate advantage over those attempting direct ground-to-ground communication. For the radio, a systolic approach is being taken in designing a MIMO-OFDM system. That is, a given radio configuration can be decomposed into primitive transmitter and receiver elements. A basic single-antenna OFDM radio may be composed by pairing an individual transmitter and receiver module, whereas the processing necessary for a N-transmitter/M-receiver MIMO-OFDM system is composed by corresponding numbers of transmitters and receivers. The flexibility afforded by the systolic approach enables a wide variety of radios to be configured that accommodate a broad range of channel environments and bandwidth requirements

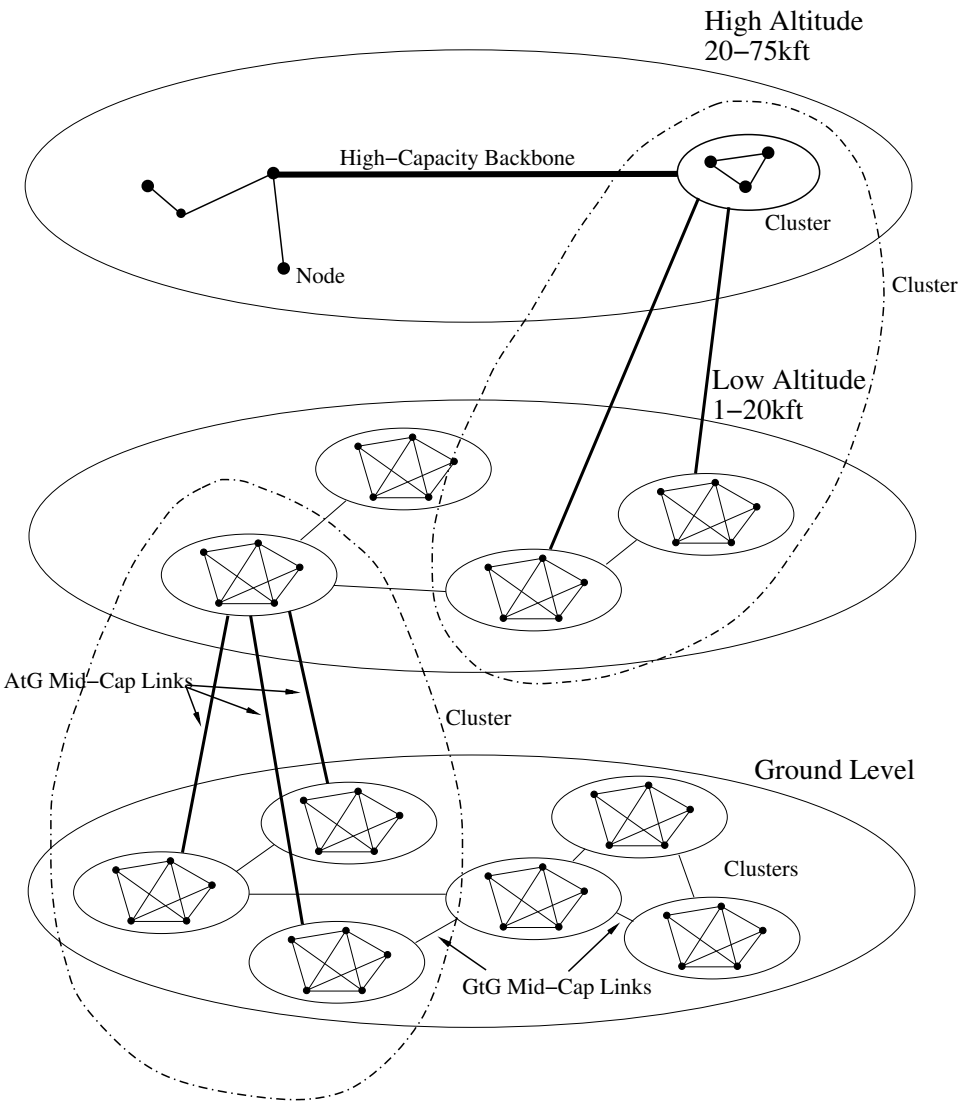


Figure 2.1: Hierarchical Network

while minimizing logistical issues.

Because OFDM is one of the central components of this effort, special emphasis has been focused on understanding the impairments and the corresponding mitigating strategies relevant to OFDM. This of course must be done with regard to the various operational contexts in which these MIMO-OFDM radios will be employed.

After Section 2.2.2 offers a brief review of OFDM, Section 2.2.3 considers research to date on impairments and mitigating strategies for OFDM. Recognizing that the Air-to-Ground (AtG) channel presents both high doppler and time dispersion, in Section 2.3 we derive a new channel model to describe the AtG channel replacing the traditional time-invariant tapped delay line channel model. Using this new dynamical model of the AtG channel, Section 2.4 shows that channel estimation-based equalization in the time-domain provides more responsive tracking of channel dynamics and eliminates inter-carrier interference (ICI). Since the prior equalization is complex compared to conventional OFDM, we consider the performance of conventional OFDM using the AtG channel model derived in Section 2.3 to derive, in Section 2.5, the SINR under this new channel model. We compare the theoretical performance with simulation and also present the simulated performance of the optimal equalization obtained in Section 2.4. Finally, in Section 2.6 we show that the throughput of OFDM (under a constant BER constraint) under dynamic channel conditions is limited by cyclic prefix overhead for low RMS frequency offsets whereas, at high RMS frequency offsets it is limited by the ICI.

### 2.2.2 OFDM Overview

Consider an OFDM system having $N$ subcarriers and a cyclic prefix length of $L$. Each OFDM symbol, $i$, is formed as the inverse discrete Fourier transform (IDFT) of a block of $N$ data symbols $S_i$ concatenated to a block of L samples taken from the tail of the prior IDFT output sequence. The result is passed through a pulse shaping filter, $p_n$, to yield the following transmitted sequence:

$$x_n = \sum_{i=-\infty}^{\infty} s_{i,n-i}\ p_{n-i} \tag{2.1}$$

where $s_i$ is the IDFT of the $i^{th}$ block of data symbols, $S_i$, extended by a cyclic prefix:

$$s_{i,k} = \begin{cases} \sqrt{\frac{1}{N}} \sum_{l=0}^{N-1} S_{i,l} e^{j2\pi lk/N}, & for\ 0 \leq k < N+L \\ 0, & otherwise \end{cases}$$

When the sequence $x_n$ is passed through a linear time-invariant (LTI) channel $h_n$ of length $g$, such as is depicted in Fig. 2.2, inter-symbol interference (ISI) will occur between adjacent OFDM symbols. Here it is assumed that $g < L$ by design. The received signal is:

$$y_n = \sum_{j=-\infty}^{n} x_j h_{n-j} + \nu_n$$

where $\nu_n$ is assumed to be white Gaussian noise (WGN) ($\nu_n$ will be used loosely in the following to represent noise). If we assume perfect timing synchronism, then at the receiver a set of N+L signal samples is taken corresponding to the $i^{th}$ OFDM symbol. By discarding the first $L$ samples the cyclic prefix is removed. Using array notation, we can describe this remaining block of $N$ samples as:

$$Y_i = C_n H C_p W^H S_i + \nu_i \tag{2.2}$$

where $W$ is the $N$-by-$N$ DFT matrix, $C_p$ is the $N+L$-by-$N$ cyclic prefix matrix, $C_n$ is the $N$-by-$N+L$ cyclic removal matrix, and $H$ is the $N+L$-by-$N+L$ Toeplitz

channel matrix (Toeplitz for time-invariant channels). The resulting block, $Y_i$, is processed by performing the DFT:

$$R_i = WC_nHC_pW^HS_i + \nu_i = WCW^HS_i + \nu_i \tag{2.3}$$

where the $N$-by-$N$ matrix, $C = C_nHC_p$, has the circulant property which implies that $WCW^H$ is diagonal.

Since $g < L$, the ISI from the $i - 1^{th}$ symbol does not extend further than the length of the (discarded) L-sample guard interval of the $i^{th}$ symbol. This leads to OFDM's desirable single-tap equalization characteristic. And further, the circulant property of $C$ effectively leads to a decoupling of the equations in (2.3) so that the equalization coefficients may be computed with complexity $O(N)$.

### 2.2.3 OFDM Impairments and Mitigating Strategies

In the performance analysis of communications systems there are a number of impairments to consider. For each impairment, performance analysis has been undertaken to determine the significance of each and various proposals for mitigating them have been reported. In this section we briefly discuss each impairment and refer to the relevant research and, similarly, for each possible mitigating strategy. We do this all in the context of OFDM.

A primary issue with most systems is channel time dispersion which results in ISI. The effects of unmitigated ISI are well known and, in practice, some form of equalization is necessary to accurately decode the transmitted data [Pro95b]. OFDM was developed primarily as a way to simplify the equalization design resulting in single-tap equalization [WE71]. To accomplish this, OFDM generally requires incorporation of a cyclic prefix so that the output of the channel may be

viewed as a series of sequences obtained by cyclic convolution of input blocks with the channel. Cyclic de-convolution may be efficiently implemented using an FFT. It is interesting to note, however, that at least one example of a cyclic-prefix*less* version of OFDM also exists based on a single-feedback-tap DFE for combatting ISI [ST99].

Although OFDM alone helps to address the ISI issue, further benefits may be derived by harnessing the diversity resulting from frequency-selectivity. Since forward error correction is generally provided utilizing low-rate codes, we can allocate the symbols across the sub-channels according to an appropriate interleaving pattern. This will effectively spread each information bit across multiple independently fading sub-channels [WC96].

Although the equalization of OFDM systems is straightforward, this benefit comes at a cost. The trade-off here is that because of the symbol length of an OFDM symbol compared to a single carrier modulation at the same sample rate, OFDM will have greater sensitivity to the rate of channel change. There is, as we see later, essentially a linear trade-off in OFDM symbol length versus the fading rate. To address this problem, our principal tool is to choose an appropriate symbol length that will allow us to track the equalizer taps with sufficient accuracy. For the AtG channel class we will later show that, in addition to time dispersion, we also have a dispersion of frequency offsets among each of the various channel tap delays. In this special case, it is possible to track the channel and perform an equalization that eliminates ICI.

In addition to the environmental impairments mentioned previously, we also have to contend with physical effects within the transceiver. A significant impairment is the non-linearity of the transmitter's power amplifier. That is, we need to consider the dynamic range of the signal we are amplifying because the amplifica-

tion may not be constant over a very wide dynamic range. This is known as the peak to average power (PAR) problem. This problem occurs in OFDM because symbols composed of $N$ information bits require a dynamic range of $20log(N)$ to represent the entire OFDM symbol alphabet. To address this, we can code the output symbols (add redundancy) using a PAR reducing code. This will have the effect of reducing our information transmission rate but, surprisingly, is not as severe as might be presupposed [CP02]. This observation is consistent with information theory which, in this case, would indicate that the vast majority of the input words are *close* to the RMS power [CT91]. Consequently, there are *few* extreme input words. This supports the previous observation that a modest amount of redundancy can be effectively utilized in PAR reduction.

Another transceiver artifact concerns the degree of carrier and symbol timing synchronization. The sensitivity of OFDM to these impairments has been thoroughly covered in [SM00]. In practice the sampling frequency and carrier frequency are coherently derived from the same local oscillator. Because the carrier frequency is much higher than the sampling frequency, we expect carrier phase and frequency stability to dominate transceiver performance. For example, we know that an uncompensated timing error produces a linearly increasing phase error across the subchannels and an uncompensated carrier phase error produces the same phase error across all the subchannels [SM00]. Deriving the sampling and carrier frequency from a common local oscillator we have:

$$\begin{aligned} f_c &= X f_{LO} \\ f_s &= Y f_{LO} \end{aligned} \tag{2.4}$$

If we perturb the local oscillator for one sampling interval, we will induce the following sample timing error:

$$T_e = \frac{1}{Y f_{LO}} - \frac{1}{Y(f_{LO} + \delta)}$$

Similarly, for the same perturbation, the carrier phase error at the end of the sampling interval will be:

$$\phi_e = \frac{X(f_{LO} + \delta)}{Y f_{LO}} - \frac{X f_{LO}}{Y f_{LO}} = \frac{X\delta}{Y f_{LO}}$$

which we pointed out will be the phase error across all the subchannels. The maximum phase error that can be expected due to the timing error $T_e$ is:

$$\epsilon_e = \frac{T_e}{T_s} = \frac{\delta}{f_{LO} + \delta} \approx \frac{\delta}{f_{LO}}$$

Since $X>>Y$ it is clear that perturbations to the local oscillator impact performance through the carrier to a much larger degree than through sample timing. Mitigating these synchronization effects has been approached by many avenues [Moo94, SC97, BSB97] and is the subject of Section 2.4.

### 2.2.4 OFDM and Fast Fading

In the case of mobile systems, the issue of primary concern is fading-rate. There are a number of trends that have forced communications designers to accommodate ever-higher fading rates. First, the scarcity of radio spectrum at the low end is forcing consideration of higher frequency bands. In turn fading rates are higher - proportional to the increased carrier frequency. Second, since the present research seeks a solution that is applicable across a wide range of vehicle mobilities (from stationary to high dynamic aircraft), provision must be made for the most extreme fading case. Third, for block oriented modulations such as OFDM, the fading rate is proportional to the block length.

In fast fading environments, the least-mean-squares (LMS) algorithm may not be able to adapt to the rapid channel variations. Recursive least-squares (RLS) adaptation may be required to remedy this at the expense of an order of magnitude complexity increase. Interpolation of channel impulse response (CIR)

or equalization coefficients is another approach that helps in coping with fast fading [Lee99]. This is useful in cases where the data stream is interspersed with training at the expense of decoding delay. Additionally, the choice of adaptation domain may have an effect on the tracking speed of a particular adaptation algorithm. This is where channel estimation based adaptation may help since this domain is often described by fewer parameters than in the equalizer-tap domain.

## 2.3 The Air-to-Ground Multipath Model (AtGMM)

The one factor that virtually all of the adaptation methods up to the present time have in common is that they treat the channel or equalization coefficients as either random or unknown constants. This situation derives from using a channel model such as is depicted in Fig. 2.2. More specifically, it is assumed that the time evolution of the process cannot be described by some time-propagation model and therefore is treated as random. For many environments, the assumption of an unpredictable evolution of parameters is reasonable. Such fading environments are characterized by their Doppler power spectrum. But, what if the parameter evolution could be accurately described using some dynamical model? In principle, tracking such a parameter set should be less demanding than the traditional non-dynamical set (in the presence of dynamics). This principle is well established in control theory where higher-order tracking algorithms exhibit less tracking lag if the underlying process is of a compatible order. In this section we take a detailed look at the air-to-ground (AtG) channel and propose a new channel model to describe it.

We begin by first reproducing a continuous-time model of the multipath en-

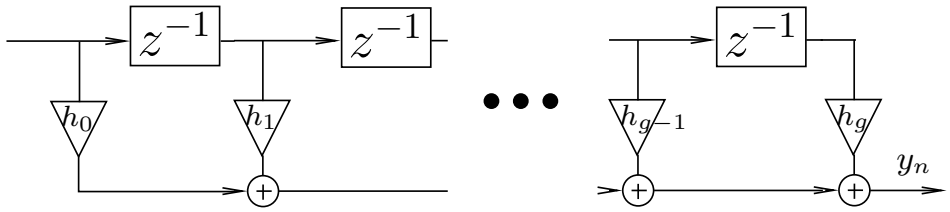


Figure 2.2: Conventional Time-Invariant Discrete-Time Channel Model

vironment [Pro95c].

$$c(\tau;t) = \sum_m \alpha_m(t) e^{j2\pi f_c \tau_m(t)} \delta(\tau - \tau_m(t))$$

This relation expresses the time-variant impulse response of a continuous-time channel as it evolves in time $t$ with a number of arrivals at delays $\tau_m(t)$. We note that the model is expressed in terms of a superposition of discrete arrivals with each arrival $m$ having a particular amplitude $\alpha_m(t)$ and phase $e^{j2\pi f_c \tau_m(t)}$. Since the delay $\tau_m$ is the ratio of range $R_m$ to the speed of light $c$, we have the following alternate expression:

$$c(\tau;t) = \sum_{m \in M(t)} \alpha_m(t) e^{j2\pi R_m(t)/\lambda_c} \delta(\tau - R_m(t)/c) \tag{2.5}$$

where $\lambda_c$ is the carrier wavelength and the set of arrivals at time $t$ and any delay $\tau$ we denote as $M(t)$. Now that we have emphasized in (2.5) the fact that multipath is range-dependent, we can proceed to examine the effect of mobility within various environments. The environments we have identified for this research are the following: 1) Air-to-Air (AtA), 2) Ground-to-Ground (GtG), and 3) Air-to-Ground (AtG).

The GtG environment is characterized by Doppler consistent with ground vehicle speeds and significant time-dispersion caused by nearby scatterers. The AtA environment (i.e. antennae not near the ground) is characterized by high Doppler and a singular line-of-sight (LOS) ray with negligible received ground-reflected rays. The AtG case is characterized by high Doppler and substantial

dispersion caused by scatterers nearby the ground antenna. We also note that there may be several of these dispersion "clusters" of received energy due to the presence of large reflectors that are distant with respect to the receiver and transmitter. The three scenarios are depicted in Fig. 2.3.

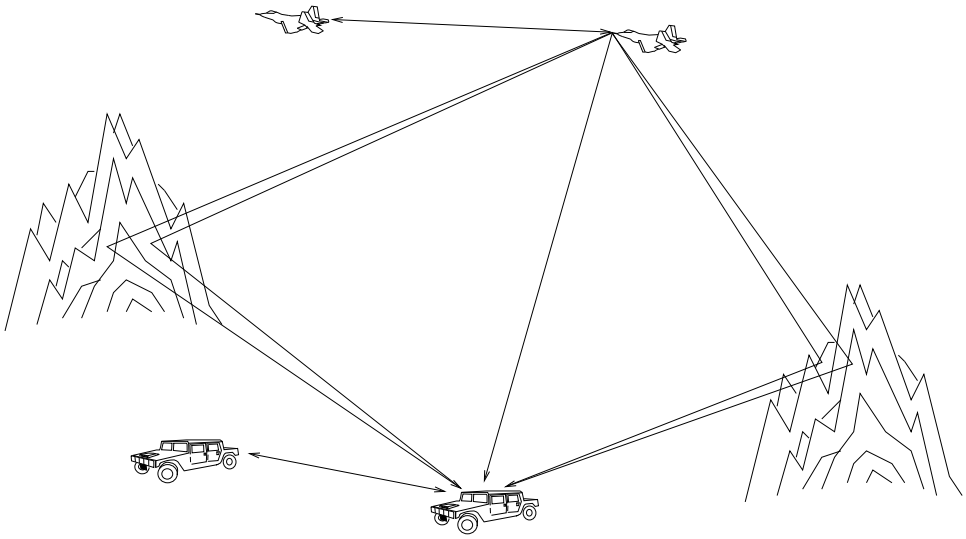

Figure 2.3: AtA, GtG, and AtG Multipath Environments

### 2.3.1 Air-to-Air (AtA)

The AtA case is clearly the simplest of the three and can be considered a non-fading flat channel. For this to be reasonable the ground reflection must be insignificant and the transceiver implementation must employ carrier synchronization. In this case, (2.5) collapses to the following:

$$c(\tau;t) = \alpha(t)e^{j2\pi R(t)/\lambda_c}\delta(\tau - R(t)/c)$$

Focusing on the only impulse arrival at delay $\tau = R(t)/c$ and expressing the range to the first order as $R(t) = R_0 + \dot{R}t$, we have:

$$c(t) = \acute{\alpha}(t)e^{j2\pi\dot{R}t/\lambda_c}$$

where we have absorbed the phase constant $e^{-j2\pi R_0/\lambda_c}$ into $\acute{\alpha}(t)$. Finally, to further simplify the AtA model, we can treat the complex gain $\acute{\alpha}(t)$ as constant as compared to the time-variant phase rotation $e^{j2\pi\dot{R}(t)/\lambda_c}$ to yield:

$$c(t) = \acute{\alpha} e^{-j2\pi\dot{R}t/\lambda_c} \tag{2.6}$$

### 2.3.2 Ground-to-Ground (GtG)

To proceed for the GtG case, we return to (2.5) and focus on the $m^{th}$ multipath ray. Next make the assumption that all signal reflectors are physically stationary with respect to the antennas. We can then conclude that the range rate of a given multipath ray is the following linear combination of the velocities of the transmitter and receiver antennas:

$$\dot{R}_m = \dot{R}_{m,r} + \dot{R}_{m,t} = V_r \cdot L_{m,r} + V_t \cdot L_{m,t} \tag{2.7}$$

which says that the total range rate is the sum of the receiver velocity projected onto the LOS of the multipath ray arriving at the receiver plus the same corresponding to the ray departing the transmitter. Since we are focusing on the $m^{th}$ multipath ray, our GtG model, adapted from (2.6), is now:

$$c(\tau_m, t) = \acute{\alpha_m} e^{j2\pi(V_r \cdot L_{r,m} + V_t \cdot L_{t,m})t/\lambda_c} \tag{2.8}$$

From (2.8) we can arrive at the discrete-time CIR:

$$h_{k,n} = \sum_{m \in \acute{M}(k,n)} c(\tau_m, nT_s) \tag{2.9}$$

where we have "clustered" the arrivals corresponding to the $k^{th}$ delay accordingly:

$$\acute{M}(k,n) \equiv \{m : kT_s \leq \tau_m(nT_s) < (k+1)T_s\}$$

If there are a large number of scatterers nearby either antenna, then it is clear that the distribution of $|h_{k,n}|$ will be Rayleigh [Yac93].

### 2.3.3 Air-to-Ground (AtG)

The relation expressed in (2.9) can now be used to aid our understanding of the AtG case. To continue, we require some assumptions. First, in the AtG case, we can safely assume that the signal emanating from the airborne vehicle does not encounter any local scattering as in the case of the ground vehicle. Second, there may be one or more large scatterers, such as mountains, that are assumed distant with respect to the airborne vehicle. Finally, we shall assume that the signals reflected from our large scatterers are clustered together in delay and that these clusters are not overlapping in time at the receiver. In other words, the range of delays due to all multipaths received from one "mountain" will not overlap the group received from a second "mountain." Of course, it is possible that these groups of multipath arrivals may overlap in delay, but usually this will not be the case. On account of these assumptions we can further specialize our channel model.

In order to visualize this situation refer to Fig. 2.3. The assumptions previously mentioned provide the following. The first two assumptions taken together provide that the departing multipath rays from the airborne antenna which are reflected by one of the distant scatterers will be nearly parallel. So we may assume that the angles between these rays and the aircraft's velocity vector are nearly equal. The last assumption provides that for a given delay index $k$, all of the arriving rays will have nearly the same LOS departing the aircraft. On this account we may write:

$$h_{k,n} \approx e^{j2\pi n T_s V_t \cdot L_{t,k}/\lambda_c} \sum_{m \in \acute{M}(k,n)} \alpha_m^{'} e^{j2\pi n T_s V_r \cdot L_{r,m}/\lambda_c} \tag{2.10}$$

since

$$L_{t,k} \approx L_{t,m} \quad \forall\ m \in \acute{M}(k,n)$$

At this time some observations are in order. Since the channel response described in (2.9) is generally applicable, if we apply it in the case of the AtG channel we will observe that the Doppler bandwidth of this channel is quite extreme in comparison to typical GtG scenarios. Indeed, for realistic vehicle mobility assumptions, the fading rate is dominated by the Doppler induced by the high aircraft velocity. Consequently, an adaptation to such channel behavior would be quite demanding.

However, in (2.10) we note that the fading rate of the summation is comparable with typical GtG scenarios since it is based purely on ground vehicle mobility. This is modified by a delay-dependent phase rotation entirely due to aircraft mobility. This observation leads to the following time-variant channel model which we call the AtG multipath model (AtGMM):

$$h_{k,n} \approx h_k e^{j\omega_k n T_s} \tag{2.11}$$

where:

$$h_k \equiv \sum_{m \in \acute{M}(k,n)} \acute{\alpha_m} e^{j2\pi n T_s V_r \cdot L_{r,m}/\lambda_c}$$

and

$$\omega_k \equiv 2\pi V_t \cdot L_{t,k}/\lambda_c$$

This channel model is depicted in Fig. 2.4. For our AtG model we see that the fading rate is similar to that of the GtG model when the deterministic phase rate is known.

## 2.4 Optimal Equalization under high mobility

Given this new model for the AtG case the next question we must consider is how to best exploit it. This model holds that the Doppler of all rays are not the same.

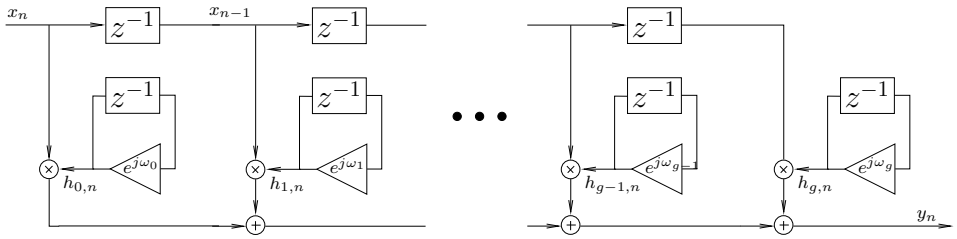


Figure 2.4: AtG (Time-Variant) Discrete-Time Channel Model

If the Doppler "dispersion" (the Doppler spread) of the different multipaths is large enough then, from previous research [SM00], we know that significant ICI will result. In Section 2.5 we seek to quantify this effect, but for the present we will consider an approach to exploiting the AtGMM to mitigate the effect.

### 2.4.1 Time vs. Frequency Domain OFDM Equalization

In the conventional OFDM system, equalization coefficients are determined in the frequency domain. Another way of looking at this is to say that the equalization coefficients are determined in the data domain, or the decision domain we may also say. This domain is generally the immediate choice. However, this may not be the best choice. Alternatively, we may perform equalization in the time domain. The time domain may hold an advantage since the number of coefficients at any time can be no more than $L$ whereas for the frequency domain it is $N$. Since the same measurement stream is used to produce estimates in either domain, the error variance of time domain estimates will be a fraction of the frequency domain estimates.

Since we are interested in the performance in fading environments, we can quantify this advantage by considering the tracking performance of an adaptive filter. As an example, the minimal excess mean-square error (MSE) for the LMS

algorithm is [Say00a]:

$$\zeta_{min}^{LMS} = \sqrt{\sigma_v^2 Tr(R_u) Tr(Q)} \tag{2.12}$$

where $R_u$ is the covariance of the regressor vector $u$, $Q$ is the covariance of the step-wise process noise to be tracked, and $\sigma_v^2$ is the measurement noise. Comparing the two domains, the only variable with respect to (2.12) is $R_u$. If we assume a zero-mean i.i.d. training sequence, then $R_u = \sigma_u^2 I$ in both domains leading to an $\sqrt{L/N}$ improvement in $\zeta_{min}^{LMS}$ for the time domain approach. So, the advantage of working in the time domain is the fact that we can track channel changes with greater responsiveness.

Since time domain channel tracking is preferred for OFDM, we proceed to examine how this may be done for our time variant channel. The received block in (2.2) is dependent on the channel matrix $H$ which, for a static channel, is Toeplitz. The same block is dependent on the circulant matrix $C$. For our time-variant AtGMM, the matrix $C_i$ (the subscript denoting the $C$ corresponding to the $i^{th}$ OFDM symbol) has the structure:

$$C_i = h_0 D_{0,i} + h_1 D_{1,i} R + h_2 D_{2,i} R^2 + \cdots + h_g D_{g,i} R^g \tag{2.13}$$

where post-multiplication by R performs the cyclic left-shift of a row vector and

$$D_{k,i} = diag([\, e^{j\omega_k KiT_s} \;\; e^{j\omega_k [Ki+1]T_s} \cdots e^{j\omega_k [Ki+N-1]T_s}]) R^k$$

where $K \equiv (N+L)$. Since the channel is now sample-variant, $C_i$, in (2.13), is no longer circulant resulting in ICI for AtG applications using conventional OFDM equalization.

If channel estimation-based equalization within the time domain is employed, ICI can be eliminated. This requires a matrix inverse of $C_i$ which, starting from (2.2), yields the following minimum MSE (MMSE) estimate for the trans-

mitted symbols:

$$\hat{S}_i = W C_i^{-1} Y_i \tag{2.14}$$

### 2.4.2 Inversion of $C_i$ for 2-ray cases

In Section 2.4.1 we noted that time-domain equalization requires that $C_i$ be inverted. In general, this is computationally intensive as a matrix inversion is $O(N^3)$ operations. However, in the particular case where there are two multipath rays, we have an inversion method that involves only $O(N^2)$ operations. Consider the following 8-by-8 2-ray "Doppler circulant" matrix:

$$C_i = \begin{bmatrix} h_0 & 0 & 0 & 0 & 0 & h_5 & 0 & 0 \\ 0 & h_0 e^{j\phi_0} & 0 & 0 & 0 & 0 & h_5 e^{j\phi_5} & 0 \\ 0 & 0 & h_0 e^{2j\phi_0} & 0 & 0 & 0 & 0 & h_5 e^{2j\phi_5} \\ h_5 e^{3j\phi_5} & 0 & 0 & h_0 e^{3j\phi_0} & 0 & 0 & 0 & 0 \\ 0 & h_5 e^{4j\phi_5} & 0 & 0 & h_0 e^{4j\phi_0} & 0 & 0 & 0 \\ 0 & 0 & h_5 e^{5j\phi_5} & 0 & 0 & h_0 e^{5j\phi_0} & 0 & 0 \\ 0 & 0 & 0 & h_5 e^{6j\phi_5} & 0 & 0 & h_0 e^{6j\phi_0} & 0 \\ 0 & 0 & 0 & 0 & h_5 e^{7j\phi_5} & 0 & 0 & h_0 e^{7j\phi_0} \end{bmatrix} \tag{2.15}$$

This matrix expresses the Doppler circulant matrix for the case where we have achieved timing synchronization - which explains why we have the $h_0$ elements along the diagonal. Otherwise, the single post-cursor impulse occurs sometime later in the impulse response. The inverse of this matrix is:

$$C_i^{-1} = \begin{bmatrix} A_1 & A_2 \end{bmatrix} \tag{2.16}$$

where

$$A_1 = \begin{bmatrix} h_0^7 e^{28j\phi_0} & -h_0^2 h_5^5 e^{9j\phi_0} e^{18j\phi_5} & h_0^5 h_5^2 e^{21j\phi_0} e^{5j\phi_5} & -h_5^7 e^{25j\phi_5} \\ -h_0^4 h_5^3 e^{18j\phi_0} e^{10j\phi_5} & h_0^7 e^{27j\phi_0} & -h_0^2 h_5^5 e^{11j\phi_0} e^{15j\phi_5} & h_0^5 h_5^2 e^{18j\phi_0} e^{7j\phi_5} \\ h_0 h_5^6 e^{5j\phi_0} e^{23j\phi_5} & -h_0^4 h_5^3 e^{14j\phi_0} e^{13j\phi_5} & h_0^7 e^{26j\phi_0} & -h_0^2 h_5^5 e^{5j\phi_0} e^{20j\phi_5} \\ -h_0^6 h_5 e^{25j\phi_0} e^{3j\phi_5} & h_0 h_5^6 e^{6j\phi_0} e^{21j\phi_5} & -h_0^4 h_5^3 e^{18j\phi_0} e^{8j\phi_5} & h_0^7 e^{25j\phi_0} \\ h_0^3 h_5^4 e^{14j\phi_0} e^{14j\phi_5} & -h_0^6 h_5 e^{23j\phi_0} e^{4j\phi_5} & h_0 h_5^6 e^{7j\phi_0} e^{19j\phi_5} & -h_0^4 h_5^3 e^{14j\phi_0} e^{11j\phi_5} \\ -h_5^7 e^{28j\phi_5} & h_0^4 h_5^3 e^{9j\phi_0} e^{18j\phi_5} & -h_0^6 h_5 e^{21j\phi_0} e^{5j\phi_5} & h_0 h_5^6 e^{25j\phi_5} \\ h_0^5 h_5^2 e^{19j\phi_0} e^{9j\phi_5} & -h_5^7 e^{27j\phi_5} & h_0^3 h_5^4 e^{12j\phi_0} e^{14j\phi_5} & -h_0^6 h_5 e^{19j\phi_0} e^{6j\phi_5} \\ -h_0^2 h_5^5 e^{7j\phi_0} e^{21j\phi_5} & h_0^5 h_5^2 e^{16j\phi_0} e^{11j\phi_5} & -h_5^7 e^{26j\phi_5} & h_0^3 h_5^4 e^{7j\phi_0} e^{18j\phi_5} \end{bmatrix} \tag{2.17}$$

and

$$A_2 = \begin{bmatrix} h_0^3 h_5^4 e^{10j\phi_0} e^{14j\phi_5} & -h_0^6 h_5^1 e^{23j\phi_0} & h_0 h_5^6 e^{3j\phi_0} e^{19j\phi_5} & -h_0^4 h_5^3 e^{14j\phi_0} e^{7j\phi_5} \\ -h_5^7 e^{24j\phi_5} & h_0^3 h_5^4 e^{13j\phi_0} e^{10j\phi_5} & -h_0^6 h_5 e^{21j\phi_0} e^{j\phi_5} & h_0 h_5^6 e^{4j\phi_0} e^{17j\phi_5} \\ h_0^5 h_5^2 e^{15j\phi_0} e^{9j\phi_5} & -h_5^7 e^{23j\phi_5} & h_0^3 h_5^4 e^{8j\phi_0} e^{14j\phi_5} & -h_0^6 h_5 e^{19j\phi_0} e^{2j\phi_5} \\ -h_0^2 h_5^5 e^{7j\phi_0} e^{17j\phi_5} & h_0^5 2 h_5^2 e^{20j\phi_0} e^{3j\phi_5} & -h_5^7 e^{22j\phi_5} & h_0^3 h_5^4 e^{11j\phi_0} e^{10j\phi_5} \\ h_0^7 e^{24j\phi_0} & -h_0^2 h_5^5 e^{9j\phi_0} e^{14j\phi_5} & h_0^5 h_5^2 e^{17j\phi_0} e^{5j\phi_5} & -h_5^7 e^{21j\phi_5} \\ -h_0^4 h_5^3 e^{10j\phi_0} e^{14j\phi_5} & h_0^7 e^{23j\phi_0} & -h_0^2 h_5^5 e^{3j\phi_0} e^{19j\phi_5} & h_0^5 h_5^2 e^{14j\phi_0} e^{7j\phi_5} \\ h_0 h_5^6 e^{j\phi_0} e^{23j\phi_5} & -h_0^4 h_5^3 e^{14j\phi_0} e^{9j\phi_5} & h_0^7 e^{22j\phi_0} & -h_0^2 h_5^5 e^{5j\phi_0} e^{16j\phi_5} \\ -h_0^6 h_5 e^{17j\phi_0} e^{7j\phi_5} & h_0 h_5^6 e^{2j\phi_0} e^{21j\phi_5} & -h_0^4 h_5^3 e^{10j\phi_0} e^{12j\phi_5} & h_0^7 e^{21j\phi_0} \end{bmatrix} \tag{2.18}$$

The inverse of the matrix $C_i$ may be found (within a constant factor) by forming the transpose of the matrix of cofactors. Because of the particular structure of the 2-ray case, the elements of the cofactor matrix for all $N \times N$ matrices are composed of one term. This can be easily verified using the above matrix as an example case. Because of the involved nature of determining the matrix of cofactors, we were not able to derive the inverse from first principles. Rather, we found the inverse for several cases by varying the matrix dimension and location of the impulse responses (post-cursor location) and then extrapolated our observations into a general algorithm which was tested on a larger set of matrices satisfying the 2-ray constraint with the prompt impulse along the diagonal.

Our observations of this class of inverses are as follows:

• If the rate of phase change for $\phi_0$ and $\phi_g$ is zero, we have the inverse of a purely circulant matrix. We note that a property of circulant matrices is that their inverses are also circulant. We observe this property with respect to the factors $h_0$ and $h_g$.

• The sum of the exponents for the $h_0$ and $h_g$ factors is $N-1$; where $N$ is the dimension of $C_i$.

• The sum of the exponents for the $\phi_0$ and $\phi_g$ factors is $N(N-1)/2-i$, where $i$ is the column number starting with column zero.

• The difference between the $\phi_g$ exponents from one row to another is a constant integer multiple of $\phi_g$ across all columns (modulo $N(N-1)/2$). As a consequence of this property, when the initial phase factors are determined for row 1, the following row's phase factors may be easily determined if the change in phase for each row is known before hand.

Further details of this algorithm are presented in Section 2.8.

### 2.4.3 AtGMM Channel Estimation

From (2.13) the channel parameters we would like to estimate are the complex coefficients $h_{n,k}$, and the associated frequencies $\omega_k$. Since the system is dynamical, conventional adaptive filters are generally not appropriate and we will be forced to consider a Kalman filter. Further, since this system is non-linear, we should consider the "extended" variant of the Kalman filter (EKF). The system we wish to model has the following state propagation and observation equations, respectively:

$$\begin{aligned} x_{n+1} &= f_n(x_n) + g_n(x_n)u_n \\ y_n &= h_n(x_n) + \nu_n \end{aligned} \tag{2.19}$$

In the following, we take the the states to be estimated as random constants and hence we assume $u_n = 0$.

The EKF for estimating $x_n$ is described by the familiar expressions below [Say00b]:

$$\begin{aligned} \hat{x}_{n+1|n} &= f_n(\hat{x}_{n|n}) \\ \hat{x}_{n|n} &= \hat{x}_{n|n-1} + K_{f,n}[y_n - h_n(\hat{x}_{n|n-1})] \\ K_{f,n} &= P_{n|n-1}H_n^*(H_nP_{n|n-1}H_n^* + R_n)^{-1} \\ P_{n|n} &= (I - K_{f,n}H_n)P_{n|n-1} \\ P_{n+1|n} &= F_nP_{n|n}F_n^* + G_nQG_n^* \end{aligned} \tag{2.20}$$

where:

$$\begin{aligned} F_n &= \left.\frac{\partial f_n(x)}{\partial x}\right|_{x=\hat{x}_{n|n}} \\ H_n &= \left.\frac{\partial h_n(x)}{\partial x}\right|_{x=\hat{x}_{n|n}} \end{aligned} \tag{2.21}$$

and $Q = 0$ on account of the previous assumption. For the AtGMM we define the following state vector:

$$x_n \equiv [\, h_{0,n} \;\; e^{j\omega_0 T_s} \;\; h_{1,n} \;\; e^{j\omega_1 T_s} \;\; \cdots \;\; h_{L-1,n} \;\; e^{j\omega_{L-1} T_s} \,]^T$$

where $h_{k,n}$ and $e^{j\omega_k T_s}$ are those in (2.11). Our state propagation function $f_{k,n}(x_n)$ is time-invariant and is uncoupled between different tap delays as follows:

$$x_{n+1,k} \equiv [\, h_{k,n+1} \quad e^{j\omega_k T_s} \,]^T = [\, h_{k,n}e^{j\omega_k T_s} \quad e^{j\omega_k T_s} \,]^T$$

where:

$$x_n \equiv [\, x_{n,0}^T \quad x_{n,1}^T \quad \cdots \quad x_{n,L-1}^T \,]^T$$

The observation equation above is the cyclic convolution of the input vectors $s_i$ and the time-variant channel $h_n$ and is obtained as the individual rows taken from (2.2) (with $C_i$ in place of $C$) so that:

$$y_n = Y_{i,m} = \sum_{k=0}^{L-1} h_{k,n}s_{i,j} + \nu_n \tag{2.22}$$

where $s_{i,k}$ is the $k^{th}$ element of $s_i$, $m = [n \; mod \; (N + L)] - L$, and $j = (N - k + m) \, mod \, N$. The expression for $m$ accounts for the fact that only $N$ of every $N$+$L$ observations are processed in channel estimation.

Again, because the states corresponding to different tap delays are uncoupled, we can express $F_n$ and $H_n$ in terms of a specific delay $k$:

$$\begin{aligned} F_{n,k} &= \begin{bmatrix} e^{j\omega_k T_s} & h_{k,n} \\ 0 & 1 \end{bmatrix} \\ H_{n,k} &= \begin{bmatrix} s_{i,j} & 0 \end{bmatrix} \end{aligned} \tag{2.23}$$

with the complete matrices expressed as:

$$\begin{aligned} F_n &= diag\left(\begin{bmatrix} F_{n,0} & F_{n,1} & \cdots & F_{n,L-1} \end{bmatrix}\right) \\ H_n &= \begin{bmatrix} H_{n,0} & H_{n,1} & \cdots & H_{n,L-1} \end{bmatrix} \end{aligned} \tag{2.24}$$

In Section 2.5.3 we present a comparison of the signal-to-interference-ratio performance using this channel estimation-based method with that of conventional OFDM equalization.

## 2.5 Conventional-OFDM in the High-Mobility Environment

Previously, we have developed a model for the AtG channel environment as well as a means of channel estimation. Because the channel estimation-based optimal equalization method uses the matrix inverse of $C_i$ it is straightforward to see that this method eliminates ICI (at substantial complexity cost). However, when conventional equalization is employed we know that ICI is unavoidable. In this section we consider the performance implications of the AtGMM for conventional equalization.

### 2.5.1 Computing the Average SINR for the AtGMM

Since the frequency offset of each delay within the AtGMM is different, we can employ existing analyses [SM00] of carrier-offset performance as a starting point. In our analysis we consider the average SINR across the entire channel bandwidth since, in the AtGMM, we are dealing with a frequency-selective channel. Furthermore, since we expect to code our information across multiple subchannels, the SINR we are interested in can be expressed as the ratio of the average signal energy to the average noise plus interference energy. Finally we note that perfect channel knowledge is assumed in the following analysis. Clearly, practical systems must employ channel estimation of some sort and, consequently, additional degradation must be expected. The effects of imperfect channel knowledge are covered in [AC98].

We can evaluate the average SINR across the subchannels as the ratio of the average received "useful" energy to the average noise plus self-interference energy:

$$SINR = \frac{\bar{S}}{N_o + \bar{A}} \tag{2.25}$$

where $\bar{S} \equiv \frac{1}{N}\sum S_n$ and $\bar{A} \equiv \frac{1}{N}\sum A_n$.

Starting from [SM00], the interference to the $n^{th}$ subcarrier due to the $i^{th}$ subcarrier and the $k^{th}$ multipath in the AtGMM environment is:

$$\begin{aligned} I_{n,i,k} &= \frac{1}{\sqrt{N}}\sum_{m=0}^{N-1} h_{k,m} e^{-j2\pi(ik+im-nm)/N} \\ &= \frac{1}{\sqrt{N}}\sum_{m=0}^{N-1} h_k e^{j\omega_k(m+M)T_s} e^{-j2\pi(ik+im-nm)/N} \end{aligned} \tag{2.26}$$

where $M$ is an integer multiple of $K$ and the "useful" signal within the $n^{th}$ subcarrier due to the $k^{th}$ multipath is $I_{n,n,k}$. The total signal energy within the $n^{th}$ subcarrier results from the coherent sum due to all contributing multipaths:

$$S_n = \left| \sum_{k=0}^{g-1} I_{n,n,k} \right|^2$$

The total interference energy within the $n^{th}$ subcarrier results from the coherent sum due to all contributing multipaths from all subcarriers $i \neq n$:

$$A_n = \sum_{i \neq n} \left| \sum_{k=0}^{g-1} I_{n,i,k} \right|^2$$

Also, it can be shown that the average interference power per subcarrier may be calculated as:

$$\bar{A} = \|h\|^2 - \bar{S}$$

with

$$\bar{S} = \sum_{k=0}^{g-1} |h_k|^2 \frac{sin^2(\omega_k N/2)}{N^2 sin^2(\omega_k/2)}$$

The previous two expressions provide the necessary information to calculate the desired SINR.

### 2.5.2 Minimizing ICI in the AtGMM

OFDM systems commonly employ carrier synchronization to mitigate the ICI that would otherwise result without it. Ideally, we would like to maximize the average SINR as described. This may be done by, equivalently, minimizing the ICI or maximizing the average signal power. The result is more immediate if we choose the latter. The average signal power with carrier synchronization is given as:

$$\bar{S} = \sum_{k=0}^{g-1} |h_k|^2 \frac{sin^2((\omega_k - \omega)N/2)}{N^2 sin^2((\omega_k - \omega)/2)} \tag{2.27}$$

where $\omega$ is the carrier synchronization frequency. Maximizing (2.27) by finding the $\omega$ that zeros its derivative yields an intractable expression that may only evaluated by numerical methods. Alternatively, we can approximate this if we recognize that the individual terms in (2.27) are all maximized when $\omega = \omega_k$ for their respective $\omega_k$'s. Furthermore, we recognize that the numerators of these

terms are minimized at the same set of points. And, invoking a small-angle approximation, we arrive at the following expression to be minimized:

$$\sum_{k=0}^{g-1} |h_k|^2(\omega_k - \omega)^2$$

which is clearly minimized when:

$$\omega = \frac{\sum_{k=0}^{g-1} \omega_k |h_k|^2}{\|h\|^2} \tag{2.28}$$

That is, we can minimize the ICI by driving the carrier synchronization frequency to be equal to the power-weighted average Doppler; an intuitively satisfying result. Although (2.28) only *approximately* maximizes (2.27), for even a moderately-dispersive set of Doppler components this result is sufficiently accurate to assure a small signal loss when compared to using the optimal carrier frequency.

### 2.5.3 Simulation Results

In Fig. 2.5 we present simulation results which compare the simulated and theoretical SINR for a particular selection of tap coefficients for an input SNR of 30dB. A 64-subcarrier system with a 16 sample cyclic prefix is simulated. The comparisons include the theoretical SINR of Conventional OFDM (Eq. (2.25)), simulated SINR of Conventional OFDM (Sim COFDM), and simulated SINR of Optimal OFDM (Sim OOFDM). For these comparison cases we use the following vector of tap coefficients: $\{0.8 - 0.1j, 0.1 - 0.3j, -0.1 + 0.05j\}$, all other taps are zero. The time/frequency-dispersive case uses the following set of phase rotations to propagate the phase of each tap: $\{e^{j3\omega}, e^{-j2\omega}, e^{j0.5\omega}\}$ where we vary $\omega$ to cover the range of RMS frequency offsets of interest. Because of the frequency-dispersion, we characterize the normalized frequency offset as follows:

$$\epsilon \equiv \frac{N}{2\pi}\, \omega_{RMS}$$

where

$$\omega_{RMS} \equiv \left( \frac{1}{|h|^2} \sum_{k=0}^{g-1} |h_k|^2 \omega_k^2 \right)^{1/2}$$

This represents the weighted RMS frequency offset to subcarrier bandwidth ratio.

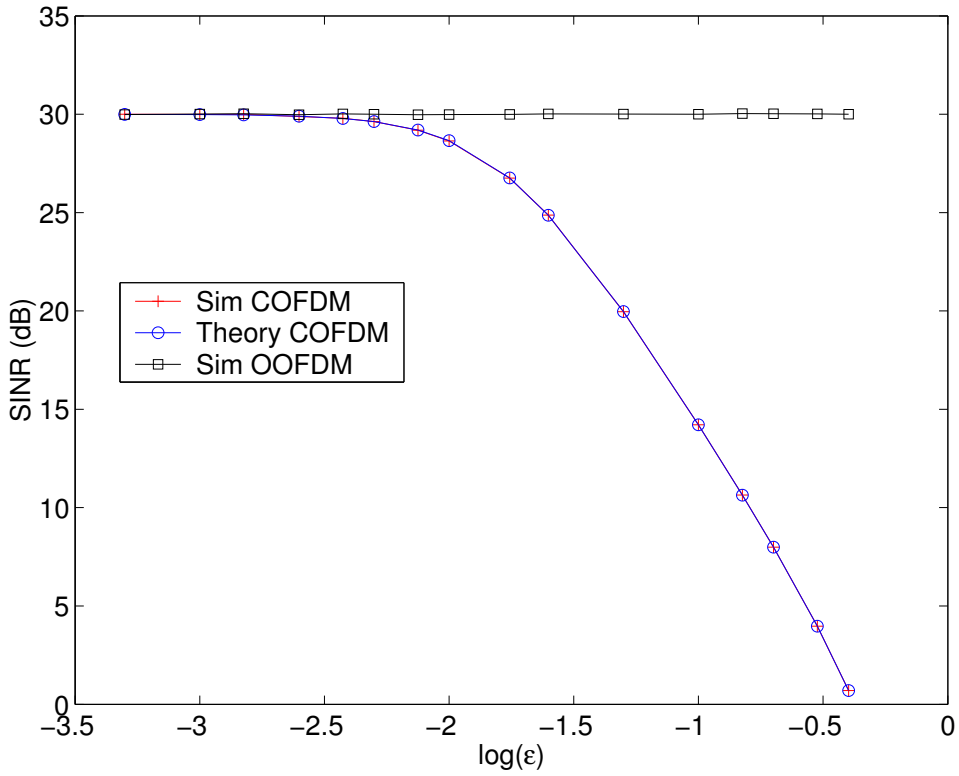


Figure 2.5: Comparison of Conventional VS Optimal OFDM Processing

We note that for a normalized frequency offset exceeding 1%, that significant loss in SINR occurs in conventional systems. However, as we noted in Section 2.4, the optimal OFDM processing is able to eliminate ICI. Consequently, we can maintain the input SNR regardless of the various tap frequency offsets. We also note that these results assume that the frequency offsets for each tap are within 1/2 the subcarrier bandwidth.

## 2.6 Optimization of OFDM in the High-Mobility Environment

In the previous section we derived an expression for the SINR within the AtGMM context when conventional OFDM is used. This allows us to assess the effect on the *effective* SNR, that is the SINR, when confronted with a specific time/frequency dispersive scenario. To assess this effect, we note that it is necessary to consider both the number of subcarriers to be used as well as the specific RMS frequency offset. They must be jointly considered because, as we see in (2.27), $N$ may be traded against the specific set of $\omega_k$'s (in addition to the proper choice for the carrier synchronization frequency $\omega$). This suggests that under certain severe situations we may wish to decrease $N$ to a point where the ICI is not problematic. However, since OFDM is burdened with the overhead of a cyclic prefix, this strategy will reduce the information throughput. To put this more precisely, the information throughput can be expressed:

$$\eta = \frac{N}{N+L} b \tag{2.29}$$

where $b$ is the number of bits per subcarrier and the throughput, $\eta$, is expressed in units of bits/sample.

In order to fairly compare various options, it is necessary to establish a specific (uncoded) BER performance criterion to be applied to all options. Consequently, this BER criterion has been established for all results in this section at $10^{-3}$. Under this requirement, we note that the number of bits per subcarrier $b$ has a nearly linear relationship to SNR per bit (expressed in dB) and $b^2$ also has a linear relationship to SNR. Taking the logarithm of (2.25) we can extract $b$ and use it in (2.29). We will then have an expression we can use to optimize the selection of $N$ to maximize the information throughput.

As an example, we have shown in Fig. 2.6 several throughput curves corresponding to different mobility scenarios. The three scenarios correspond to stationary, low-dynamic, and high-dynamic mobility and use the same time/frequncy dispersive channel tap parameters used earlier and having RMS frequency offsets of $10^{-5}$, $10^{-4}$, and $10^{-3}$ cycles per sample respectively.

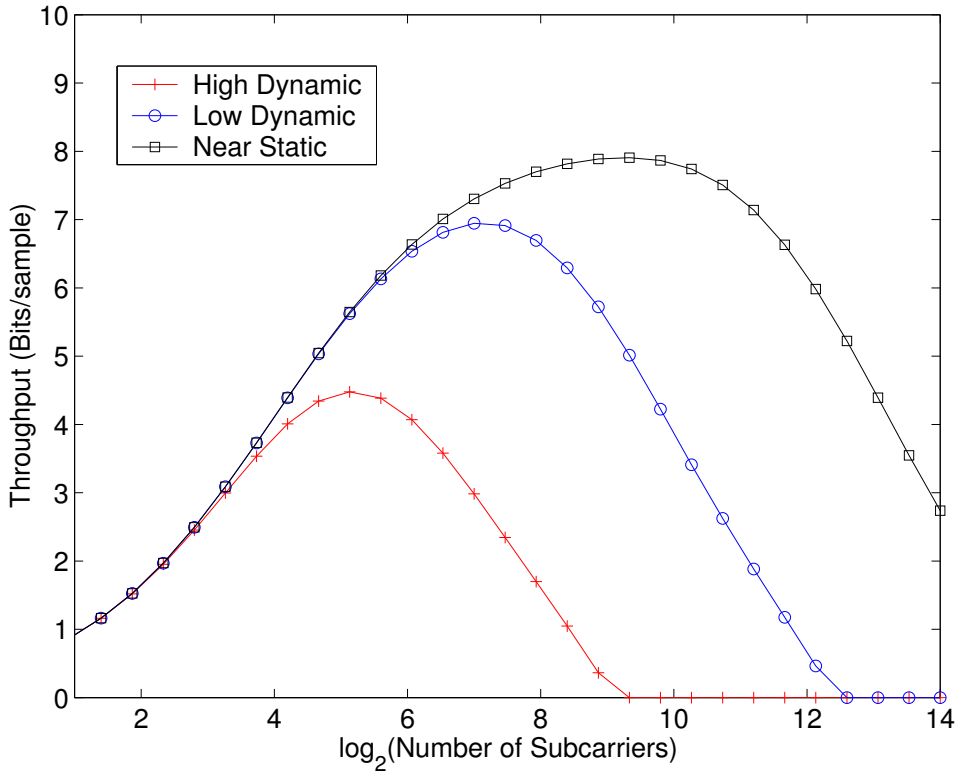


Figure 2.6: Example OFDM Throughput Performance

From Fig. 2.6 we realize that at on the high end, throughput is limited by frequency offset sensitivity. On the low end, throughput is limited by the cyclic prefix overhead (which is taken as $L = 16$ in this section). Consequently, an optimization problem presents itself. We can now determine the optimal number of subcarriers that will maximize throughput given a particular RMS frequency offset subject to our BER constraint. Fig. 2.7 presents the results of

this numerical analysis.

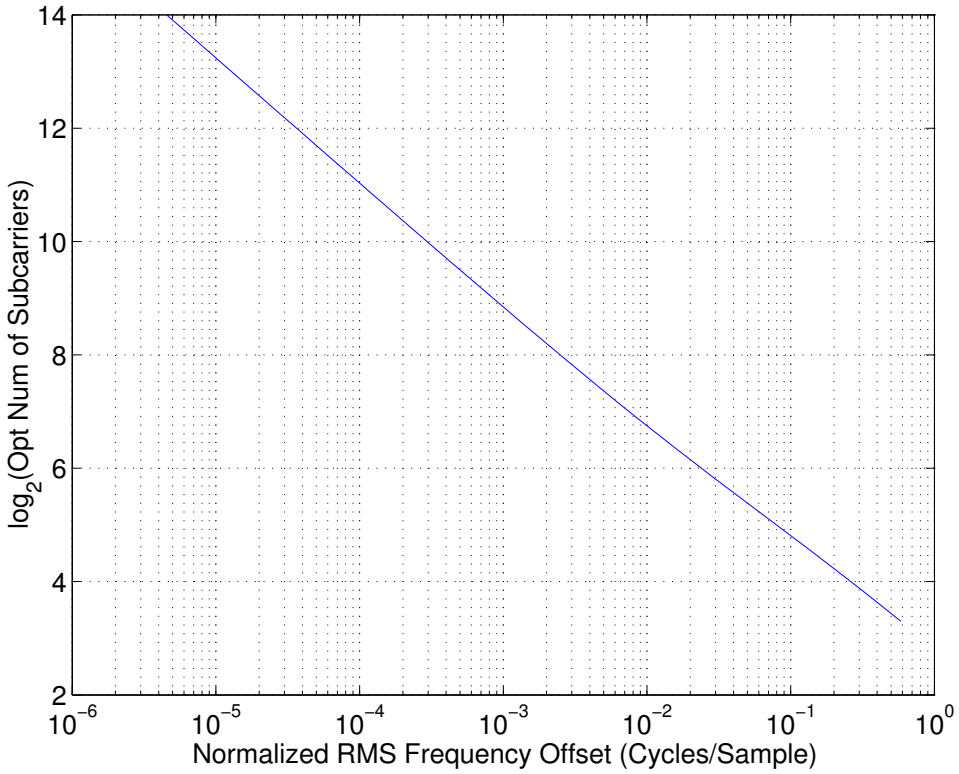


Figure 2.7: Optimal Symbol Size VS RMS Freq Offset

For very small RMS frequency offsets, the optimal symbol size is quite linear with change in RMS frequency offset. Then as we approach higher offsets, resulting in significant ICI, the slope decreases. This is due to the fact that as the cyclic prefix becomes a more significant proportion of the total symbol that throughput then begins to suffer. Consequently, as the frequency offset increases further, corresponding decreases in the throughput-optimal symbol size lessen when compared to those of the small-offset regime. This figure can be used in the design of conventional OFDM systems within fading contexts for selection of the appropriate symbol set size.

Finally, in Fig. 2.8 we present the corresponding throughput that can opti-

mally be achieved for a given RMS frequency offset.

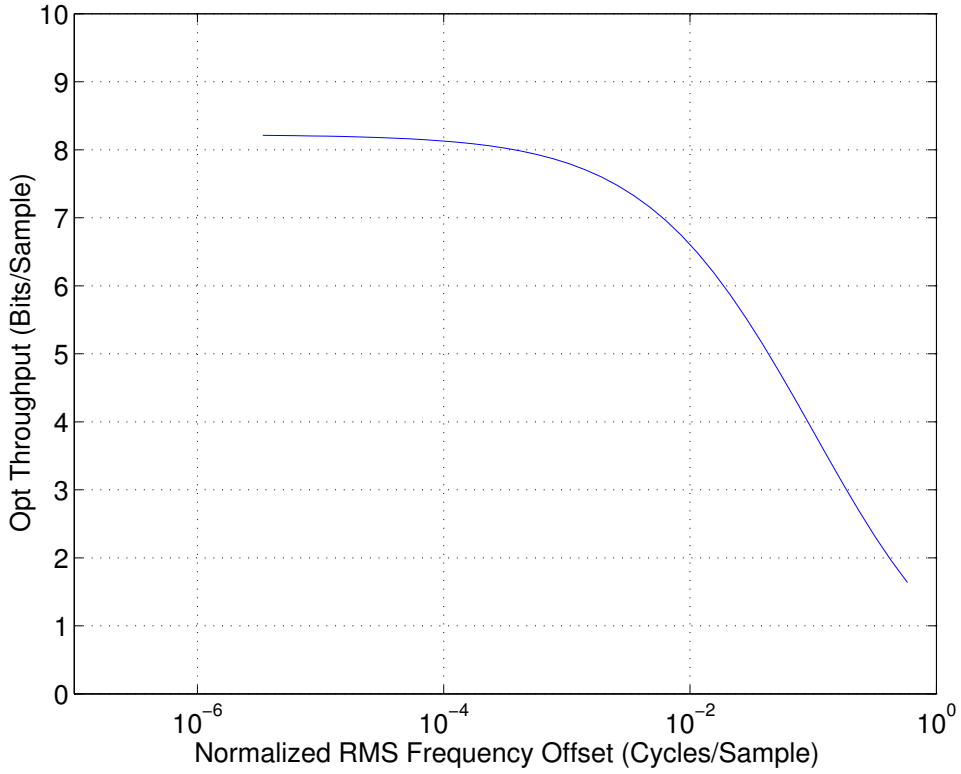


Figure 2.8: Optimal Throughput VS RMS Frequency Offset

## 2.7 Conclusion and Future Directions

In this chapter we have addressed the performance implications of high mobility with regard to OFDM modulation. In order to study this it was useful to derive an AtGMM channel model to replace the conventional time-invariant tapped delay line model. For this new model we obtained a means to estimate the parameters using an EKF. The result of such an estimation could be applied to an estimation-based equalization within the time domain for OFDM. Recognizing that such an equalization approach is prohibitively complex we then considered the effect of the

AtG mobility within the context of conventional OFDM equalization and derived a performance measure in the form of an SINR. This expression can be used to evaluate specific time/frequency dispersive AtGMM channels. Simulations were performed that confirmed correspondence with the derived theory. The simulation also supports the claim that the optimal equalization eliminates ICI. Continuing the theme of using conventional OFDM within high mobility contexts we presented a numerical analysis showing that an optimal symbol size could be selected that would maximize the information-loading within each subcarrier, given a specific received SNR and BER constraint.

Further work could be done with regard to the AtGMM in the context of single-carrier systems in channel estimation to begin with but perhaps also in the equalization area as well. Also, the AtGMM may be a convenient method for generating fading simulations. In general, fading is often modelled as a stochastic process. But, in checking the performance of systems which assume stochastic input, it may be simpler (particularly in hardware-based channel simulators) to generate the AtGMM fading profile as compared to generating a random profile.

## 2.8 Two-Ray Near Circulant Matrix Inverse

In this section we present an algorithm for obtaining the inverse of a near-circulant matrix $C$ derived from a two-ray channel in the AtG environment. This algorithm is based on the assumption that the first impulse within the CIR starts at delay index zero and its complex coefficient is denoted as $h_0$. The second starts at delay index $d$ and its complex coefficient is denoted as $h_d$. Also, $\alpha$ and $\beta$ denote the rate of phase change for taps 0 and $d$ respectively. The matrix size is denoted as $N$. In the result below, matrix indexing begins with zero.

$$C_{i,j}^{-1} = (-1)^{i+j} h_0^{mod(N-1+dj+(N-d)i,N)} h_d^{N-1-mod(N-1+dj+(N-d)i,N)} e^{j\alpha_{i,j}\phi_0} e^{j\beta_{i,j}\phi_d}$$

if $i, j \neq 0$. Otherwise,

$$C_{0,0}^{-1} = h_0^{N-1} e^{jM\phi_0}$$

where:

$$M = \frac{N(N-1)}{2}$$

$$\alpha_{i,j} = X(V_j, X(H_i, 0))$$

$$\beta_{i,j} = M - j - \alpha_{i,j}$$

$$X(V_k, m) = mod(NM + m + V_k, M)$$

$$V_{mod(di,N)} = -i - \frac{D-1}{2}(N-1)$$

$$H_{mod((N-d)i,N)} = -i - \frac{N-D-1}{2}(N-1)$$

# CHAPTER 3

# Statistics of the Channel Impulse Response

## 3.1 Introduction

Multipath is an accepted reality within wireless communication systems. Its effect may be deleterious as in the case of inter-symbol interference or necessary and desirable as in the case of MIMO systems. In any case, it is necessary for systems designers to have some a priori knowledge of the multipath environment that the system is likely to encounter in service.

The multipath channel can be described as a system with the continuous-time impulse response:

$$c(t;\tau) = \sum_{k=1}^{L} \alpha_k(t)\delta(\tau - \tau_k) \tag{3.1}$$

Where $\tau$ represents the delay incurred in transit and $\alpha_k$ is the complex gain associated with the $k^{th}$ impulse. When the symbol period of a communications system is significantly longer duration than the length of the channel impulse response (CIR) the system is said to be narrow-band. In such a case, phase-shifted versions of the received signal corresponding to each of the channel's impulses combine non-coherently. In the discrete domain, the appropriate representation of such a channel would be as a single impulse. Conversely, when the symbol length is significantly shorter than the CIR we are dealing with a wide-band system. In this case, the discrete-domain CIR must be represented by a sequence of complex

gains. The focus of this chapter is on wide-band channel characteristics[1].

There are two gross measures of the channel characteristics that systems designers frequently utilize. One key piece of information is the RMS delay spread which provides a measure of the length of the significant CIR which is required in equalizer design [Yac93].

The other key parameter is the coherence time [Yac93]. The coherence time provides an indication of the time over which two signals are similarly affected by the channel. That is, the channel does not change *significantly* over this period of time. This information is useful in determining the required performance of the equalization adaptation algorithm.

At a more detailed level, the designer may be interested in the inter-arrival times of the impulses along with the associated impulse energies. Finding the distribution for the impulse energies within the CIR is the subject of the present chapter.

The rest of this chapter is organized as follows. Section 3.2 identifies some of the research that has been undertaken in the area of the statistics of the CIR. Section 3.3 proceeds by using the work of Suzuki as a basis and derives a new density for the impulses within the CIR. Section 3.4 compares the new distribution with the lognormal using previously collected empirical data. Finally, we conclude the chapter in Section 3.5.

[1]A nice, unified, treatment of the statistics of narrowband channels can be found in [YSB04].

## 3.2 Previous Research

### 3.2.1 Distribution of Arrival Times

The continuous time impulse response (3.1) has embedded within it the sequence of arrival times represented by the $\tau_k$'s. We can represent these arrival times as:

$$\tau_k = \sum_{m=1}^{m=k} X_m \tag{3.2}$$

where $X_m$ is the inter-arrival time between the $m^{th}$ and $(m+1)^{st}$ impulse. If the inter-arrival times are independently distributed, then the density of $\tau_k$ is:

$$p_{\tau_k}(x) = p_{X_1}(x) \ * \ p_{X_2}(x) * \ \ldots \ * \ p_{X_k}(x) \tag{3.3}$$

where $*$ represents the convolution operator. Only under a fairly restricted set of conditions can this density be evaluated in closed form.

In more practical terms, arrival times describe the time at which an impulse of some *significance* is detected. We emphasize the word *significance* because detection of an arrival depends on how sensitive a detector is used by the designer. Consequently, if our detection system is very sensitive, then we would expect to detect more arrivals within a specified interval of time than if it were less sensitive. By sensitivity, we mean that the detector can discriminate between an actual impulse and the front-end noise of the detection system. If we apply this notion within the context of physical measurement of the CIR, we are faced with the fact that there is some noise floor below which we cannot reliably detect impulses. Consequently, such a system must set a threshold for the detection of impulses. Given this preliminary discussion, we are prepared to consider the subject of arrival times.

To a first approximation, if we assume that the reflectors are uniformly distributed within our environment, it would then be sensible to choose a Poisson

point process to describe the arrival times (if we neglect the impulse threshold). The interval of time between arrivals must have an exponential distribution for the Poisson model to hold. Furthermore, it follows that the time of the $n^{th}$ arrival, $\tau_n$, has an Erlang-$n$ distribution.

Prior experiments have shown that the Poisson assumption holds under cases of relative detector insensitivity, that is, considering only the relatively strong impulses. When the sensitivity is increased, it has been observed that the Poisson model does not provide a good fit. It is thought, with good reason, that the urban and factory/office/wherehouse environments do not adhere to the random distribution of reflectors assumption. In this case Turin [Tur72] proposed the so-called modified Poisson process to describe this case (a.k.a. $\Delta - K$ model).

The traditional Poisson process is described by one parameter - the arrival rate $\lambda$. Under the $\Delta - K$ model, the arrival rate may take on one of two values - either $\lambda$ or $K\lambda$ depending on a state variable. The state variable is initially set to select an arrival rate of $\lambda$. When an arrival occurs, the state variable is set to select the arrival rate of $K\lambda$. If another arrival does not occur within a time interval of $\Delta$ seconds, the state variable reverts back to the initial state and the arrival rate is again set to $\lambda$.

When $K > 1$ the probability that there will be another arrival within $\Delta$ seconds is increased compared to the normal arrival rate. This selection results in a "clustering" of arrivals. When $K < 1$, the likelihood of another arrival within $\Delta$ seconds is decreased compared to the usual arrival rate. This results in a tendency for arrivals to occur with a uniform inter-arrival rate. For $K = 1$ or $\Delta = 0$, the process reverts to the usual Poisson.

Suzuki's work [Suz77] in this area showed that for proper fitting of the $\Delta$ and $K$ parameters, the number of arrivals within various time intervals could

be modelled with good agreement to the experimental data. One reason is that urban environments do tend to cluster their reflectors. Another reason, perhaps more compelling, is that there are three parameters that may be adjusted to fit the data.

Another distribution that has been used to describe the inter-arrival process [YM91] is the Weibull distribution. The density is given below:

$$f_x(x) = \frac{\beta}{\alpha}\left[\frac{x}{\alpha}\right]^{\beta-1} e^{-\left[\frac{x}{\alpha}\right]^{\beta}} \tag{3.4}$$

The Weibull distribution contains three parameters, $\alpha$, $\beta$, and $\nu$. Since inter-arrival times are always positive, we take the location parameter $\nu$ to be zero which converges to the two-parameter version given above. From a phenomenological point of view, the Weibull does not obviously follow from a physical justification the way a pure Poisson does. It is interesting to observe that for $\beta = 1$ the Weibull does converge to the exponential distribution - the basis for the Poisson process. In [YM91] it was noted that appropriate selection of the parameters could be used to achieve a good fit for different sets of empirical data. So, judicious selection of the parameters may be key.

Of the above descriptions of the inter-arrival process it is clear that both are based on the notion that the arrival process is stationary with time. In other words, for the overall time span that the CIR covers, the inter-arrival process is statistically invariant. This is a fundamental assumption that may be open to challenge. In fact, given the idea that only impulses exceeding some threshold are counted, it is reasonable to conjecture that the inter-arrival times increase as we traverse the time span of the CIR. This is because with increasing delay we expect a decay in the mean amplitude of the impulses. In fact, it is clear that the impulses must die-out altogether eventually with the result that we should approach infinite inter-arrival time.

### 3.2.2 Distribution of Impulse Amplitudes

The knowledge of the arrival-time process provides an important part of the description for the CIR. From it we can ascertain the length of the channel we will likely encounter in practice and perhaps be able to optimize the equalizer design accordingly. But this is only part of the information required. Additionally, we require statistical knowledge of the impulse amplitudes. In this area it has been customary for most researchers to perform parameter selection of some popular distributions in order to fit the empirical data.

The impulse response can be characterized as a sequence of complex gains resulting from the diffraction, scattering, and reflection of radio waves within the environment. A particular coefficient within this sequence may be considered as the non-coherent sum of a multiplicity of multipath arrivals occurring within the sample delay. It can be shown that for a particular impulse containing a LOS component the distribution is Rician as given below:

$$f_x(x) = \frac{x}{\sigma^2} \exp\left(-\frac{x^2 + a^2}{2\sigma^2}\right) I_0\left(\frac{ax}{\sigma^2}\right) \tag{3.5}$$

where $I_0$ is the zero$^{th}$-order modified Bessel function:

$$I_0\left(\frac{ax}{\sigma^2}\right) = \frac{1}{2\pi} \int_0^{2\pi} \exp\left(\frac{ax\cos\theta}{\sigma^2}\right) d\theta \tag{3.6}$$

and $a$ is the amplitude of the LOS component.

When the LOS component is not present, the distribution converges to the Rayleigh. Derivations for these distributions and justification, from a phenomenological basis, may be found in [Yac93].

$$f_x(x) = \frac{x}{\sigma^2} \exp\left(-\frac{x^2}{2\sigma^2}\right) \tag{3.7}$$

An important contribution that helped to put the understanding of impulse distributions on a firmer phenomenological footing was made by Suzuki [Suz77]. Suzuki reasoned that a given impulse encountered two effects. One well accepted effect was that the propagation of the signal from transmitter to receiver would undergo a fading effect due to a shadowing process. Shadow fading is also known as long term fading since it describes the mean signal level over fairly large (hundreds of carrier wavelengths) distances. Also, in the region local to the receiver, a second effect known as Rayleigh fading occurs. This is due to the scattering local to the receiver. In this case, small movements (on the order of a wavelength) of the antenna result in substantial attenuation or gain of the signal.

To picture this situation, refer to Fig. 3.1. Here we see the signal propagated from the transmitter and reflected off several dispersed obstacles. These "shadowed" rays arrive in the vicinity of the receiver having a log normal distribution. The signals of each of these arrivals then undergo local scattering which results in Rayleigh fading. The "combined" distribution that results for each impulse is the Suzuki distribution.

To understand this distribution we will review the concept of a contagious or mixture distribution [MGB74]. A simple example of a mixture distribution is as follows:

$$Z = X + Y$$

where $X$ is a binary r.v. taking the value $\mu_0$ with probability $p$, value $\mu_1$ with probability $1-p$ and $Y$ is $N(0,\sigma)$. The mixture distribution for $Z$ in this case is given by:

$$f_x(x) = (1-p)\frac{1}{\sqrt{2\pi}\sigma}e^{-\frac{1}{2\sigma^2}(x-\mu_0)^2} + p\frac{1}{\sqrt{2\pi}\sigma}e^{-\frac{1}{2\sigma^2}(x-\mu_1)^2}$$

Here we see the result is a mixture of two Gaussian random variables. The

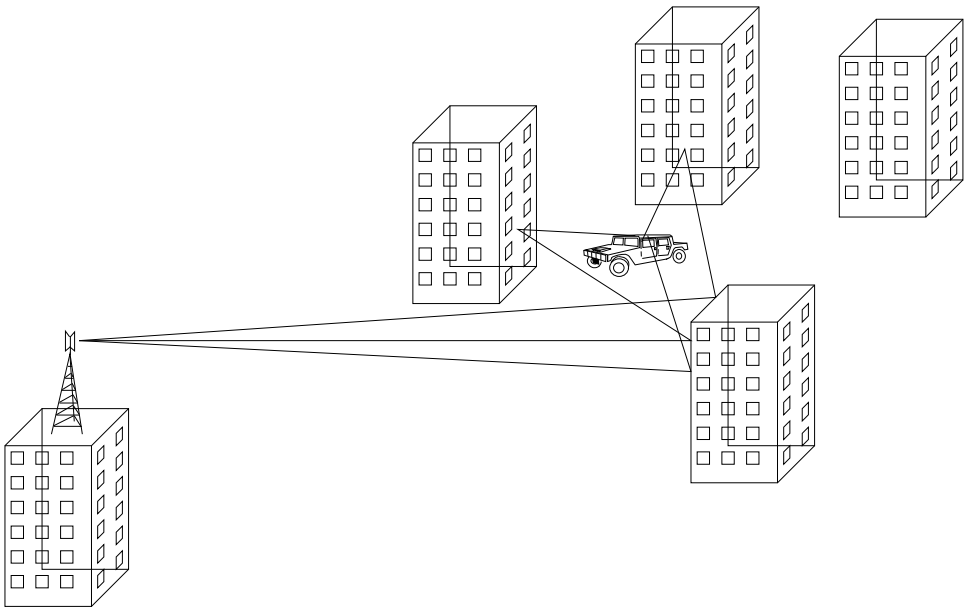

Figure 3.1: Typical wireless scenario showing shadowing multipath.

concept of a mixture can be generalized [MGB74] in the following form:

$$f_x(x) = \int_\Theta f(x|\Theta)g(\Theta)d\Theta$$

That is, given a distribution parameterized by $\Theta$ and the distribution of $\Theta$, the mixture is the product of the two integrated over the domain of $\Theta$. This is precisely what the Suzuki distribution is.

To arrive at the Suzuki distribution we start with the Rayleigh distribution whose parameter $\sigma^2$ reflects the energy that arrives in the local vicinity before scattering. But, $\sigma$ itself is also a random variable which is described by the log normal distribution. Consequently, the Suzuki density can be described by the following mixture:

$$p_x(x) = \int_0^\infty \frac{x}{\sigma^2} e^{-\frac{x^2}{2\sigma^2}} \frac{1}{\sqrt{2\pi}\sigma\lambda} e^{-\frac{(\ln\sigma-\mu)^2}{2\lambda^2}} d\sigma \tag{3.8}$$

We can integrate the above to arrive at the Suzuki distribution below:

$$P_x(x) = \int_0^\infty \left(1 - e^{-\frac{x^2}{2\sigma^2}}\right) \frac{1}{\sqrt{2\pi}\sigma\lambda} e^{-\frac{(\ln\sigma-\mu)^2}{2\lambda^2}} d\sigma \tag{3.9}$$

Regarding the above distributions, we note that if we were to use them to describe the distribution of all the impulses within the CIR then we are making the assumption that the distribution is stationary with respect to arrival time. This is similar to the assumption of time-invariance with regard to the multipath inter-arrival times that we discussed earlier. This is the approach most researchers have taken in evaluating the distribution of the impulses within a given CIR realization.

## 3.3 Channel Impulse Amplitude Distribution

In Section 3.1 we noted that the research prior to the present time has implicitly assumed the time-invariance of the impulses within the CIR. This clearly cannot be the case since the impulses die out over time. In this section we will show, from a phenomenological point of view, a distribution that fully describes the distribution of impulses within the CIR.

In the previous section we pointed out how Suzuki described the distribution for a single impulse within the CIR. This distribution put our understanding on a firm phenomenological basis for a specific impulse. We begin with this distribution (which is the distribution on the impulse magnitude) and proceed by performing a transformation of this distribution to what we term the dB-Suzuki distribution. The transformation begins by defining $y \equiv 20log(x) = 2a \ln x$ with $a = \frac{\ln 10}{10}$. By standard means [Pap84], from this definition we can arrive at the dB-Suzuki distribution:

$$p_y(y) = \int_0^\infty \frac{1}{2a\sqrt{2\pi}\lambda} e^{\frac{y-\sigma}{a}} e^{-\frac{1}{2}e^{\frac{y-\sigma}{a}}} e^{-\frac{(\sigma-\mu)^2}{2\lambda^2}} d\sigma \tag{3.10}$$

Our purpose in performing this transformation is partly to elucidate the distribution and simplify the next step. Furthermore, the channel impulses will cover

a large dynamic range with the smaller impulses predominating. Expressing the density on the dB scale allows the smaller impulses to not be as closely packed as they would be on an absolute scale which allows for more accurate fitting of small amplitude impulses with the empirical data.

By defining $\rho \equiv 2a \ln \sigma$ and $b(\rho) \equiv \rho + a \ln 2$, we can by some further manipulation arrive at the following distribution:

$$p_y(y) = \int_{-\infty}^{\infty} \frac{1}{a} e^{\frac{1}{a}(y-b(\rho))} e^{-e^{\frac{1}{a}(y-b(\rho))}} \frac{e^{-(\rho-\mu)^2/(2\sigma^2)}}{\sqrt{2\pi}\sigma} d\rho \tag{3.11}$$

The significant thing to note here is that, expressed in the dB domain, we have a mixture of the abscissa-reversed Fisher-Tippett and Gaussian densities.

The distribution we seek, ultimately, is the distribution of an impulse selected randomly from the CIR. This must be distinguished from what we have determined so far. The present result describes the distribution of an impulse having a particular mean energy. The question remains, then, as to what the distribution of this mean is. Then we can, by another application of the mixing concept, determine the overall distribution of the impulses within the CIR.

The path loss of a received signal is generally taken to be linearly decaying with distance (in dB). Since distance translates linearly with delay we can say that, to a first approximation, the mean signal energy decays linearly (in the dB domain) with the excess delay of the arriving impulse. This then brings us to a key question. What is the distribution within the CIR of arrival times? Assuming that arrivals have an exponential inter-arrival time distribution, if we collect arrivals occurring within a window (presumably the window is large enough so that significant impulses that we may be interested in do not occur outside the window) it is straightforward to show that the arrival times have a uniform distribution within the interval of the window.

Knowing that the arrivals have a uniform distribution, we then conclude that

the mean path loss is also uniformly distributed (in the dB domain) over some range $s < \mu < t$. The overall density for the CIR can then be expressed as the following mixture (where $t > s$):

$$p_z(z) = \int_s^t \frac{1}{t-s} p_y(z|\mu) d\mu \tag{3.12}$$

We note that the prior expression for $p_y(y)$ is, in fact, dependent on $\mu$.

### 3.3.1 A Useful Approximation

In the equation for the dB-Suzuki density, we note that this mixture represents a convolution of the Fisher-Tippett density with the Normal density. From this observation we can conclude that for $\sigma >> a$ the dB-Suzuki density has an approximately Normal density. Furthermore, because we are dealing with the convolution of two densities, we can conclude that we are dealing with the sum of two independent random variables. In this case one random variable has the Fisher-Tippett distribution and the other a Normal. Thus, the mean of the sum is the sum of the means and similarly for the variance of the sum. So, the mean and variance for the approximated Gaussian is given by the following:

$$\mu_{dBSuzuki} = \mu - a(\gamma - \ln 2) \tag{3.13}$$

and

$$\sigma^2_{dBSuzuki} = \sigma^2 + \frac{a^2\pi^2}{6} \tag{3.14}$$

where $\gamma$ is Euler's constant.

These observations explain why we opted earlier to perform the transformation to the dB-Suzuki distribution. This transformation ultimately resulted in the observation that a convolution was embedded in the expression for the mixture. This then enabled us to conveniently derive the parameters for the Normal

approximation given here.

Then, under the condition of $\sigma >> a$, we can immediately arrive at the following convenient form for the density of the impulses within the CIR:

$$p_y(y) = \frac{1}{t-s}[Q(r(t)) - Q(r(s))] \tag{3.15}$$

where $r(x) = \frac{x-a(\gamma-\ln 2)-y}{\sigma_{dBSuzuki}}$ and $Q(x) = \int_x^\infty \frac{1}{\sqrt{2\pi}e^{-y^2/2}dy}$.

## 3.4 Results

In [YM91] the objective was to obtain the parameters of the lognormal distribution which provided the best fit to the distribution of the channel impulses. Using the original data collected in [YM91], these figures are reproduced in Figs. 3.2 and 3.3 for the indoor LOS and obstructed cases respectively. In [YM91] the cost function used to adapt the distributional parameters is the distribution mean squared error:

$$C = \int_{-\infty}^{\infty} \left[\hat{F}(x) - F(x)\right]^2 f(x)dx \tag{3.16}$$

where $\hat{F}(x)$ is the empirical distribution, $F(x)$ and $f(x)$ are the "target's" distribution and density, respectively. In [Suz77] the fitting was performed by equating the mean and variance of the empirical distributions with the candidate distributions. A Cramer-Von Mises test was then performed to determine if the empirical distribution is a likely fit to the candidate distribution.

Although [YM91] uses the MSE as a cost function for the candidate distribution with respect to the empirical, we might not wish to restrict ourselves to this particular choice. This is merely one of many possible cost functions. Another possible choice is the following:

$$C = \int_{-\infty}^{\infty} 10^{x/10} \left[\hat{F}(x) - F(x)\right]^2 f(x)dx \tag{3.17}$$

If we regard all signals as equally "important", then the MSE is a reasonable choice for a weighting function. However, in designing communication systems, it is primarily the strong impulses that we wish to model with reasonable accuracy. So, in that spirit, the suggested cost function in (3.17) is presented. In this case, we see that this is an energy-weighted MSE. Consequently, minimization by this cost function will result in distributions that favor accuracy in the right tail of the distribution over the left tail.

For the density proposed in (3.15) we minimized the distributional error according to the cost function of (3.16). We present our fits in Figs. 3.4 and 3.5. Comparing these to those shown in Figs. 3.2 and 3.3 we see that the new distri-

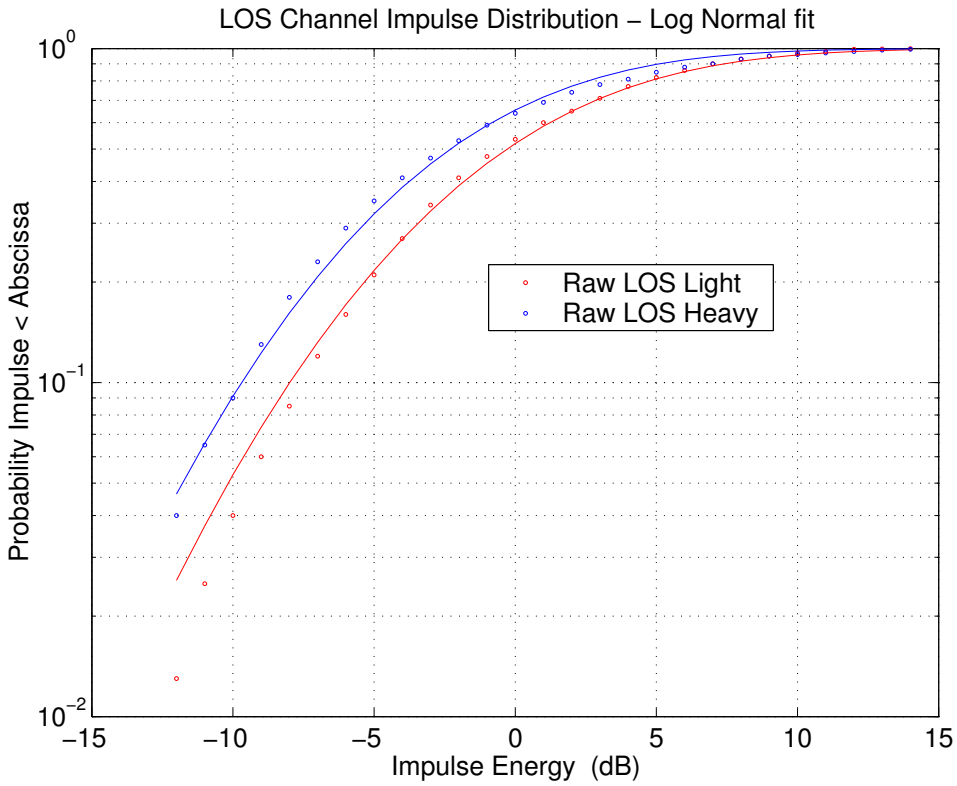


Figure 3.2: Original lognormal distribution fit for LOS case.

bution provides a better fit to the empirical data than the lognormal distribution.

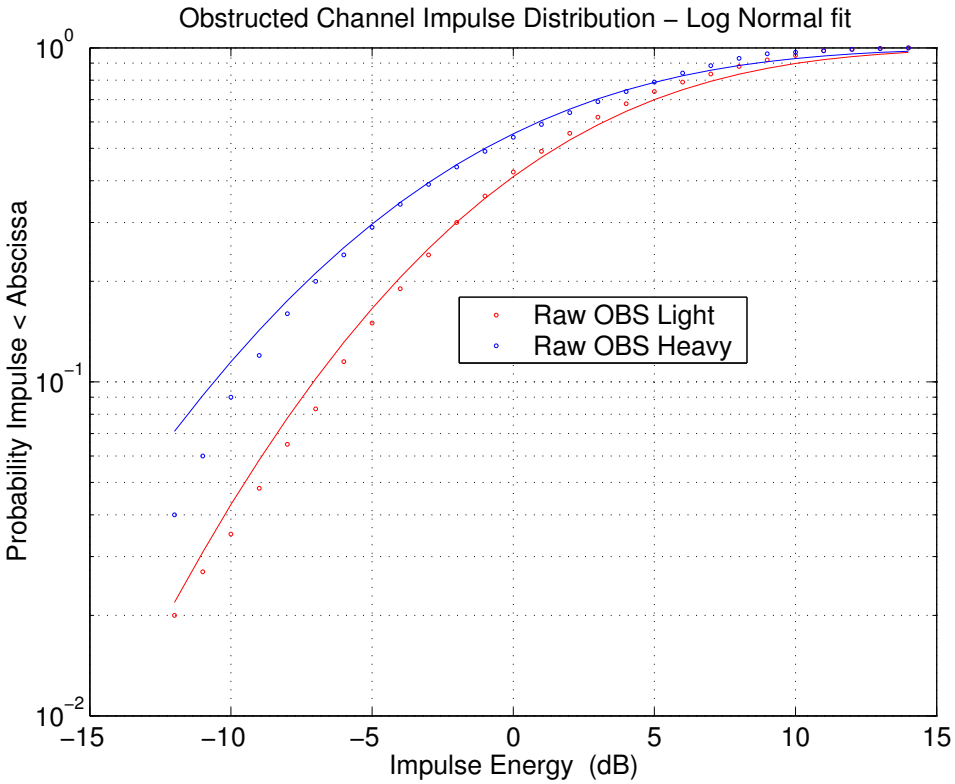


Figure 3.3: Original lognormal distribution fit for Obstructed case.

As we pointed out with regard to arrival times, one reason is that the new distri-

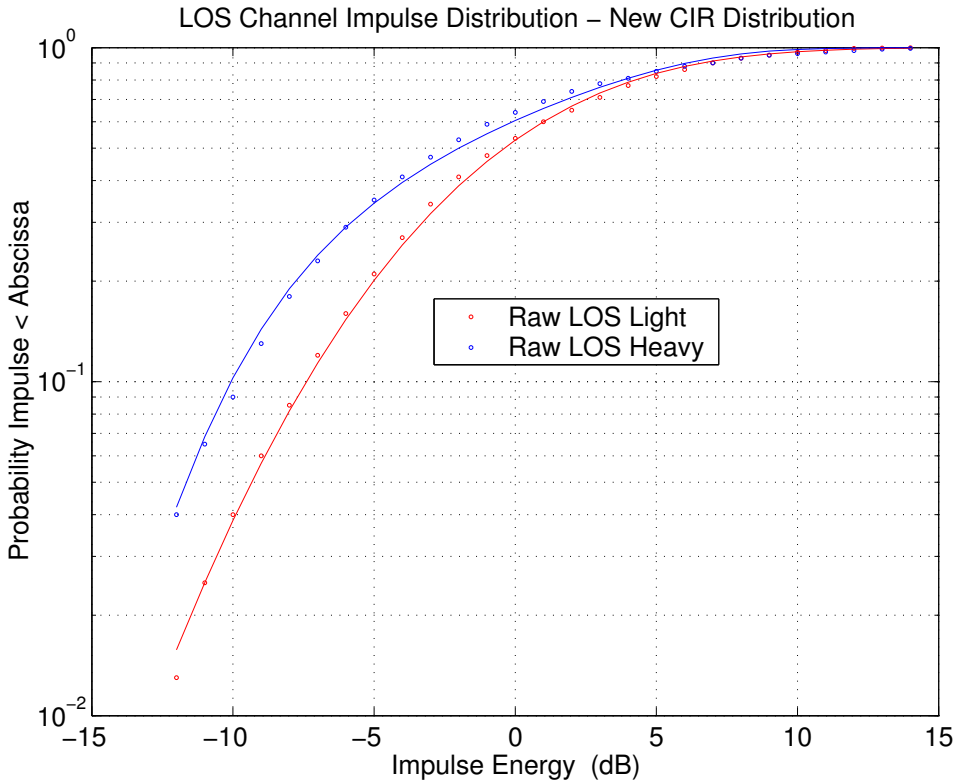


Figure 3.4: New distribution fit for LOS case.

bution provides an additional modelling degree-of-freedom. Another is, of course, that the new distribution follows from a more rigorous phenomenological basis.

## 3.5 Conclusion

In this chapter we have focused on deriving, from a phenomenological perspective, the distribution of impulses occurring within the CIR. This work was founded on Suzuki's original work showing that the distribution of an impulse having a particular mean path loss and shadowing variance follows the Suzuki distribution. We extended this distribution by observing that the distribution of the mean path

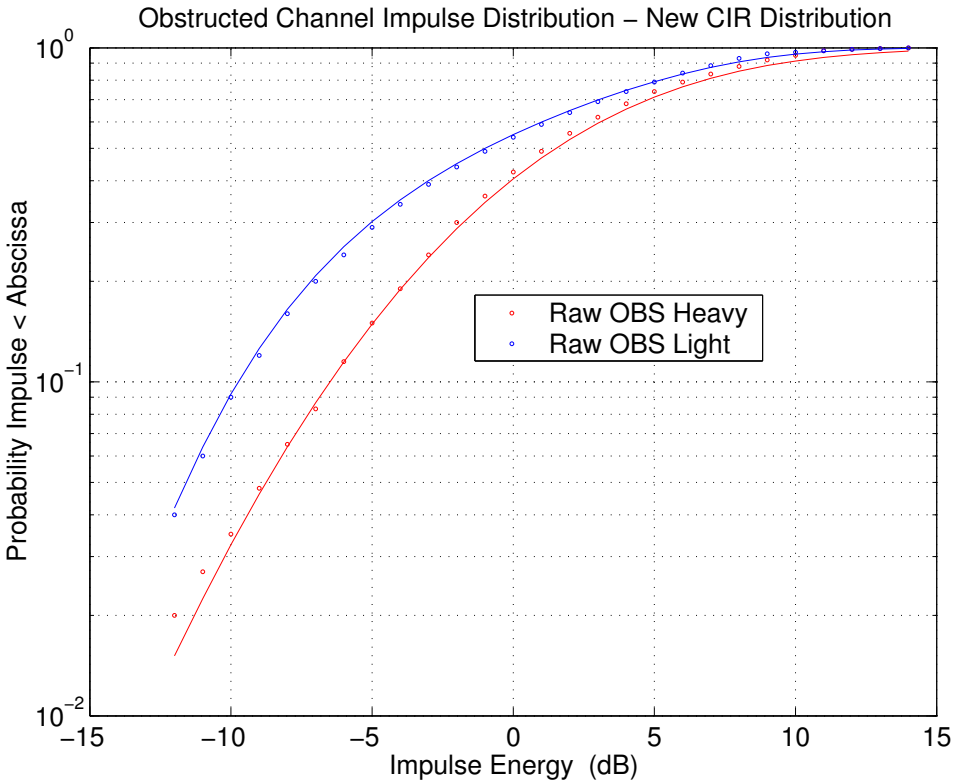


Figure 3.5: New distribution fit for Obstructed case.

loss is uniform under a Poisson arrival assumption. This resulted in a mixture of the dB-Suzuki and uniform densities which can, for large shadowing variance, be simplified by approximation. We then compared our distribution to results published for various combinations of obstructed and LOS scenarios and degree of clutter. Here we noted that the empirical distributions drop very rapidly at the low end of the impulse energy scale compared to our distribution as well as other researcher's best-fit distributions. We pointed out that this is almost entirely due to the fact that the empirical distribution is effectively truncated whereas the theoretical densities are not. When accounting for truncation in the theoretical distributions, better fits are obtained. Finally, we noted that the results presented in previous research do not supply any information regarding the "goodness-of-fit" in the high-end of the energy scale. Considering that half of the channel energy is expected to be 10 dB above the median impulse amplitude and greater (for a -12 dB truncation), having an accurate description of this part of the CIR density seems imperative - which could be an area of future research.

## 3.6 Derivation of dB-Suzuki Density

We begin with the Suzuki density given below:

$$p_x(x) = \int_0^\infty \frac{x}{\sigma^2} e^{-\frac{x^2}{2\sigma^2}} \frac{1}{\sqrt{2\pi}\sigma\lambda} e^{-\frac{(\ln\sigma-\mu)^2}{2\lambda^2}} d\sigma \tag{3.18}$$

We first desire the dB-Suzuki density which requires that the argument $x$ be transformed to the dB scale by the following expression:

$$y \equiv 20\log x = 2a\ln x$$

where:

$$a \equiv \frac{10}{\ln 10}$$

We define the prior function of x and its associated root as:

$$y = g(x)$$

and

$$x_1 = g^{-1}(y)$$

It is well known [Pap84] that the density of a function (having a single root) is given by the following:

$$f_y(y) \equiv \frac{f_x(x_1)}{|g'(x_1)|}$$

The derivative of $g(x)$ is:

$$g'(x) = \frac{2a}{x}$$

and the root of $g(x) is$ :

$$x_1 = e^{\frac{1}{2a}y}$$

By substitution we obtain the dB-Suzuki density:

$$p_y(y) = \int_0^\infty \frac{1}{2a\sigma^2} e^{\frac{1}{a}y} e^{-\frac{1}{2\sigma^2}e^{\frac{1}{a}y}} \frac{1}{\sqrt{2\pi}\sigma\lambda} e^{-\frac{(\ln\sigma-\mu)^2}{2\lambda^2}} d\sigma \tag{3.19}$$

We can continue our derivation to arrive at a more instructive version of this density. To do this we now make the following change of variable:

$$\rho \equiv 2a \ln\sigma$$

and perform the necessary algebra to arrive at the following:

$$p_y(y) = \int_{-\infty}^\infty \frac{1}{a} e^{\frac{1}{a}(y-b(\rho))} e^{-e^{\frac{1}{a}(y-b(\rho))}} \frac{e^{-(\frac{\rho}{2a}-\mu)^2/(2\lambda^2)}}{\sqrt{2\pi}2a\lambda} d\rho \tag{3.20}$$

where:

$$b(\rho) \equiv \rho + a\ln(2)$$

Define the following:

$$\sigma \equiv 2a\lambda$$

Noting that $\mu$ is an open parameter (that is, allowing its definition to be context-dependent) we finally obtain:

$$p_y(y) = \int_{-\infty}^{\infty} \frac{1}{a} e^{\frac{1}{a}(y-b(\rho))} e^{-e^{\frac{1}{a}(y-b(\rho))}} \frac{e^{-(\rho-\mu)^2/(2\sigma^2)}}{\sqrt{2\pi}\sigma} d\rho \tag{3.21}$$

# CHAPTER 4

# Order Statistics and the Channel Impulse Response Amplitude

## 4.1 Introduction

The statistical properties of the channel impulse response (CIR) have been studied extensively from the perspective of both arrival times and impulse amplitudes. This focus has been on obtaining distributions which accurately describe these features. However, relatively little has been done to obtain the statistics of the largest impulses within the CIR. Consequently, an important contribution may be made with respect to characterizing the statistics of these largest and most significant impulses. This chapter addresses this using order statistics. It also provides some application of these results to a practical design question.

We begin with an introduction to the theory of order statistics in Section 4.2. Then, in Section 4.3, we present a brief introduction to the subject of the asymptotics of order statistics which forms the basis of extreme value theory (EVT). Since our analysis will be restricted to the application of order statistics, we present this material for possible use in future research on this topic. In Section 4.4 we consider the application of order statistics to the subject of the ordered impulse magnitudes contained in the CIR. In Section 4.5 we use the results derived in Section 4.4 to obtain the distribution of the sum of the energies

of the largest $m$ impulses within the CIR. We are interested in this particular statistic because it precisely represents the performance of a RAKE receiver. A RAKE receiver performs a search over the delay spread to acquire the signal arriving via the strongest $m$ impulses within the CIR. The energy is combined by maximal ratio combining which implies that the performance is determined by summing the total energy for all taps input into the combiner.

In Section 4.6 we compare the probability of exceedance for the energy sum derived using the theory of order statistics with diversity theory. We also make these comparisons using both the exponential as well as lognormal distributions as the distributions representing the distribution of the impulses in the CIR. Finally, we present our conclusions in Section 4.7.

## 4.2 Introduction to Order Statistics - Basic Results

Prior to discussing the application of order statistics to the CIR, we first review some basics. Consider a sequence of random numbers $X_1, X_2, ..., X_n$ of length n sampled from a distribution function $F(\cdot)$. Sort these in increasing order to obtain the sequence $Y_1, Y_2, ..., Y_n$. The sequence $Y_1, Y_2, ..., Y_n$ is said to be the *order statistics* corresponding to the random sequence $X_1, X_2, ..., X_n$.

Given the distribution of $X$, the distribution of $Y_i$ is given by the following [MGB74]:

$$F_{Y_i}(y) = \sum_{j=i}^{n} \binom{n}{j} [F(y)]^j [1 - F(y)]^{n-j} \tag{4.1}$$

From this, the distributions of the extreme values easily follow:

$$F_{Y_n}(y) = F(y)^n \tag{4.2}$$

and

$$F_{Y_1}(y) = 1 - [1 - F(y)]^n \tag{4.3}$$

The density for the $j^{th}$ order statistic is:

$$f_{Y_j}(y) = \frac{n!}{((j-1)!(n-j)!)}[F(y)]^{j-1}[1-F(y)]^{n-j}f(y) \tag{4.4}$$

and the joint density of any two order statistics such that $1 \leq j \leq k \leq n$ is:

$$f_{Y_j,Y_k}(x,y) = \frac{n!}{(j-1)!(k-j-1)!(n-k)!}Q_{j,k}(x,y) \tag{4.5}$$

for $x < y$ and $f_{Y_j,Y_k}(x,y) = 0$ for $x \geq y$. Where:

$$Q_{j,k}(x,y) = F(x)^{j-1}[F(y)-F(x)]^{k-j-1}[1-F(y)]^{n-k}f(x)f(y) \tag{4.6}$$

Finally, if the $X_i$'s were selected independently then, the joint density of the $Y_i$'s is:

$$f_{Y_1,...,Y_n}(y_1,...,y_n) = \begin{matrix} n!f(y_1).....f(y_n) & y_1 < y_2 < ... < y_n \\ 0 & otherwise \end{matrix} \tag{4.7}$$

From the joint density above, it is straightforward to show that order statistics possess the Markov property. That is, the statistics $Y_1,...,Y_{j-1}$ are independent of $Y_{j+1},...,Y_n$ given $Y_j$.

## 4.3 Asymptotic Properties of Order Statistics

The preceding section presented a number of fundamental results for studying order statistics. Now, we would like to consider the possibility that the distributions of the most extreme elements of a sequence may have an asymptotic limiting distribution (assuming we use the appropriate centering and normalization constants). More formally we can state this as the following assertion:

$$\lim_{n\to\infty} P\left(\frac{Z_n - a_n}{b_n} < z\right) = \lim_{n\to\infty} H_n(a_n + b_n z) = H(z) \tag{4.8}$$

In introducing this topic the natural question to ask is, "why are we interested in the asymptotic limiting distribution, if we already know the exact distribution?"

The answer to this is that we, in contradiction to the original question, may actually not know the original distribution. Furthermore, it may be more convenient to deal with the limiting distribution than to derive, from first principles, an exact order-statistic distribution based on the exact underlying distribution. A practical application of this is that, from a sampled distribution function of extreme values, we might obtain the appropriate centering and normalizing constants.

In [Gal87] a number of results pertinent to asymptotic distributions of extreme value statistics can be found. We will briefly summarize those pertinent to this chapter.

First, it has been shown that there are only three limiting distributions for extreme value statistics that exist [Gal87]. For our purposes, and because this is the distribution that occurs most frequently as a limiting distribution to some well known distributions, we state only one distribution which we denote:

$$H_3(x) = exp(-e^{-x}) \tag{4.9}$$

The normalizing parameters for a particular sample size $n$ are given by:

$$a_n = F^{-1}\left(\frac{n-1}{n}\right) \tag{4.10}$$

and

$$b_n = R(a_n) \tag{4.11}$$

where $F^{-1}(\cdot)$ represents the inverse CDF and

$$R(t) = (1 - F(t))^{-1} \int_t^{\infty} (1 - F(y))dy \tag{4.12}$$

The necessary conditions for convergence to this distribution are that (4.12) is finite and:

$$\lim_{t \to \infty} \frac{1 - F(t + xR(t))}{1 - F(t)} = e^{-x} \tag{4.13}$$

The exponential distribution falls within the "domain of attraction" of the above asymptotic distribution which may be shown, in spite of the limit, by establishing the above equivalence.

## 4.4 Order Statistics and the CIR Amplitude

As was stated in the introduction, the primary focus of research into the distribution of the CIR amplitudes has been on finding distributions that best fit empirically measured distributions. In this chapter we seek to utilize order statistics to gain a better understanding of the CIR and pertinent statistics relevant to radio design. But, before we proceed, it is important that we understand how these empirical distributions are determined.

To determine a typical CIR, receiver and transmitter antennae are set up at some fixed spatial interval. Wide band measurements are then made - perhaps using spread spectrum modulation and the "sliding-correlator" technique at the receiver. This is done over the delay domain of significant channel response. Following this, a peak-selection algorithm is run to determine the time-location and amplitude of each of the impulses within the CIR. Then the amplitudes of these peaks are tossed into a "bin" - note that amplitudes less than some threshold are ignored. This process is repeated many times for different locations maintaining the same spatial separation (also the same general environment - i.e. LOS, clutter, etc.). Finally, the impulses within this bin are used in creating a histogram or empirical density.

Now, in approaching the subject of determining the appropriate distribution of the CIR, a number of researchers have utilized several convenient distributions in order to "fit" the empirical data described above. The motivation for this is

that there is at least some physical justification for the distributions utilized. For example, the lognormal, Rayleigh, and Suzuki distributions have been suggested for fitting the data. But, we need to point out that these distributions only address part of the overall physical situation. In the case of the Rayleigh, only the short-term fading issue is accounted. Long-term (a.k.a. shadow) fading is described by the lognormal distribution. And, finally, the Suzuki describes a combination of the two.

But, because the CIR is a time sequence, it therefore represents a different receiver-transmitter antenna separation from tap to tap and hence will experience independent shadow fading from tap to tap. Similarly the Rayleigh fading will undergo independent fading from one tap to another. Finally, as we traverse the CIR from beginning to end, we expect the nominal path loss to increase. Consequently, the parameters of the Rayleigh and lognormal distributions cannot be considered stationary as we traverse the delay index of the CIR. This observation led to the development of the distribution described in Chapter 3.

The fitting approach utilizes a cost function that measures the error-cost of a particular distribution function compared to the empirical data. The cost function most used is based on the MSE criteria. The appropriate expression for the current context is:

$$C = \int_{-\infty}^{\infty} \left[\hat{F}(x) - F(x)\right]^2 f(x)dx$$

Before we proceed further we should mention that although [YM91] uses the MSE as a cost function for the candidate distribution with respect to the empirical, this may not be the best choice considering our intended application. Since we will likely be most interested in the largest taps, it would stand to reason that we should pay more attention to accurate modelling of the right tail of the channel impulse distribution.

Another approach was presented in Chapter 3 which seeks to obtain the distribution by basing the statistical analysis on a more rigorous phenomenological basis. That is, as mentioned above, the analysis considers the three types of fading - path loss, shadow fading, and Rayleigh fading - and obtains a distribution based on a mixture of the uniform, Log-normal, and Rayleigh distributions. For reference, this distribution is reproduced:

$$p_z(z) = \int_s^t \frac{1}{t-s} p_y(z|\mu) d\mu \tag{4.14}$$

where $\sigma$ represents the shadowing standard deviation in dB and where:

$$p_y(y|\mu) = \int_{-\infty}^{\infty} \frac{1}{a} e^{\frac{1}{a}(y-b(\rho))} e^{-e^{\frac{1}{a}(y-b(\rho))}} \frac{e^{-(\rho-\mu)^2/(2\sigma^2)}}{\sqrt{2\pi}\sigma} d\rho \tag{4.15}$$

and the variables $t$ and $s$ ($t > s$) represent the beginning and end of the uniform path loss distribution.

It was shown in Chapter 3 that this distribution provided a better fit than past attempts. This is partly because the prior attempts did not account for the fact that as we vary the delay the distribution of the impulses is not stationary. After incorporating this effect it is now possible to provide a significantly better fit. Another reason is, simply, that this distribution has three parameters with which to fit the empirical data.

Now, having a distribution which can accurately represent the CIR, we now can turn our attention to the determination of some further key distributions that will aid our analysis of the CIR response.

### 4.4.1 Distribution of Largest Taps

The distribution $H^{(k)}(x)$ for the $k^{th}$ largest tap is given as [Gal87]:

$$H^{(k)}(x) = H(x) \sum_{t=0}^{k-1} \frac{1}{t!} \left[-\ln H(x)\right]^t \tag{4.16}$$

where $H(x)$ is the appropriate limiting distribution for $F(x)$ and its associated density is:

$$h^{(k)}(x) = \frac{e^{-xk}}{(k-1)!}H(x) \tag{4.17}$$

From the distribution given in (4.14) we can employ (4.10) and (4.11) to generate the location and scale parameters $a_n$ and $b_n$ respectively. We have also provided the derivation of mean and second moment in Section 4.8.

### 4.4.2 Distribution of Sum of Largest (Smallest) Taps

One distribution that we shall find useful in the analysis to follow is the distribution of the sum of largest or smallest extremes. That is, we seek the following:

$$P\{Z < t\} = P\left\{\sum_{i=r}^{n} X_{i:n} < t\right\} \tag{4.18}$$

where $Z \equiv \sum_{i=r}^{n} X_{i:n}\ for\ (n > r)$ is the sum of the largest $n-r+1$ order statistics and $X_{i:n}$ is the $i^{th}$ smallest order statistic of the statistics $X_i$ drawn i.i.d. from a distribution F(x). This distribution may be written by conditioning on the $r^{th}$ smallest statistic:

$$P\left\{Z < t\right\} = \int_{x\in\aleph} P\left\{\sum_{i=r}^{n} X_{i:n} < t | X_{r:n} = x\right\} dQ_{r:n}(x) \tag{4.19}$$

where $Q_{r:n}(x)$ is the distribution of the $r^{th}$ smallest. Continuing, we have:

$$P\left\{Z < t\right\} = \int_{x\in\aleph} P\left\{\sum_{i=r+1}^{n} X_{i:n} < t - x\right\} dQ_{r:n}(x) \tag{4.20}$$

At this point, we recognize that because of the conditioning by $X_{r:n} = x$, that the $X_{i:n}$'s have been drawn from a distribution left-truncated at $x$ which we shall refer to as $F_{x,l}(y)$. Consequently, we define $Y_{i:n-r} \equiv X_{i+r:n}$ which is taken from the distribution $F_{x,l}(y)$. Making this substitution we have:

$$P\{Z < t\} = \int_{x\in\aleph} P\left\{\sum_{i=1}^{n-r} Y_{i:n-r} < t - x\right\} dQ_{r:n}(x) \tag{4.21}$$

Since all $n-r$ order statistics are represented in the summation, the dependence created by ordering is nullified and we can equivalently say that the sum is of i.i.d. statistics $Y_i$ taken the from the distribution $F_{x,l}(y)$:

$$P\{Z < t\} = \int_{x \in \aleph} P\left\{ \sum_{i=1}^{n-r} Y_i < t - x \right\} dQ_{r:n}(x) \tag{4.22}$$

The density of the sum may now be computed by convolution since the random variables are independent.

We have just determined the distribution of the sum of the largest extremes. To arrive at the distribution of the smallest extremes we follow a similar approach except that $F_{x,r}(y)$ represents a distribution right-truncated at $x$.

### 4.4.3 Distribution of Signal to Interference Plus Noise Ratio

Using the results of the prior section we can determine another useful distribution - that of the SINR. In this case it can be stated as the following:

$$P\{Z < t\} = P\left\{ \frac{\sum_{i=r}^{n} X_{i:n}}{N + \frac{1}{M}\sum_{i=1}^{r-1} X_{i:n}} < t \right\} \tag{4.23}$$

where $N$ is the total noise and $M$ represents the processing gain. To arrive at this result, we begin by considering the following joint distribution:

$$P\{Y < y, Z < z\} = P\left\{ \sum_{i=r}^{n} X_{i:n} < y, N + \frac{1}{M}\sum_{i=1}^{r-1} X_{i:n} < z \right\} \tag{4.24}$$

for $z > N$ where we define $Y = \sum_{i=r}^{n} X_{i:n}$ and $Z = N + \frac{1}{M}\sum_{i=1}^{r-1} X_{i:n}$. We again condition on the $r^{th}$ smallest:

$$= \int_{\aleph} P\left\{ \sum_{i=r+1}^{n} X_{i:n} < y - x,\ \sum_{i=1}^{r-1} X_{i:n} < M(z - N) \right\} dQ_{r:n}(x) \tag{4.25}$$

By conditioning on the $r^{th}$ smallest, the sum on the right is conditionally independent of the sum on the left according to the Markov property of order statistics.

We also note that the random variables contained in the sum on the left were drawn from a distribution, $F_{x,l}(y)$, which was derived by truncating $F(x)$ on the left at $x$. The random variables contained in the sum on the right are drawn from a distribution $F_{x,r}(y)$, which was derived by truncating $F(x)$ on the right at the point $x$.

Because of the conditional independence, we can write:

$$= \int_{\aleph} P\left\{\sum_{i=r+1}^{n} X_{i:n} < y - x\right\} P\left\{\sum_{i=1}^{r-1} X_{i:n} < M(z-N)\right\} dQ_{r:n}(x) \tag{4.26}$$

Next, we define $Y_{i:n-r} \equiv X_{i+r:n}$ for the first sum and $Y_{i:r-1} \equiv X_{i:n}$ for the second to yield:

$$= \int_{\aleph} P\left\{\sum_{i=1}^{n-r} Y_{i:n-r} < y - x\right\} P\left\{\sum_{i=1}^{r-1} Y_{i:r-1} < M(z-N)\right\} dQ_{r:n}(x) \tag{4.27}$$

Finally, we make the observation that the distribution of both sums can be viewed as the sums of i.i.d. random variables, as in the previous section, which brings us to the final joint distribution:

$$= \int_{\aleph} P\left\{\sum_{i=1}^{n-r} Y_i < y - x\right\} P\left\{\sum_{i=1}^{r-1} Y_i < M(z-N)\right\} dQ_{r:n}(x) \tag{4.28}$$

for $z > N$. Defining $T = \frac{Y}{Z}$, we can find the density of T using the following:

$$f_T(t) = \int_{-\infty}^{\infty} |z| f_{Y,Z}(tz, z) dz \tag{4.29}$$

where $f_{Y,Z}(y,z)$ is joint density corresponding to the previous joint distribution $f_{Y,Z}(y,z) = \frac{\partial^2}{\partial y \partial y} P\{Y < y, Z < z\}$.

## 4.5 Comparison to Design Diversity

In the design of radio systems fading is one of the predominant impairments. Because of the prevalence of fading, diversity is frequently harnessed to moderate this effect. There are many forms of diversity that may be employed. For

OFDM systems operating in a frequency-selective environment, information may be spread across multiple sub-channels thus realizing frequency diversity. For MIMO systems, multiple antennas are available at both the receiver and transmitter and are spatially arranged so as to provide signal independence between the various receiver-transmitter antenna pairs in the spatial domain. Finally, CDMA affords an opportunity to realize some diversity through the time domain. This occurs in environments where there may be multiple resolvable multipath arrivals. In this case, a RAKE receiver may be employed to harness and combine the energy among highest energy arrivals.

To exemplify how we might apply the statistics generated so far we will consider the typical approach to diversity design. In particular we will consider a RAKE receiver. Although it is true that each tap fades independently of the others in the time dimension, conventional analysis also implicitly assumes that each of the branches in a diversity combiner are selected from the same distribution. This is not truly the case since in a RAKE implementation we search for the strongest $m$ taps available within the CIR of length $n$. The resulting sequence of statistics are known, as we have explained above, to be non-stationary because they are *ordered*. This issue is further emphasized because the distribution of each tap's energy is not stationary with increasing delay - this is implicitly demonstrated by the density shown in (4.15) by the dependence on $\mu$.

Our investigation will be as follows. Diversity analysis often assumes an exponential basis distribution. On this account we first analytically determine the sum-of-extremes distribution based on an exponential distribution. In this case we are able to obtain a closed-form solution. We then consider the sum-of-extremes case where the underlying distribution is log-normal - which better approximates the distribution of the impulses within the CIR than the exponen-

tial. In this case we must settle for a numerical solution. Finally, we will compare the previous two distributions to the distributions corresponding to pure-selection and maximal ratio combiners. The selection and maximal ratio combiner types are both derived from an exponential distributional assumption.

We begin our comparison by selecting parameters we might typically see in practice for the log-normal distributed CIR ($\mu = 2.30$ (10 dB), $\sigma = 1.52$ (6.6 dB), number of impulses equal to 15 and up to four-branch combiner). Then, in order to normalize our results, we determine the mean of this log-normal distribution and use it for selecting the mean for our exponential distribution mentioned above (mean=31.62). The derivation of the sum-of-extremes distribution for the exponential basis can be found in Section 4.9.

## 4.6 Results

In the following figures, we show the results of our analyses. In Fig. 4.1 we compare the sum-of-extremes with the selection and maximal ratio diversity schemes in the case of the exponential basis distribution. The cases we considered were for one, two, three, and four branch diversity RAKE/MRC with 15 impulses within the CIR. In this case we note that the single-branch case overlays the result for the pure-selection diversity diversity as we would expect since the traditional expression for selection diversity is based on the exponential distribution (this was obtained by simulation since the expression in Section 4.9 only covers multi-tap cases). The other extreme corresponds to the case where we combine all 15 of the channel taps - this is the 15-branch MRC case. We note that in between the pure-selection and MRC curves we have the sum-of-extremes cases corresponding to the two, three, and four tap cases. From examination of these it is clear that increasing the number of taps results in the usual diminishing return for the

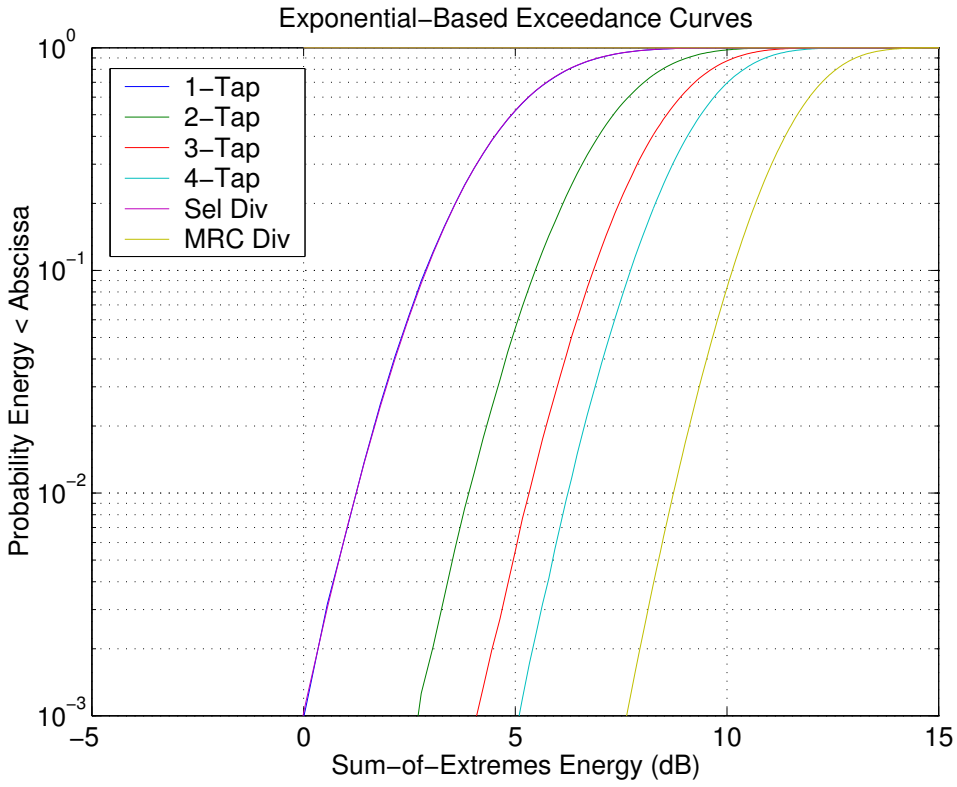


Figure 4.1: Exponential-Based Analysis

additional complexity.

In Fig. 4.2 we compare the sum-of-extremes with the selection and maximal ratio diversity schemes in the case of the more realistic log-normal basis distribution. Again, the cases we considered were for one, two, three, and four branch diversity RAKE with 15 impulses within the CIR. In this case there is a clear distinction between the "shape" of the log-normal basis curves and the exponential basis curves. Using the log-normal as a basis it appears that at the lower SNR regions (i.e. near the link margin) that for the same SNR the log-normal curve shows as much as an order of magnitude difference in exceedance probability compared to the corresponding exponential basis. Alternatively, for the same exceedance probability, analysis based on the exponential basis is optimistic

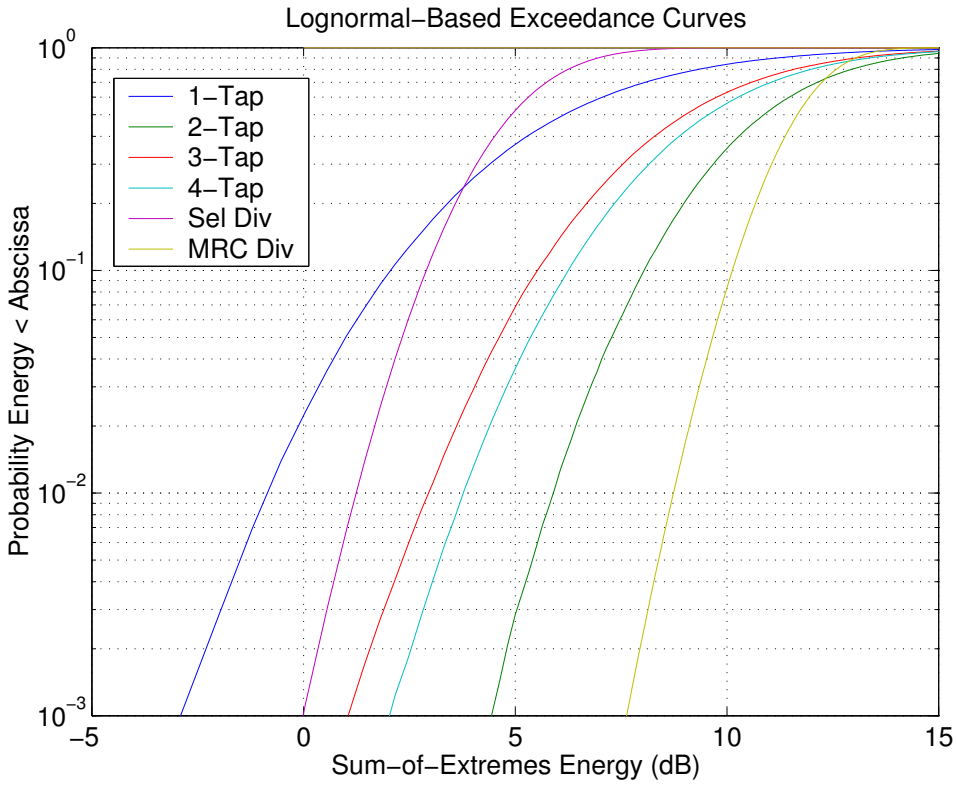


Figure 4.2: Lognormal-Based Analysis

by approximately 2 dB (at about 1% exceedance probability) compared to the corresponding more realistic log-normal basis.

## 4.7 Conclusion

In this chapter we have considered the application of order statistics and extreme value theory to a diversity design problem involving a RAKE receiver. We compared conventional diversity outage analysis to a more accurate method which accounts for the non-stationarity of the statistics of the impulses within the CIR. This was done by utilizing the log-normal distribution as our analytical basis.

We observed that for realistic channel parameter choices the conventional

analysis using an exponential distributional basis appears to be optimistic with respect to our more realistic analysis based on the log-normal distribution of the channel impulses. This result is expected since, in the exponential case we were dealing with what was thought to be a stationary distribution with respect to each impulse used in the combiner. Since what we actually have is non-stationary gradation (along the delay dimension) resulting in an overall distribution closer to lognormal, we expect to see something that looks like a decrease in effective diversity. That is, we expect to see a "flatter" appearance of the plotted distributions. This is precisely the case in the curves presented.

In addition to our application of order statistics to the RAKE receiver problem described in this chapter there are, no doubt many other similar applications. One application is in the area of power engineering. In this case we may envision power demands as arrivals with some associated amplitude. The sequence of amplitudes may be collected over some period of time and then ordered. The statistics for the largest is of obvious interest.

Another application in the area of digital communications is with respect to the decision feedback equalizer. In this application, we begin with the statistics of the impulse response of the channel plus feed-forward filter. We then form the ratio of the maximum tap energy to the total channel energy. This statistic is of interest since it expresses the loss in performance with respect to the MLSE decoder.

One final application is with respect to OFDM. As was mentioned in Chapter 2 Section 2.2.3, an important impairment in OFDM is due to the peak to average power (PAR) problem. This is because the design linearity of the power amplifier within the transmitter and dynamic range within the receiver and dictated by this figure. In this case, we are interested in knowing the distribution of the peak

instantaneous power. The reason for this is that although we can compute the peak power knowing the constellation size and OFDM symbol length, using this figure for design purposes may be overly conservative since this is a particularly remote event. We may prefer to ignore these remote events and suffer the attendant distortion, but focus our efforts of the more prevalent cases. A distribution of the peak power would be helpful to aid in focusing on these more prevalent cases.

## 4.8 The first and second moments for the kth extreme

Starting with the definition of the mean for $k^{th}$ extreme value we have:

$$E(Y_k) = \int_{-\infty}^{\infty} y h^{(k)}(y) dy = \int_{-\infty}^{\infty} \frac{y e^{-yk}}{(k-1)!} e^{-e^{-y}} dy \tag{4.30}$$

Then defining $z = e^{-y}$ we can make the following transformation:

$$E(Y_k) = -\int_{0}^{\infty} \frac{\ln(z) z^k}{(k-1)!} e^{-z} dz \tag{4.31}$$

Using a symbolic integration program we find the following progression in $k$:

$$\begin{aligned} k = 1 \quad &\rightarrow \quad E(Y_1) = \gamma - \tfrac{1}{1!} \\ k = 2 \quad &\rightarrow \quad E(Y_2) = \gamma - \tfrac{3}{2!} \\ k = 3 \quad &\rightarrow \quad E(Y_3) = \gamma - \tfrac{11}{3!} \\ k = 4 \quad &\rightarrow \quad E(Y_4) = \gamma - \tfrac{50}{4!} \end{aligned} \tag{4.32}$$

where $\gamma$ is the Euler-Mascheroni constant ($\gamma \approx 0.57722$). By careful inspection we can arrive at the following result:

$$E(Y_k) = \gamma - \sum_{j=1}^{k-1} \frac{1}{j} \tag{4.33}$$

If we start with the density for the centered and normalized case ($Z = a + bY$), we arrive at the following:

$$E(Y_k) = a + b\left(\gamma - \sum_{j=1}^{k-1} \frac{1}{j}\right) \tag{4.34}$$

For the second moment we perform the transformation as at the beginning for the first moment to yield:

$$E(Y_k^2) = -\int_0^\infty \frac{\ln(z)^2 z^k}{(k-1)!} e^{-z} dz \tag{4.35}$$

Using a symbolic integration program we find the following progression in $k$ (times $\frac{1}{(k-1)!}$):

$$\begin{array}{lll} k=1 & \rightarrow & E(Y_1^2) = \gamma^2 + \frac{1}{6}\pi^2 \\ k=2 & \rightarrow & E(Y_2^2) = \gamma^2 + \frac{1}{6}\pi^2 \\ k=3 & \rightarrow & E(Y_3^2) = 2 + 2\gamma^2 - 2\gamma + 2!\frac{1}{6}\pi^2 \\ k=4 & \rightarrow & E(Y_4^2) = 12 + 3!\gamma^2 - 22\gamma + 3!\frac{1}{6}\pi^2 \\ k=5 & \rightarrow & E(Y_5^2) = 70 + 4!\gamma^2 - 100\gamma + 4!\frac{1}{6}\pi^2 \\ k=6 & \rightarrow & E(Y_6^2) = 450 + 5!\gamma^2 - 548\gamma + 5!\frac{1}{6}\pi^2 \end{array} \tag{4.36}$$

By careful inspection we can arrive at the following result:

$$E(Y_k^2) = \gamma^2 + \frac{1}{6}\pi^2 - 2\gamma \sum_{j=1}^{k-1} \frac{1}{j} + 2 \sum_{n=1}^{k-2} \frac{1}{n+1} \sum_{j=1}^{n} \frac{1}{j} \tag{4.37}$$

Note that for $k = 2$ the second summation is to be taken as zero. If we start with the density for the centered and normalized case ($Z = a + bY$), we arrive at the following:

$$\begin{array}{lll} E(Y_k^2) & = & (a+\gamma b)^2 + \frac{1}{6}\pi^2 b^2 - 2\gamma \sum_{j=1}^{k-1} \frac{ab+b^2\gamma}{j} + \\ & & 2\sum_{n=1}^{k-2} \frac{2b^2}{n+1} \sum_{j=1}^{n} \frac{1}{j} \end{array} \tag{4.38}$$

## 4.9 Density of the sum-of-extremes for the exponential case

Since we are interested in the density of the sum-of-extremes we shall begin by taking the partial of (4.22) with respect to $t$. Then, noting that the elements of the summation are selected i.i.d corresponding to a distribution left-truncated at

$x$ we first obtain, by convolution, the density for this sum:

$$F_{x,l}(y) = \frac{\lambda^{n-r}}{(n-r-1)!}(y-(n-r)x)^{n-r-1}e^{-\lambda(y-kx)} \tag{4.39}$$

for $y > (n-r)x$ and where $x$ is the truncation point. The density of the $r^{th}$ order statistic is given by (4.4). We note that we could approximate this using (4.17) for large $n$. Making the substitution for the exponential density yields:

$$q_{r:n}(x) = \binom{n}{n-r} \lambda r[1-e^{-\lambda x}]^{r-1}e^{-\lambda x(n-r+1)} \tag{4.40}$$

After substituting into (4.22) our density is now:

$$f_t(t) = \Delta e^{-\lambda t}\int_0^{t/K}(t-Kx)^{n-r-1}[1-e^{-\lambda x}]^{r-1}dx \tag{4.41}$$

where

$$\Delta \equiv \binom{n}{n-r}\frac{r\lambda^K}{(n-r-1)!} \quad K \equiv n-r+1 \tag{4.42}$$

After a variable substitution and application of the binomial formula we now have:

$$f_t(t) = \frac{\Delta}{K}e^{-\lambda t}\int_0^t y^{n-r-1}\sum_{j=0}^{r-1}\binom{r-1}{j}(-1)^j e^{-\lambda' jt}e^{\lambda' jy}dy \tag{4.43}$$

Where $\lambda' = \lambda/K$. Rearranging the order of summation and integration:

$$f_t(t) = \frac{\Delta}{K}e^{-\lambda t}\sum_{j=0}^{r-1}\binom{r-1}{j}(-1)^j e^{-\lambda' jt}\int_0^t y^{n-r-1}e^{\lambda' jy}dy \tag{4.44}$$

Evaluating the integral in the prior equation by standard means yields:

$$f_t(t) = \binom{n}{n-r} r\lambda e^{-\lambda t}A \tag{4.45}$$

where

$$A = B + D \tag{4.46}$$

and

$$B = (-1)^{n-r}K^{n-r-1}\sum_{j=1}^{r-1}\binom{r-1}{j}\frac{(-1)^j}{j^{n-r}}C_j \tag{4.47}$$

and

$$C_j = e^{-\lambda' jt} - \sum_{k=0}^{n-r-1} \frac{(-\lambda' jt)^k}{k!} \tag{4.48}$$

and

$$D = \frac{(\lambda t)^{n-r}}{K!} \tag{4.49}$$

We should note that for selection of parameters that may be typically encountered in practice that evaluation of the last expression may yield numerical instabilities if quad precision is not used. So, if numerical integration is available, equation (4.44) may be necessary for environments limited to double precision.

# CHAPTER 5

# Wireless Channels, Equalization Classes, and the T-Algorithm

## 5.1 Introduction

In this chapter we focus on equalization for single-carrier systems using the MLSE approach and the T-algorithm from the family of sequential decoding (SD) algorithms. Both [Pro95d] and [Lee99] consider the performance implications of the worst case channel impulse response (CIR). In this chapter we consider the likelihood of such channels occurring based on the CIR distributions derived in an earlier chapter and determine the resulting expected loss in performance compared to the entire energy in the channel. Since $d^2_{free}$ measures this loss, we develop a new method for finding $d^2_{free}$ via the trellis weight enumerating function and also perform simulations to determine $d^2_{free}$. Finally, we simulate the T-algorithm compare its performance to MLSE and DFE bounds.

In Chapter 2 we focused on a multicarrier system operating in a high dynamic environment. The attractiveness of multicarrier systems such as OFDM stems from the ease of equalization. However, in highly mobile environments consideration needs to be given to the rate at which re-training needs to be performed. Furthermore, inter-carrier interference is a problem which results in an irreducible error floor. Therefore, at some point (Doppler to carrier wavelength ratio is a

good indicator) it is expedient to abandon multicarrier modulation schemes and reconsider single-carrier modulation. In this chapter we will be focusing our attention on single-carrier equalization schemes and focus, in particular, on MLSE via SD.

In the previous two chapters we have been investigating the statistical characteristics of wireless channels. Chapter 3 presented a statistical model which had a physically traceable origin. That chapter began with Suzuki's statistical model which was simply the mixture of two specific densities. In this case the lognormal density, which is generally accepted as an appropriate model for shadow fading, was mixed with the Rayleigh density which describes the statistics of short-term fading. This treatment was observed to reasonably describe the statistics of channel impulses within fairly short intervals. Through collection of CIR samples, Suzuki observed that the distribution was nearly lognormal.

Noting that Suzuki's distribution is theoretically applicable only over a particular point along the path loss profile, in Chapter 3 we extended this density to encompass the entire path loss profile. This was done by first converting the Suzuki density, which corresponds to absolute voltage scale, to the dB-Suzuki density which corresponds to an energy scale measured in dB. We then observed that, under the assumption of exponential interarrival times of the impulses, that the arrival times would have a uniform distribution leading to the condition in which path loss distribution (on a dB scale) would also be uniform. Then the overall density for the impulses within a channel impulses response was obtained as the mixture of the uniform density and the dB-Suzuki density.

In Chapter 4, we enlarged our study of CIR statistics to include the statistics corresponding to the extreme impulses. The distribution of the largest impulses within the CIR are clearly important to us since, under certain equalization

scenarios, these are the ones in which the equalization effort is concentrated. In that chapter we centered on one such case: The RAKE receiver. Since the RAKE receiver essentially combines the m-largest impulses of a CIR having $n$ impulses (for $n > m$), we obtained the distribution for that particular case. This yielded a family of curves reflecting exceedance probability corresponding to the different numbers of impulses combined. This was performed using an exponential basis distribution (which is the energy distribution corresponding to a Rayleigh voltage distribution). It was also performed using the lognormal distribution which, as we pointed out in the prior chapter, was the distribution that Suzuki noted as closely approximating reality. These two cases, (exponential-based exceedance and lognormal-based exceedance) were compared to show that a significant difference exists depending on the assumed distribution.

In the present chapter we will be considering the implications of channel models on the analysis and selection equalization methods. We begin by breaking down the general subject of equalization into three "classes." These classes are determined according to their relative performance potential. Within these classes we identify a number of methods and briefly describe each. Recognizing that MLSE is the top-of-the-heap performance-wise, we then consider various MLSE approaches. We conclude that for equalization of practical channels, sequential detection (SD) is the only practical complexity method. We then describe a number of SD methods for completeness. Next, we consider the performance aspects of MLSE. Noting that performance is directly tied to $d^2_{free}$, we consider methods for evaluation. The first method involves a "direct assault" on the problem by exhaustive search. This method is, of-course, computationally intensive. Another approach involves taking limits on the trellis weight enumerating function. Having noted that a number of researchers have determined that a "worst-case" channel exists for a given channel length, we then pose the question as to whether

anything near such worst-case channels occur with any frequency worth considering. We address this question by way of simulation. Finally, we conclude with a simulation of the symbol error rate performance of SD under the channel models we have been considering.

## 5.2 Equalization Classes

In the study of equalization methods we may find it useful to separate the various methods into "classes." There are many ways in which classification may be performed. The classification system that is probably of most interest is a performance-based one. Based on this approach we find that there are basically three equalization classes. We give them the following names: 1) Interference suppression, 2) Interference cancellation, and 3) Optimal processing.

Within the interference suppression regime we have the following well known equalization methods: Beam forming and the CDMA-RAKE or FHSS concepts. Classical beam forming systems perform their interference suppression within a multi-antenna environment. The "beam" is formed by weighting the complex inputs from each antenna so that they are co-phased on the desired signal. Other in-band signals are suppressed in such a system if they do not have a similar direction compared to the desired signal. In most practical applications beam forming is somewhat more complex than the previous explanation in that the weights are often determined according to a MMSE criterion and trained using an LMS or RLS tracking algorithm. Such an approach emphasizes MMSE performance over forming the beam precisely in the direction of the desired signal. This approach has the advantage in that it maximizes the signal-to-interference-ratio.

The CDMA-RAKE/FHSS approach is another method within the interference

suppression regime. In this case, the data-bearing signal is modulated by a pseudo-random code either in the frequency domain as in frequency-hopping-spread-spectrum (FHSS) or time-domain as in direct-sequence-spread-spectrum (DSSS) . In this case (whether in the frequency or time domains the effects are similar) suppression of both self-interference (due to multipath) and adjacent channel interference (due to multiple access) is achieved automatically without the aid of weighting parameters.

Orthogonal frequency division multiplexing (OFDM) can be classified as an interference suppression equalization method as well. The design of OFDM enables suppression of the interference from the previous symbols by incorporating the cyclic prefix. When an OFDM receiver is properly synchronized, the discarded cyclic prefix takes with it the inter-symbol interference.

In the interference cancellation regime, we have the following equalization methods as examples: Decision Feedback Equalization (DFE), Reduced State Sequence Equalization (RSSE [EQ89]) and Decision Feedback Sequence Equalization (DFSE). By interference cancellation we simply mean that the interference caused by ISI may be mitigated or eliminated. Since some of the channel energy is being ignored we note that a power loss will be incurred in such regimes compared to a flat channel of the same energy. Clearly, such a power loss will depend on the particular channel realization.

The well known DFE equalization system is comprised of a feedforward FIR filter, a decision device, and a feedback FIR filter. The previous decisions are used within the feedback filter to create a feedback signal that cancels the post-cursor response contained in the output of the feedforward filter. Once the lengths of the two filters have been decided[1] the coefficients are generally computed by utilizing

[1]Note that the feedback must be at least as long as the channel and a useful heuristic says that the feedforward should be about twice the length of the channel.

a training signal and computed according to an MMSE criterion. Under time-varying conditions, filter coefficient adaptation is performed via LMS or RLS.

Our next example within the interference cancellation regime is really a cross between interference cancellation and MLSE and is known as RSSE or DFSE (in the case of equalization of ISI). The system structure of the DFSE consists of a feedforward filter followed by the trellis decoder (VA) whose surviving paths are fed into a bank of decision feedback filters - one filter per branch metric calculation within the trellis decoder. The feedforward filter's transfer function is designed in such a way so that, when combined with the channel transfer function, the overall response is minimum-phase. The overall impulse response is then partitioned into two sub-sequences, the length of which is a design decision based on the tolerable complexity of the overall system. Because of the minimum-phase characteristic of the overall response, the DFE portion of the system operates on that portion of the impulse response that contains impulses of less energy than the portion that is used in the trellis decoder. This leads to the conclusion that the energy cancellation occurring in the DFSE is, in general, less than for a pure DFE resulting in an improvement in performance.

Within the optimal processing regime we have the following equalization methods: MLSE via the VA, the Reduced State VA (RSVA), the multi-trellis VA (MVA) [BM96], and SD. We shall assume the reader is familiar with the VA so we will not comment further except to say that it has been combined with or modified slightly to obtain other variants which seek to perform something approximating MLSE. In particular the RSVA and MVA algorithms fall in this category. SD approximates MLSE but cannot be rightly considered a variant of the VA (partly because many of the SD algorithms pre-date VA).

It is well known that the complexity of the VA grows exponentially with

the number of memory states. For this reason a number of alternative MLSE methods have been developed. To combat this complexity increase, the multi-trellis VA works on the premise that most wireless channels are likely to be sparse. If we take this into account there are a couple of steps we can take to minimize computational/memory complexity. First of all assuming a channel of length L and constellation size of $M$ if we suppose, for example, that there are three non-zero coefficients in the CIR then at each step there need only be $M^3$ branch computations at each time step. This is a factor of $M^{L-3}$ improvement in computational complexity over the vanilla VA. Since there are effectively only three memory states (in our example) at each time step in the trellis which affect the output we note that the state definition will change at each trellis step. For instance, at one step the state may be defined by the data bits $x_5, x_8, x_9$ and the next step may require data bits $x_8, x_9, x_{10}$. If we decide on a traceback length of size $K$ then we will require $K$ trellis decoders - each of which will decode a different time step's bit. Consequently, our complete decoder will have $K$ trellis decoders running in parallel with the $k^{th}$ decoder decoding bits $x_{Kn+k}$.

SD algorithms represent a substantial departure from trellis decoders mentioned above as they operate on a portion of a trellis as opposed to the entire trellis. Since trellis decoders complexity grows exponentially, SD clearly offers a substantial decrease in complexity. Furthermore, sequential decoders are not required to operate on a trellis - the algorithm is simplified to a modest degree if it is assumed to operate on a tree. Both the fact that sequential decoders operate on trellis fragments and the fact that state merges are not considered when operating on a tree result in some performance loss in SD compared to decoding on a full trellis.

## 5.3 Sequential Decoding (SD)

As mentioned above, SD offers a very substantial complexity benefit with little loss in performance compared to decoding over the complete trellis (provided we operate below the computational cutoff rate). In this section we will explore the basic principles of SD and describe the three basic algorithmic types followed by a brief commentary on each. First, we will discuss some preliminary items common to all the methods to be discussed.

Since we will be limiting ourselves to discussions involving tree searching, we will define a couple of terms necessary for tree searches. These terms are correct subset (CSS) and incorrect subset (ISS). When traversing a tree, at each node we have several choices depending on the constellation size of our symbol set. There is, of course, only one correct choice for the path to proceed from this node. The subtree following the correct branch below this node is referred to as the CSS. All other subtrees following the other branches are then members of the ISS for this node.

Next, because each algorithm does not search the entire trellis, some criteria must be established as to the search boundaries. These boundaries are referred to as the stop and drop lines. Ideally, the purpose of the drop line is to stop the ISS paths before they can result in an error. Similarly, we would like to declare the correct branch to output by having the CSS cross the stop line at the earliest possible time. Therefore, when in the process of a search a drop line is crossed, the particular path is dropped from the list and does not "survive." The first path to cross the stop line decides the appropriate output branch.

Finally, each of the methods to be discussed have their own branch and path metrics. In the case of some algorithms, these metric calculations are identical

to the Viterbi metric calculations. This is particularly true in the case of the M and T-Algorithms which will be discussed shortly.

There are basically three ways in which SD algorithms can be classified: 1) Depth-First, 2) Metric-First, and 3) Breadth-First. The titles of each of these classifications imply the way in which the trellis is probed. Depth-First searches perform path metric calculations following the branch having the best branch metric from one node to the next as the search proceeds more deeply into the trellis, following a path of least immediate resistance. At each step in the depth-first algorithm the path metric is compared to a threshold. If the threshold is not triggered, a check is made to see how far the probing has proceeded into the trellis following the first tentative decision. If the required depth has been reached, then the tentative decision is output. If the drop line is triggered, on the other hand, the algorithm must backtrack to an earlier node and proceed along an alternate path. Depth-first algorithms have the advantage that they require the least processing under quiet channel conditions. However, if a burst of noise appears, the amount of processing quickly escalates due to extensive backtracking. The best known depth-first algorithm is the Fano algorithm. Futher details on the Fano algorithm are contained in [AM] and heuristics for efficient hardware implementation are provided in [Pot97].

The stack algorithm is an example of a trellis metric-first search. In this case the stack algorithm always extends the best path (as measured by the path metric) in storage. This means that the stack algorithm must always maintain a list of the best paths. As each best path is extended, it is necessary for the algorithm to perform a sort to determine how to proceed in selecting the best path for the next cycle. Furthermore, the algorithm drops paths that cross the drop threshold and, as in the depth-first search, if the stop line is reached the

first branch is output. Finally, the stack algorithm must obviously be limited by the stack size, so if this point is reached the worst path(s) are dropped to make room for better paths.

As examples of breadth-first searches we have the M and T algorithms. The M-algorithm gets its name from the fact that it always maintains precisely $M$ paths in storage. Because the M-algorithm is breadth-first, it extends all $M$ paths in storage resulting in $Mb$ extensions. Of these extended paths we drop any paths that hit the drop line. If any path hits the stop line we release the first branch of this path as output. Of the remaining paths we select the best $M$ paths and repeat the cycle.

The above algorithm can be simplified if we recognize that the algorithm by design must handle a maximum of $M$-paths. Such a modified algorithm would not need to compute the drop line and simply maintain the list of the best $M$-paths. Furthermore, rather than computing the stop line, a particular decision depth may be adopted for branch output decisions.

The T-algorithm can be considered an extension of the M-algorithm. The principal difference between the M and T-algorithms is that the T-algorithm only maintains the paths that are within a particular threshold, $T$, of the best path. Therefore, we need only extend such paths as survive subject to the constraint that no greater than $M$ paths may survive. Such an algorithm results in the minimum average effort [Sim90]. This is the algorithm that will be employed in our performance simulations later in this chapter.

Regardless of which trellis decoding method we use, our performance will still be bounded by that of the full trellis search. Usually such performance calculations involve the determination of $d_{min}$ or $d^2_{free}$ when either Hamming or Euclidean distance measures are appropriate, respectively. This is the subject of

our next section.

## 5.4 Performance of MLSE Under Realistic Channels

In this section we consider the performance of MLSE decoding under realistic ISI channels. Although these results may be generalized further we will limit our discussion to binary PAM.

Because MLSE decoding involves estimation of the most likely sequence of symbols to have produced the received stream, this involves determining the symbol sequence having the minimum distance to the received stream. There are two methods for performing the calculation of $d^2_{free}$ - the minimum squared Euclidean distance. The first method we term the direct method. This method simply involves convolving an allowed error sequence, $\epsilon$, with the channel, $f$ of length $L$, and finding the total energy in the result:

$$d^2(\epsilon) = \sum_{i=k}^{k+l-1} \left( \sum_{j=0}^{L} f_j \epsilon_{i-j} \right)^2 \tag{5.1}$$

This is the total squared Euclidean distance for this particular error sequence. If we consider all possible error sequences $\epsilon$ and find the minimum value for $d^2(\epsilon)$ we will then obtain $d^2_{free}$. In practice, we must place a restriction on the sequences we test, otherwise the list is infinite. A fairly straightforward heuristic suggests that the maximum length error sequence that should be tested is certainly no longer than the channel itself. Using this guideline we then proceed to consider all the error sequences having two errors of length $L^2$. Clearly, the direct method is computationally intensive. We can reduce the complexity somewhat if we realize that the lower values $d^2_{free}$ will be clustered in the region where there are a low

[2]In the context of Euclidean distance measures, sequences having only a single error of unit energy result in $d^2_{free}$ equal to the channel energy.

number of input errors. Consequently, in practical problems we will determine a cutoff for the number of errors to be considered. We will find this useful in simulations that we will be performing later.

The second method we consider is the weight enumerating function method. The weight enumerating function for a convolutional code expresses, in algebraic form, all of the possible error weights corresponding to the possible error sequences. This can be expressed:

$$T(W, I) = \sum_{e} I^{i_e} W^{w_e} \tag{5.2}$$

where we are summing over all possible error sequences which we label $e$ having $i_e$ input errors and a corresponding output error weight of $w_e$. As an example, consider the rate 1/2 convolutional encoder in Fig. 5.1[3].

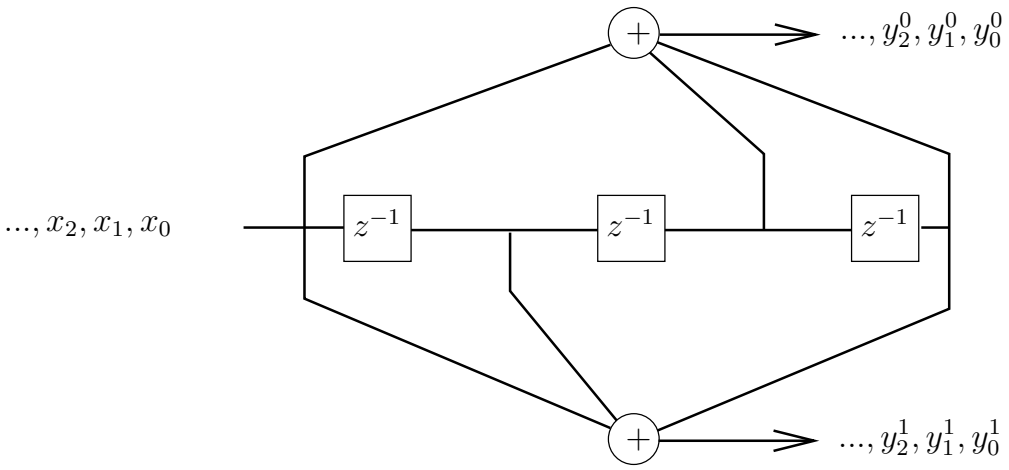


Figure 5.1: Example Convolutional Encoder

The encoder in Fig. 5.1 possesses eight states. The state transition diagram for this encoder is shown in Fig. 5.2. Each of the branches is labelled with the corresponding input error and output.

[3]Although this example involves Hamming weight instead of Euclidean distance, a similar

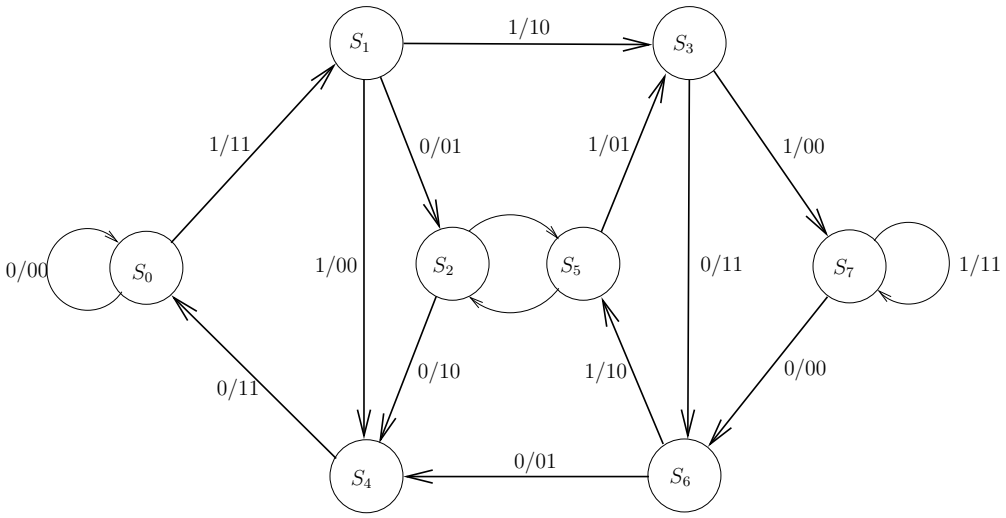


Figure 5.2: Example State Transition Diagram

The vectors between states are labelled with the number of input errors and output Hamming weight ($W^2I$ corresponds to an output weight of 2 and a single input error for this transition). In order to study the performance of this encoder we eliminate the all-zeros path (no errors path) by breaking the state transition diagram at the all-zeros loop which yields the directed Signal Flow Graph in Fig. 5.3.

From this diagram it is straightforward to obtain the state transition matrix corresponding to transitions among the non-zero states. This is done by assigning the columns of this matrix as the state-of-origin and the rows as the destination-state. The elements of this matrix are the vector labels of the Signal Flow Graph. The matrix is depicted in equation (5.3) below:

analysis holds with some modification that will be explained later.

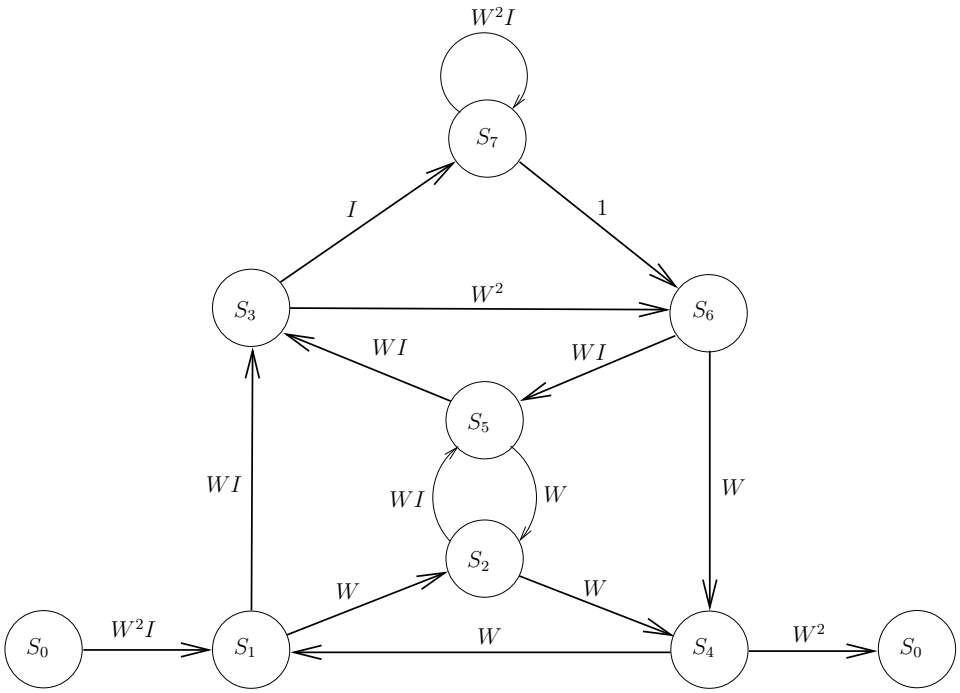


Figure 5.3: Example Signal Flow Graph

$$A = \begin{bmatrix} 0 & 0 & 0 & 0 & I & 0 & 0 \\ W & 0 & 0 & 0 & W & 0 & 0 \\ WI & 0 & 0 & 0 & WI & 0 & 0 \\ 0 & W & 0 & 0 & 0 & W & 0 \\ 0 & WI & 0 & 0 & 0 & WI & 0 \\ 0 & 0 & W^2 & 0 & 0 & 0 & 1 \\ 0 & 0 & I & 0 & 0 & 0 & W^2I \end{bmatrix} \tag{5.3}$$

In order to determine the algebraic equation which expresses the weight enumerating function, we need to define two more vectors. The first vector, $b$, is a column vector which contains one element expressing a single input error and the corresponding output error weight. The single input error corresponds to the transition between the zero state and state one. The second vector, $c$, is a row vector which expresses the output error weight corresponding to the transition

from the last state to the zero state. These vectors are given below

$$b = [\, W^2 I \quad 0 \quad 0 \quad 0 \quad 0 \quad 0 \quad 0 \,]^T \tag{5.4}$$

$$c = [\, 0 \quad 0 \quad 0 \quad W^2 \quad 0 \quad 0 \quad 0 \,] \tag{5.5}$$

To determine the total number of input errors and output weight for a particular path length through the trellis we utilize the previous matrices as follows. The expression corresponding to the shortest path through the trellis has a single input error and is simply given as: $cAb$. The next shortest path is: $cA^2b$, and so on, as we increment the exponent of the matrix $A$. In other words, transitions which don't exit the graph are represented by incrementing the exponent of the state transition matrix. The complete algebraic series which yields the weight enumerating function $T(W, I)$ is:

$$T(W, I) = \sum_{L=2}^{\infty} cA^{L-2}b \tag{5.6}$$

Finally, it is well known that if $|A| < 1$ then

$$T(W, I) = c(I - A)^{-1}b \tag{5.7}$$

We can make this assumption under the condition that $I = 1$ and $W < 1$.

Next, we desire to determine $d_{min}$ from the expression for $T(W, I)$. In this equation, the minimum distance is given by the least W-exponent. This can be done by inspection for very short constraint lengths, but we need another approach when constraint lengths get longer. In this case, we note that when $W < 1$ those terms with the least exponents will dominate the complete summation in equation (5.2) as well as equation (5.7). We also take $I = 1$ since this is irrelevant to determining $d_{min}$. Consequently, we may begin by taking the limit of $T(W, I)$

as $W \rightarrow 0$. Next, to obtain the $d_{min}$ we take the base-$W$ logarithm of the result. Equivalently, we may reverse the previous operations to obtain:

$$d_{min} = \lim_{W \rightarrow 0} \log_W(T(W,1)) \tag{5.8}$$

To accomplish this in practice is a delicate matter. This is because as $W \rightarrow 0$, it is clear that we may run into numerical problems in evaluating $(I - A)^{-1}$ since the elements having $W$ with large exponents evaluate so close to zero that we quickly run into round off problems.

But, for a fairly simple example such as we have given above, it should not be a problem. To this end, we have given the matrices above evaluated for $W = 10^{-5}, I = 1$. Using equation (5.8) we find $d_{min}$ to be 5.94. We know for this case that $d_{min}$ is 6.

In the preceding discussion we have focused on the determination of $d_{min}$ for a particular convolutional code. For our purposes, however, we are interested in MLSE equalization of ISI channels. Consequently we are concerned with determining $d^2_{free}$, which is based on the Euclidean distance, rather than $d_{min}$ which is based on Hamming distance. This introduces significant additional complexity in determining $d^2_{free}$. This is because a particular error sequence does not produce an unambiguous sequence of output weights. The ambiguity is created by the particular input sequence. Consequently, we must consider all possible input sequences for each possible error sequence in determining $d^2_{free}$. Doing this would result in an enormously complex signal flow graph (for binary PAM this would be $2^{2L}$ states). However, if the CIR contains fewer than L non-zero elements, say $M$, then a technique developed in [Wes99] may be applied to reduce the complexity to $2^{L+M}$ states. Notwithstanding such complexity reduction, long channel lengths result in significant complexity and we shall resort to determining $d^2_{free}$ by

restricting our search to error sequences of relatively few errors using the "brute force" method of equation (5.1).

The preceding discussion has provided us with a couple of tools for the determination of $d^2_{free}$ for particular channels. We will find this useful as we attempt to answer the following question that would be of concern to one relying on single carrier modulation using MLSE decoding: "What is the worst-case CIR of length $L$?" Such a question may influence our decision on whether diversity methods or some other alternate method should be employed to overcome such channel conditions.

This question is answered in [Pro95d] and provides some worst-case examples for relatively short channels. The procedure for accomplishing this is to, first, generate a possible error sequence. The autocorrelation of this error sequence, $R[n]$, is used to generate the matrix below (we use a length two error sequence and $L = 3$ CIR):

$$A = \begin{bmatrix} R[0] & R[1] & 0 \\ R[1] & R[0] & 0 \\ 0 & R[1] & R[0] \end{bmatrix} \tag{5.9}$$

We then perform the eigen-decomposition to find the eigenvalues and eigenvectors. The smallest eigenvalue is the minimum $d^2_{free}$ corresponding to this error sequence/channel pair and the corresponding eigenvector is the worst-case channel. Several examples are given in Table 1.1 [Pro95d].

As can be seen from these examples the potential loss due to such worst-case channels can be substantial. However, in light of this, another important question that should be posed is: "What is the likelihood of such extreme channels?" If we can show that the prevalence of such channels is sufficiently rare then it would not, in most practical applications, be appropriate to seriously consider these

worst-cases. Addressing this question is the subject of our next section.

## 5.5 Simulation of Channel Energy vs $dfree^2$ for Realistic Channels

To answer the question posed in the previous section we must give consideration to two areas that will affect the outcome. The first relates to how we can address the question of how significant the performance difference is between considering the total channel energy and MLSE processing. For this we will require some performance measure. The second area concerns the channel models that we intend to use. Clearly, MLSE processing depends not only on the total channel energy but also the distribution of the channel impulses. Therefore, it would be advisable to select the appropriate channel model for the expected environment.

Our answer to the first question is straightforward: $d^2_{free}$ provides a measure for estimating performance loss in MLSE equalization. For this we will generate error sequences having a limited number of errors greater than one and processes them as in equation (5.1). For example, we will need to generate all the possible error-sequence permutations of some prescribed length having two errors. Similarly, for three errors, four, five, and so forth. After processing this collection of sequences through a given channel we select the minimum $d^2_{free}$ and collect this sample. We also collect the total channel energy in a separate bin. We then generate another random channel realization using our channel model and repeat the experiment and collect our second sample, and so forth. After having done this many times we are then in a position to generate a sample density or distribution of channel energy as compared to $d^2_{free}$. If the two are "close" to one another, we may then conclude that the worst-case channel issue is, indeed, insignificant.

As to the question of the particular channel model to use, we are faced with a more challenging question. This is because the research to date (as well as in this thesis), has only provided the CIR and inter-arrival time distributions as distinct entities. They have not been integrated into a single model that would provide both simultaneously. So, in the simulations we perform in this paper we will be relying on two models for generating the CIR profiles. The first model, which we will refer to as the "conventional" model, is generated by choosing exponential interarrival times and selecting the path loss corresponding to an appropriate path loss exponent. To this path loss we add the shadowing gain/loss to each arrival (in dB). Finally, the combined path loss plus shadowing loss is used as the standard deviation to select a Rayleigh random variable. By using these two models we will show the insensitivity of the final conclusion to the selection of model.

The second model, which we refer to as our "integrated" model, is generated by choosing interarrivals so that the logarithms of these interarrivals have an exponential distribution and selecting the path loss corresponding to an appropriate path loss exponent. By this modification to the generation of interarrival times we can achieve the uniform distribution in power that was postulated in our development of the Uniform-dB-Suzuki distribution. This choice of interarrival process has the effect of increasing the time separation for impulses as we progress later in the profile. The justification for this is that since, in practice, the sensitivity of our receivers have a finite limit (with respect to some noise floor) it would therefore stand to reason that the arrivals would appear to become less frequent as we progress later in the profile. This interarrival profile can be generated by taking the current arrival time and using it as the interarrival time for the next arrival.

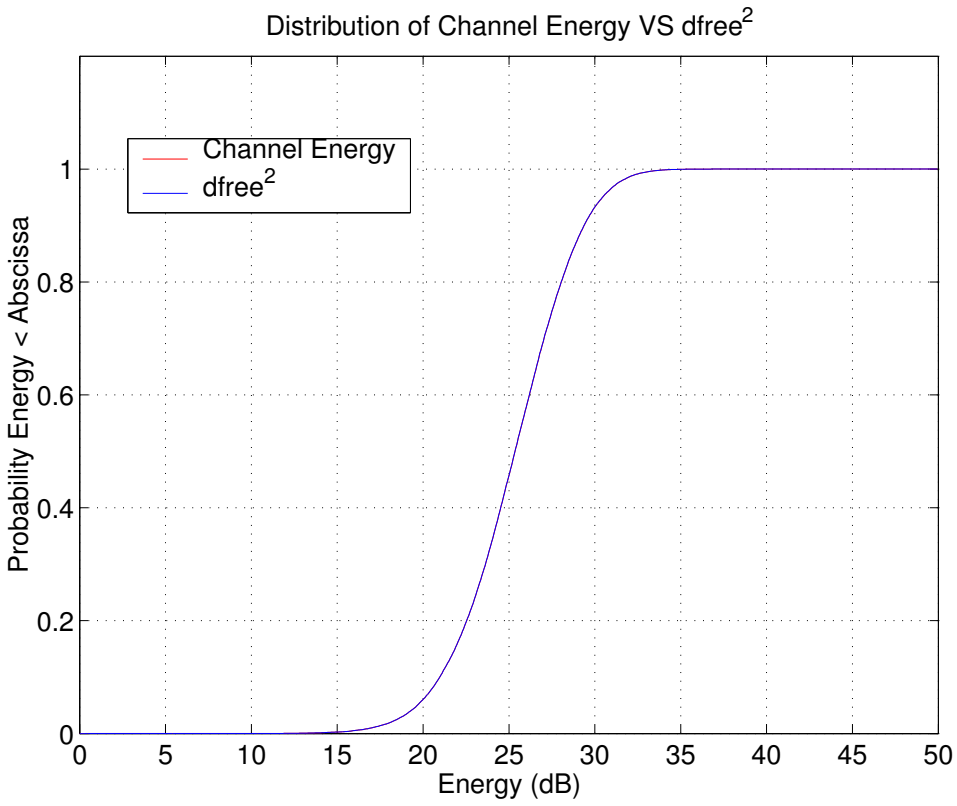


Figure 5.4: Conventional Interarrivals

The results from the "conventional" and "integrated" channel models are presented in Figs. 5.4 and 5.5 respectively. These figures represent the probability of non-exceedance similar to those presented in Chapter 4. In each graph it appears that the channel energy directly overlays the $d^2_{free}$. This is, however, not precisely the case. Figs. 5.6 and 5.7 present the differences between the channel energy and $d^2_{free}$ distributions for both channel models. It is clear that the "integrated" model does result in a larger difference between the total channel energy and $d^2_{free}$, but this difference practically undetectable in Fig. 5.5. Consequently, we may safely conclude that the performance degradation due to the possible occurrence of worst-case channels is not significant.

The results we have presented so far assume a non-normalized channel con-

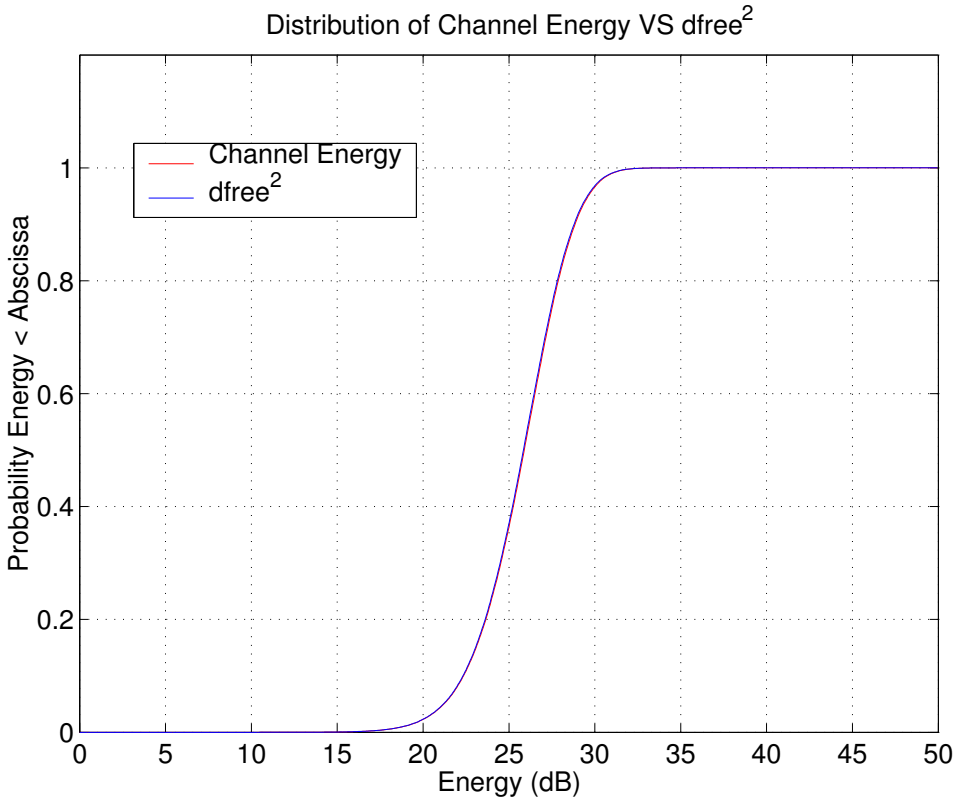


Figure 5.5: "Integrated" Model

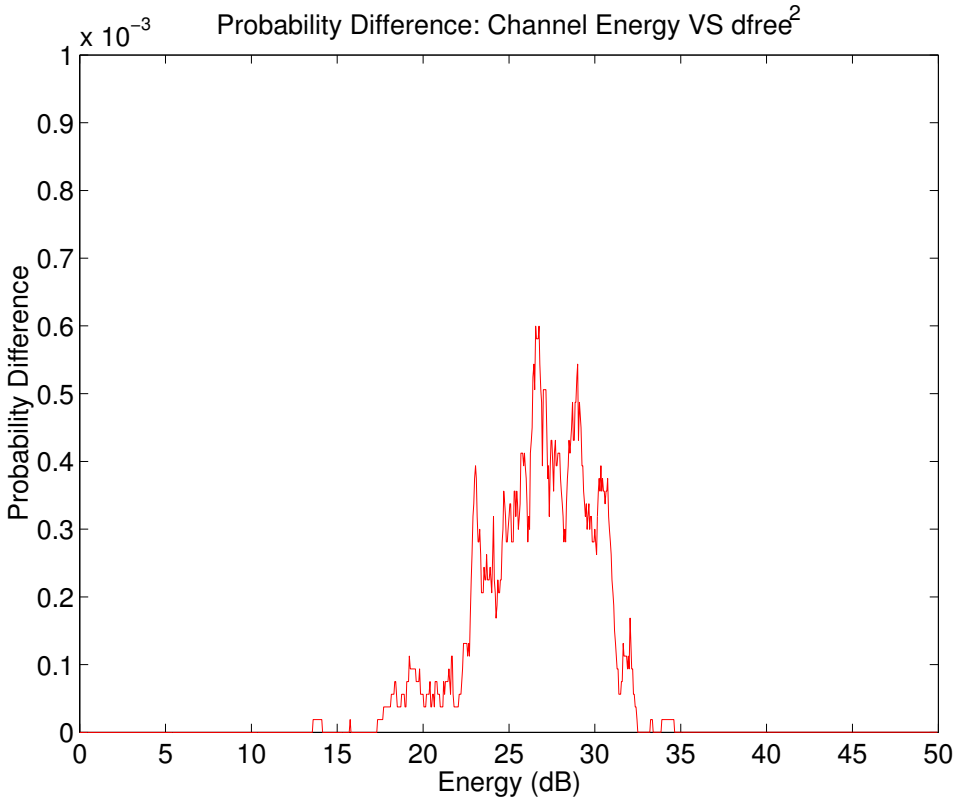


Figure 5.6: Conventional Interarrivals

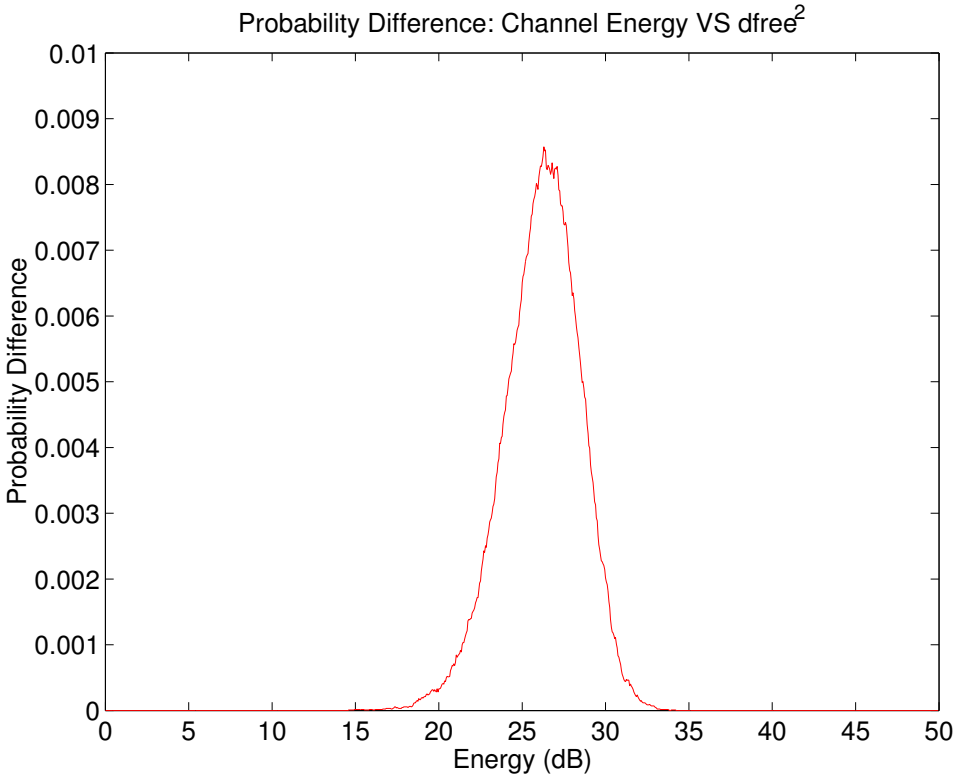


Figure 5.7: "Integrated" Model

dition - i.e. a constant transmitter power. If we, on the other hand, assume normalized channel conditions then we can compare all channel realizations on an equal footing with respect to total channel energy. So, as another performance measure, we would like to determine the density of normalized $d^2_{free}$ which we define as the ratio of $d^2_{free}$ to total channel energy. This result is displayed in Fig. 5.8. A couple of facts regarding this figure to note are that, first, only the non-zero ratio is displayed and, second, that we have normalized the density. Prior to normalization, the percentage of realizations with zero loss was about 93 percent or seven percent "lossy." In Fig. 5.8 we can see that the vast majority of channel realizations have $d^2_{free}$ falling within a loss range of roughly 2 dB of total channel energy. As a consequence, we would not expect significant performance degradation to occur in MLSE decoding due to existence of these "lossy" channels.

## 5.6 T-Algorithm Performance Under Realistic Channel Models

Having demonstrated that the "integrated" channel model results in greater loss, we now turn our attention to actually simulating the error rate performance of the T-algorithm to the channels described in the previous section. Using the "integrated" channel model, we generated channel realizations having 100 taps assuming a path loss exponent of three and that the line-of-sight (LOS) delay between the transmitter and receiver was 32 taps. These assumptions result in about 20 dB average path loss over the complete CIR. As we mentioned before, the logarithms of the interarrivals in this model have an exponential distribution.

For this simulation, we chose a 4-QAM constellation. Since we have 100 taps,

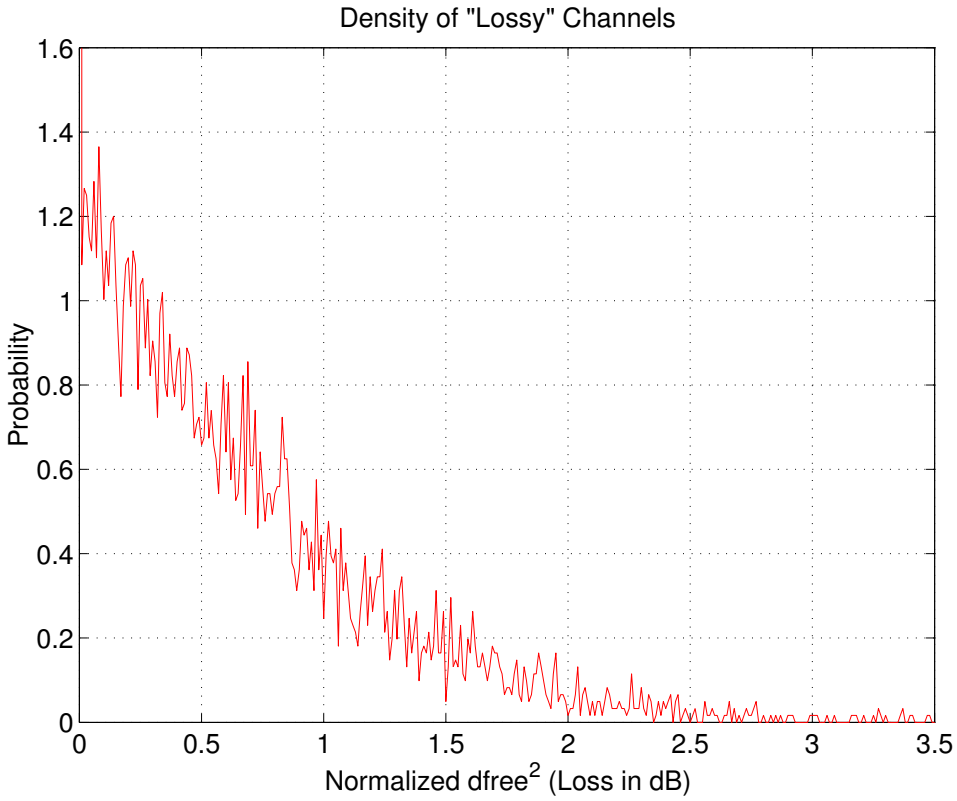


Figure 5.8: Density of Lossy Channels

a full Viterbi implementation would require $4^{100} \approx 10^{60}$ states. Using the T-algorithm, we limited the maximum number of surviving paths to 1024 with no attempts to check for trellis merges - i.e. a pure tree search.

In our simulation, we randomly selected normalized channels from our previous simulations - 200 in all. Some of these channels had normalized $d^2_{free} < 1$ - about seven percent as mentioned earlier. We then ran a simulation over a range of SNR's for all channel realizations and averaged the error rates respectively. The graph of this simulation is shown in Fig. 5.9. In this graph we have compared the T-Algorithm performance with the uncoded bit-by-bit decoding performance of a non-dispersive channel. It is interesting to note that we appear to obtain convergence as the SNR increases. This occurs because at lower SNR's, error events having more bit errors are almost as likely as those having less. This is why, in order to determine $d^2_{free}$ we allowed $W \rightarrow 0$ which is equivalent to $SNR \rightarrow \infty$.

## 5.7 Conclusion

In this chapter we have described a number of equalization methods for single carrier systems and provided a system of classification for such. From this list of methods we have identified MLSE methods as "optimal" with respect to the fact that they show the least loss compared to harnessing all the energy within a given channel. We noted however, that application of Viterbi decoding is generally prohibitively expensive in terms of decoder complexity for typical CIR lengths. The sequential decoder, and T-algorithm in particular, offers a substantially more compact alternative. We then noted that the only remaining problem area was the fact that for a given impulse response length that worst-case channel conditions could significantly impair performance of MLSE decoding. The per-

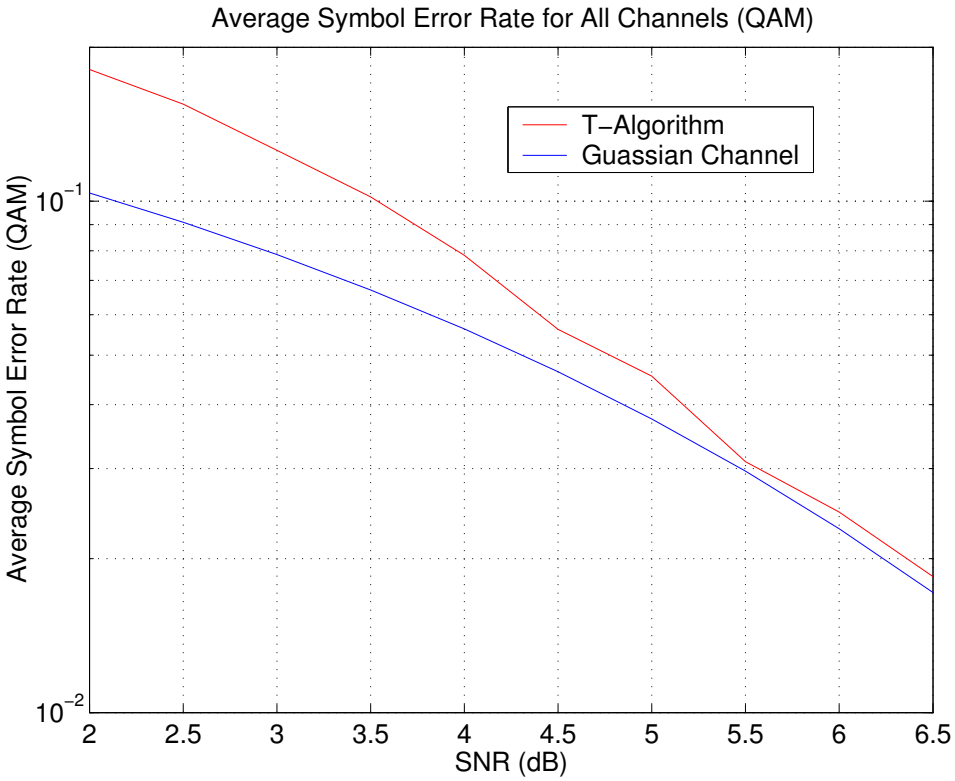


Figure 5.9: T-Algorithm Performance

formance proxy we utilized was $d^2_{free}$ and presented two computational methods. We addressed this question by simulation using two different CIR generators and showed that for each the distribution of total channel energy is substantially the same as the distribution of $d^2_{free}$ with the final conclusion that virtually all the channel energy may be recovered assuming accurate channel estimates are available. We concluded with a simulation of the T-algorithm's performance showing convergence to the performance obtainable under flat channel conditions with equal energy as SNR increases.

# CHAPTER 6

# A Realistic Channel Shadowing Model

## 6.1 Introduction

Knowledge of the long term fading due to path loss and shadowing are required in the analysis of wireless performance. In previous work [Ail02] a shadowing model was developed for the ground to ground (GtG) communication scenario including shadowing effects. The cited work assigns a set of values independently chosen from a Gaussian distribution to a two-dimensional array of grid points. These grid points are assumed to be have a uniform two-dimensional spacing of $d$ meters. These values represent the shadowing variations in dB. A user antenna located within a set of four grid points is assigned a fading value by interpolation of the surrounding four points. This is done for both antennas and the two values are combined to yield the total shadow fading value. The mean path loss is determined in the standard way with some value selected for the path loss exponent appropriate to the wireless environment.

The model proposed herein was inspired by the previously cited work. In the present work, we intend to provide modifications that account for users which may be airborne while preserving the feature of the cited work that a return to the occupancy of a prior pair of antenna coordinates results in the same long term fading loss. The latter feature is achieved by randomly choosing a "terrain." From any point in this terrain, the local skyline determines the local shadowing

of each antenna. Consequently, a feature of this terrain model is that shadowing is correlated with the azimuth of the arriving signal. We note that this model converges in its effect to the plane-earth path loss model for GtG scenarios with antennas of sufficiently low altitude (without obstructions) and to a free-space model when both antennas a substantially above the mean obstruction height (e.g. Air-to-Air (AtA) scenarios). We also present a number plots demonstrating the model and also compare it to measurements taken from an actual survey.

## 6.2 Path Loss Model

To predict the performance of a wireless communications system it is necessary to make some estimate of the signal power loss between the receiver and transmitter. There are basically four components to this loss:

- The path loss component expresses the loss as a function of range between the two antennas;
- The shadowing component describes the gain/loss incurred due to obstacle shadowing/waveguiding of the signal;
- The multipath gain/loss arises when multiple rays arrive from significantly different paths resulting in self-interference which may either boost or attenuate the received power;
- A loss associated with the receiver/transmitter electronics performance characteristics.

We will restrict the discussion in this chapter to the long-term loss components: Path loss, and shadow loss. There are basically two models for the path loss. One is the free-space Friis model which has the power decreasing as the $2^{nd}$ power of increasing range. The other is the 2-ray plane-Earth model. The latter

model has the power decreasing as the $4^{th}$ power of increasing range.

Since there is such a substantial difference in the predictions each makes, it is essential to recognize the appropriate applications for each. The free-space model should be used, as the name implies, for cases when the ground is a long way from the antennas as compared to the range between them. The 2-ray model, on the other hand, should be used if range between the antennas is much larger than height of either antenna. How to transition between these two models is the subject of this section.

In order to develop a model that accommodates the variation between the free-space and plane-Earth models we will start with the plane-Earth model and examine each step in the derivation. It will be observed that as the altitude of one antenna dominates, as in the AtG case for example, that the new model converges to the free-space model. As both antennas approach the ground, the model will converge to the plane-Earth model.

The basic reasoning in the development of the 2-ray plane-Earth model is that the direct ray and reflected ray are expected to combine in a *destructive* way resulting in substantial attenuation of the received signal. This occurs because 1) the reflected ray incurs a phase-inversion due to the reflection, and 2) the path differences between the direct and reflected ray are sufficiently small so that both rays are received *almost* out-of-phase. Because the grazing angle for this model is assumed to be small, a small-angle approximation gives us the characteristic $4^{th}$ power loss expression. The detailed derivation follows.

Let $h_t$, $h_r$, and $d$ denote the transmitter and receiver antenna heights and geographical-distance between ground-projections of both antennas respectively. The path difference $\Delta$ between the LOS and reflected rays is:

$$\Delta = d^{''} - d^{'} = \sqrt{(h_t + h_r)^2 + d^2} - \sqrt{(h_t - h_r)^2 + d^2} \tag{6.1}$$

If we assume that $h_t >> h_r$ and $d >> h_r$ and define $r \equiv \sqrt{h_t^2 + d^2}$ then,

$$\Delta \approx \frac{2h_t h_r}{r} \tag{6.2}$$

In [Yac93] it is shown that the received power is (with a slight modification):

$$P_r \approx P_t G_t G_r \left(\frac{\lambda}{4\pi r}\right)^2 \left|1 + \rho e^{j\theta_\Delta}\right|^2 \tag{6.3}$$

when both paths are of similar length, where $\rho$ is the reflection coefficient and where $\theta_\Delta$ is the phase difference of the reflected ray with respect to the direct ray which is:

$$\theta_\Delta \approx \frac{4\pi h_t h_r}{\lambda r} \tag{6.4}$$

We can also obtain the following simplification:

$$\left|1 + \rho e^{j\theta_\Delta}\right|^2 = (1+\rho)^2 - 4\rho sin^2\left(\frac{\theta_\Delta}{2}\right) \tag{6.5}$$

giving, after substitution:

$$P_r \approx P_t G_t G_r \left(\frac{\lambda}{4\pi r}\right)^2 \left((1+\rho)^2 - 4\rho sin^2\left(\frac{\theta_\Delta}{2}\right)\right) \tag{6.6}$$

The reflection coefficient $\rho$ can be expressed as [Rap96]:

$$\rho = e^{-8\left(\frac{\pi\sigma_h sin\theta_i}{\lambda}\right)^2} I_0\left(8\left(\frac{\pi\sigma_h sin\theta_i}{\lambda}\right)^2\right) \tag{6.7}$$

where $\theta_i$ is the angle of incidence with respect to the plane of reflection, $\sigma_h$ is the surface "roughness" in meters, and $I_0$ is the Bessel function of the first kind and zero order.

Note that the reflection coefficient approaches $-1$ for frequencies above 100 MHz and grazing angles less than 10 degrees. If we assume perfect reflection and a small grazing angle, we have:

$$P_r \approx P_t G_t G_r \left(\frac{h_t h_r}{r^2}\right)^2 \tag{6.8}$$

which is the standard form for the plane-Earth model. Assuming perfect reflection only, we have:

$$P_r \approx P_t G_t G_r \left[ \frac{\lambda}{2\pi r} sin \left( \frac{2\pi h_t h_r}{\lambda r} \right) \right]^2 \tag{6.9}$$

We note that the above expressions only apply when the heights of both antennas are high enough above ground to presume that a reflection exists. The previous two expressions approach zero gain as the antenna heights approach zero.

## 6.3 Shadowing Losses

As mentioned in the introduction, the shadowing model describes the loss incurred due to obstacles shadowing the signal. Since the shadowing "loss" is often described in terms of a log-normal distribution (zero-mean variate), it *might* be inferred that the model does not purely describe attenuation due to actual shadowing. In other words, this might imply that there exist both gain and attenuation effects. As an example of a gain effect, in situations where the signal may be confined, as in a narrow valley or "urban canyon", this confinement tends to decrease the rate at which the power-density of the wave is decreasing. In effect, such confining acts as a wave guide serving to convey more signal power to the receiver than if the signal were allowed to expand in free space. This effect is analogous to creating circular waves in a pond and comparing this to plane waves of the same power created in a channel. At a distance from the source, the channelled-wave power density (defined as wave height squared per unit length of wave face) will have realized less loss than the power density of the circular wave expanding in the pond. In fact, if it were not for friction, the channelled wave would experience no loss. Hence, our "shadowing" distribution should reflect both the "gain" associated with channelling effects and "loss" associated with actual shadowing. However, as we shall later see, the lognormal distribution is

usually used to describe the variations about the mean path loss (described in the previous section) in spite of the fact that the net shadowing loss at some T-R separation is generally *not* zero mean but positive (in dB).

The fundamental mechanism describing actual shadowing loss is the "knife-edge diffraction" model [Rap96]. Diffraction of RF waves around an obstruction can be explained using Huygen's Principle which states that every point along a wave acts as a point-source for a secondary wavelet. The secondary wavelets combine to produce a new wavefront. The amplitude of the wave behind an obstruction will depend both on how deep into the shadowed region the antenna is and how close to the obstruction the antenna is. The commonly accepted knife-edge diffraction gain model is:

$$F(v) = \frac{1+j}{2} \int_v^\infty e^{-(j\pi t^2)/2} dt \tag{6.10}$$

where $v$ is the Fresnel-Kirchhoff parameter given by:

$$v = h\sqrt{\frac{2(d_1+d_2)}{\lambda d_1 d_2}} \tag{6.11}$$

and $h$ is the effective height of the obstruction above a line connecting the two antennas and $d_1$ and $d_2$ are the effective distances from the obstruction.

In order to avoid numerical integration of equation (6.10), we use a simplified approximation for the simulation:

$$F(v) = \quad 1, \qquad v \leq -0.5 \tag{6.12}$$

$$F(v) = \quad 0.5 - 0.62v, \qquad -0.5 < v \leq 0 \tag{6.13}$$

$$F(v) = \quad 0.5e^{-0.95v}, \qquad 0 < v \leq 1 \tag{6.14}$$

$$F(v) = \quad 0.4 - \sqrt{0.1184 - (0.38 - 0.1v)^2}, \qquad 1 < v \leq 2.4 \tag{6.15}$$

$$F(v) = \quad \frac{0.225}{v}, \qquad 2.4 < v \tag{6.16}$$

The diffraction gain in dB is:

$$G_d = 10log_{10}|F(v)| \tag{6.17}$$

The preceding discussion, so far, has addressed basic single-obstruction diffraction. What happens in the case of multiple obstructions? In such cases, obtaining exact solutions is generally impractical for most modelling purposes. So, to address the question of multiple obstruction diffraction, a number of approximating models have been developed [Yac93]. The Epstein-Peterson model calculates the shadowing loss by considering the knife edges local to each of the respective antennas. It then calculates the diffraction loss using equation (6.12) between antenna 1 and the second obstruction peak and the loss between antenna 2 and the first obstruction peak. The sum of the two loss factors is the total shadowing loss for the model. It is a simple model and is reasonable when the two antennas have significant geographic separation and are subject to local obstructions. Such a model would probably work well for many urban and suburban environments. The model degrades when the obstructions are close together or one antenna is not subject to local shadowing. In such cases a single knife edge would be more accurate.

As a consequence of the diffraction and wave-guide effects previously cited, the following abstraction is often used. If we consider a radio wave propagating from the transmitter to receiver we can suppose that it will encounter a number of obstructions along its path ("obstructions" in an abstract sense - i.e. we also consider wave-guides as "obstructions"). Each of these obstacles can be associated with an attenuation $\alpha_i$ (or gain). Expressed in dB the total loss has the form:

$$x = \sum_{i=1}^{n} \alpha_i \tag{6.18}$$

If the number of obstacles is large, then the distribution of the sum of these attenuation factors (in dB) can be approximated as normal. Thus, in addition to the range-dependent path loss derived in the previous section, an additional random factor known as "excess path loss" due to shadowing (etc.) is included in the total path loss expression.

There are a number of comments we should make about this "excess path loss." First, the total loss $x$ above is strongly correlated with T-R separation (provided the $\alpha_i$ are not zero mean). That is, we expect more obstacles between the antennas when their separation is large than in the case where the separation is less. The variance of $x$ is also correlated with T-R separation as well. Thus, we expect the shadowing loss to be range-dependent.

Second, we should bear in mind that the lognormal distribution was arrived at due to a couple of assumptions which are required by the Central Limit Theorem which are: identical distribution of each element, and a large number of elements. These assumptions may not be reasonable. In particular, if we consider a large T-R separation and assume a large number of obstacles, then as we traverse the signal path away from each antenna we expect that the attenuation factors to, in the mean, decrease as we approach the mid-point of the path. The reason for this is that, if we assume obstructions of similar height along the signal path, then the signal that is diffracted around the initial obstructions will "find" that subsequent obstructed points along the path are shadowed to a lesser degree as measured by the angular displacement from the direct path as compared to the initial obstruction. Thus we can conclude that the assumption of an identical distribution may not be particularly valid. Thus it is probable that the nearby obstacles (w.r.t. each antenna) will exert a greater influence over the total loss than those obstacles that are closer to the path mid-point. Consequently we might

expect that the total path loss and its variance to be dominated by a fairly small number of obstacles (near the signal path end-points) and further conclude that the total shadowing loss and its variance will approach some maximum values for ever-increasing T-R separation.

The previous commentary is given because the approach to modelling long-term fading frequently treats shadowing losses as zero-mean (in dB). But, as it is argued above, this is really not the case. What is frequently done in practice for deriving long-term fading models is to perform power loss measurements at various ranges and along various T-R paths. The measurements of range versus power are plotted on a log-log graph and a linear fit is produced. The mean path loss exponent is derived from the slope of the curve and the variance is taken to be the shadowing variations about the mean. In reality, because shadowing effects are range-correlated, they are difficult to separate from the nominal path loss in the linear curve fit.

Therefore, in practice, long-term loss models choose a path loss exponent consistent with the type of environment as well as a shadowing variance. In actuality, the path loss exponent models both the path loss plus the mean shadowing loss while the shadowing variance simply indicates the variation about the mean.

### 6.3.1 A Realistic Path Loss and Shadowing Loss Model

There are a number of important observations we can make in regard to preparing to arrive at a reasonable path loss and shadowing simulation model. We note that we may not be able to satisfy all of the below observations in the final model due to the need for a practical model.

1) Shadowing is path dependent. Thus, in a simulation, shadowing could be described by pairs of the antenna coordinates corresponding to the transmit and

receive antenna locations.

2) Shadowing tends to be a local phenomena. In other words, the shadowing effects tend to be dominated by the nearby obstacles with respect to each antenna. We draw this from the earlier argument that obstacles near the mid-point tend to not affect the total shadowing as much as those near the end-points of the path. Thus, in a shadowing simulation, the total shadowing could reasonably be derived independently for each antenna location and combined. This means that we do not necessarily need to describe shadowing in terms of coordinate pairs. This is a fortunate result in that it reduces the amount of storage required for shadowing factors by a couple orders of magnitude.

3) Shadowing is reduced with increasing antenna altitude. Increasing antenna height reduces the shadow intensity. Once an antenna is significantly above its local surroundings, the local shadowing effects should approach zero loss.

4) Far shadowing is reduced with increasing antenna altitude. Far shadowing is the shadowing intensity induced at the receiver antenna by the transmitter antenna's altitude (and vice-versa). In other words, as the transmitter's altitude is increased the receiver (even though it is stationary) will experience reduced shadowing intensity.

5) Assuming observation 2) above, the local shadowing tends to be correlated in azimuth angle. That is, an obstruction at one azimuth angle tends to largely be the same, in effect, at a slightly different azimuth angle.

6) Because the mean path loss incorporates some shadowing component, the path loss exponent should approach two as the antenna height increases above the surroundings local to both antennas. But, although the path loss exponent approaches two, there will still be some far shadowing effect. This can be modelled using knife-edge diffraction. So, for one antenna at fairly high altitude the total

loss will be free-space path loss plus a fixed loss due to diffraction.

The model proposed herein was inspired by the previously cited work [Ail02]. In the present work, we intend to provide modifications that account for users which may be airborne while preserving the feature of the cited work that a return to the occupancy of a prior pair of antenna coordinates results in the same long term fading loss. The latter feature is achieved by randomly choosing a "terrain." From any point in this terrain, the local skyline determines the local shadowing of each antenna. Consequently, a feature of this terrain model is that shadowing is correlated with the azimuth of the arriving signal. We note that this model converges in its effect to the plane-earth path loss model for GtG scenarios with antennas of sufficiently low altitude (without obstructions) and to a free-space model when both antennas are substantially above the mean obstruction height (e.g. AtA scenarios). We also present a number plots demonstrating the model and also compare it to measurements taken from an actual survey.

The present model is essentially composed of three parts: a path loss model, a shadowing model, and a "terrain" model which is required by the shadowing model. The path loss model used is given in equation (6.6). The shadowing model is based on the Epstein-Peterson multiple-obstruction diffraction model discussed earlier or the single-knife edge model as appropriate. The third component, the terrain model, has not been discussed in detail and will be presently.

The terrain model describes the height of the local obstructions surrounding each antenna at some presumed distance away from each antenna. The use of the Epstein-Peterson shadowing model is predicated on having two obstructions which form the local horizon for the transmit and receive antenna respectively. There are at least two ways the terrain could be described in a way that is compatible with the Epstein-Peterson shadowing model. One method would

be to first identify a geographical area for which the shadowing model would operate. Then, for each point in the area, identify the three dimensional (3D) locations of the points that represent the local horizon to the specific vantage point identified. These points would encompass each vantage point. The input to this method would be a topographical map. Note that all points within the area are considered "vantage points."

The second approach, which is utilized in the present simulation, identifies a set of points (obstruction locations) which *encircle* each vantage point. In this case each obstruction location is assumed to be displaced a distance $d$ from each vantage point. The question remains as to how to generate this set of points in such a way that the set of points are correlated over distance and angle. The following describes this process.

We first choose an area size, grid resolution, and azimuth angular resolution. In our simulation we chose 10 km as the square area dimensions, 1 meter as the grid resolution, and 360/16=22.5 degrees as the angular resolution. We also choose the mean obstruction height and two low-pass filtering functions. One filter describes the correlation over distance and the other describes the correlation over azimuthal angle. We then generate two 10000x16 arrays of independent zero mean unit variance normal random variables and add the mean obstruction height. We then put each of the 16 vectors of 10000 random elements through a low-pass filter which provides the desired topographical correlation over distance. We now have two 10000x16 arrays of filtered random data which we call the $X$ and $Y$ arrays. These arrays are created once at the beginning of the simulation. We finally determine the FFT of the impulse response of the azimuthal filter which we call $H$. The next step occurs for each pair of occupied antenna coordinates.

For a given antenna coordinate, we truncate to the nearest integer meter for the horizontal coordinates and use these to index the $X$ and $Y$ arrays. This yields a set of 16 points from the $X$ and $Y$ arrays each. We note that this gives us a unique "description" for every point in the grid. We then add the two sets of 16 points and perform the FFT on the result. By performing the element-by-element product of this with the $H$ vector we are, in effect, performing the cyclic convolution of the azimuthal filter with the $X + Y$ data set. The inverse FFT gives us this result. From this set of points we select the one element whose index points most closely to the opposite antenna. This element is the height of the local obstruction. As a result of this process we will obtain azimuthal and distance topographical correlation. A possible area of further contribution would be to investigate the availability of other models for generating this kind of topographical model.

We note that this long-term fading model is based on theoretically derived path loss and diffraction models. At the present time no model is included to model the wave-guide effects that can occur in urban environments. As such, in this model we will not observe signal loss less than the nominal path loss value.

### 6.3.2 Simulation Results

In this section the performance of the model is presented. The items we intend to demonstrate are enumerated below:

1) Comparison of the present model to data collected from a live survey.

2) Alter key parameters used in 1) to show the model's response to parameter variation.

3) Demonstrate "periodic" shadowing using a circular trajectory for one airborne antenna and one stationary antenna.

4) Demonstrate the positional and azimuthal-correlation of obstruction height.

For item 1) above we refer the reader to compare with [Rap96], Figure 11. This figure is a scatter-plot of path-loss versus horizontal displacement for measurements collected at four different German cities. The parameters used were: Carrier frequency=900 MHz, height of base=40m, height of mobile=2m, mean obstruction height=30m. Figure 6.1 shows the output of the model for these parameters. One striking feature of this scatter plot is that there appears to be a lower-bound on the long-term path loss. This is due to the fact that when there is virtually no shadowing, the model still imposes a base path loss. This feature would not be as apparent if we included a model to account for wave-guide effects. Aside from this, the model appears to fairly model the long term path loss data presented in [Rap96], Figure 11.

For item 2) we show the effect of raising the altitude of the higher of the two antennas to 300m in Figure 6.2. In Figure 6.2 we note that in the range of 100m to 250m that there almost no shadowing loss. This is because the 300m altitude of the airborne antenna eliminates shadowing while it is close to the ground antenna. As the airborne antenna moves downrange, the shadowing becomes much more pronounced. Another feature worth mentioning is that the abscissa corresponds to the distance between the projections of the two antenna positions on the horizontal plane.

In Figure 6.3 we see only occasional shadowing and what appears to be, otherwise, free-space path loss. The underlying path loss would eventually become 4th power if we were to extend the abscissa sufficiently.

For item 3) we have a ground antenna at the coordinates `[5000m 5000m 2m]` and an airborne antenna in a circular trajectory centered at `[7000m 5000m 300m]` with a radius of 2000m moving at a speed of 10m/sample. In this case we have

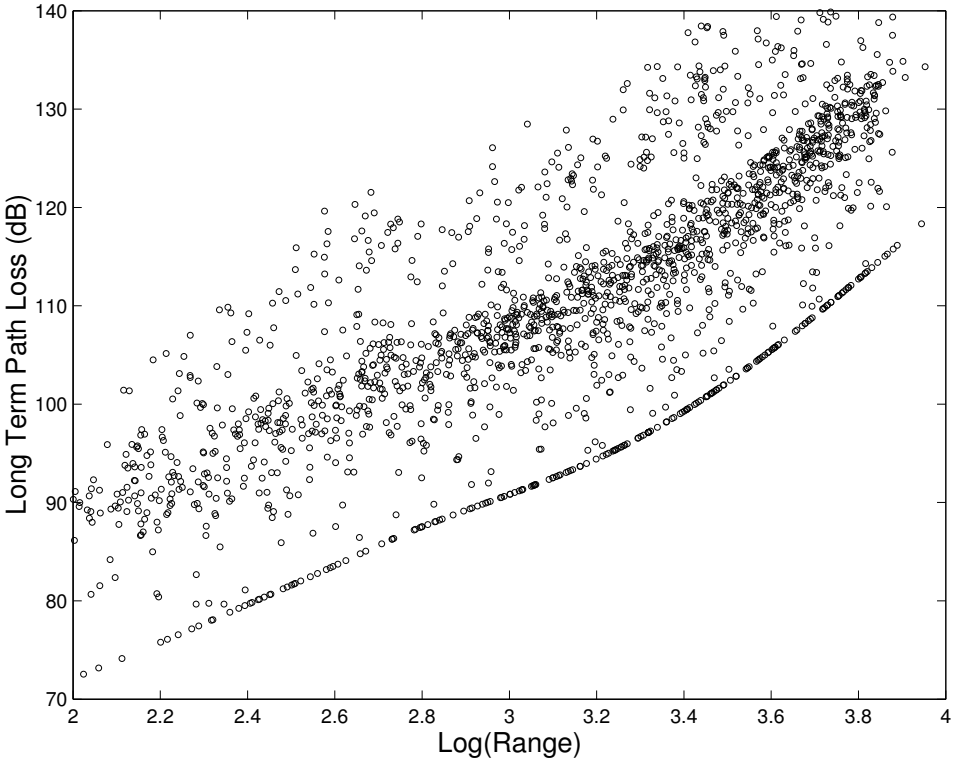


Figure 6.1: Scatter-Plot Corresponding to Item 2.

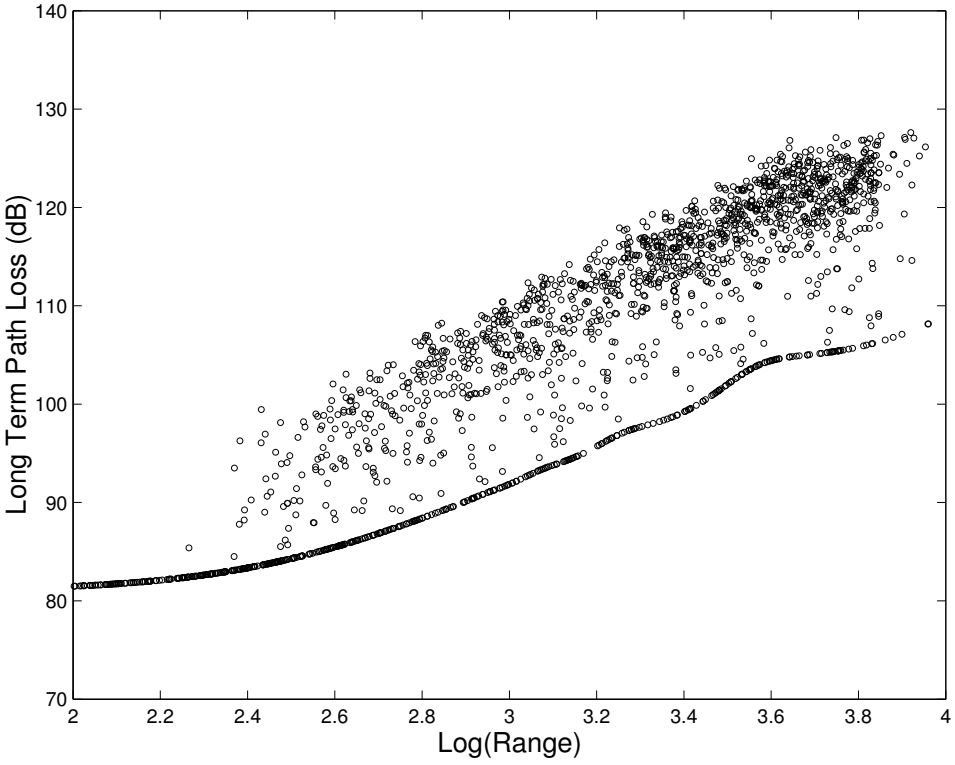


Figure 6.2: Scatter-Plot Corresponding to Item 2.

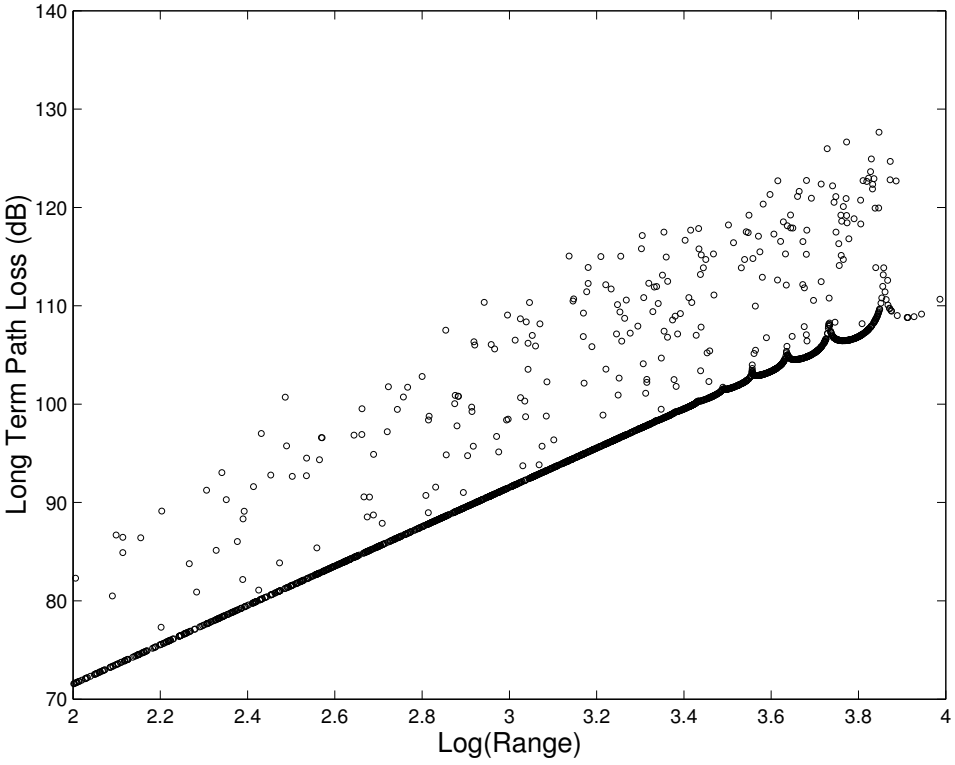


Figure 6.3: Scatter-Plot Corresponding to Item 2.

performed two complete circles in-flight. The minima occur when the aircraft is directly overhead the ground-based antenna. This is clearly apparent in the repeating path-loss pattern shown in Figure 6.4.

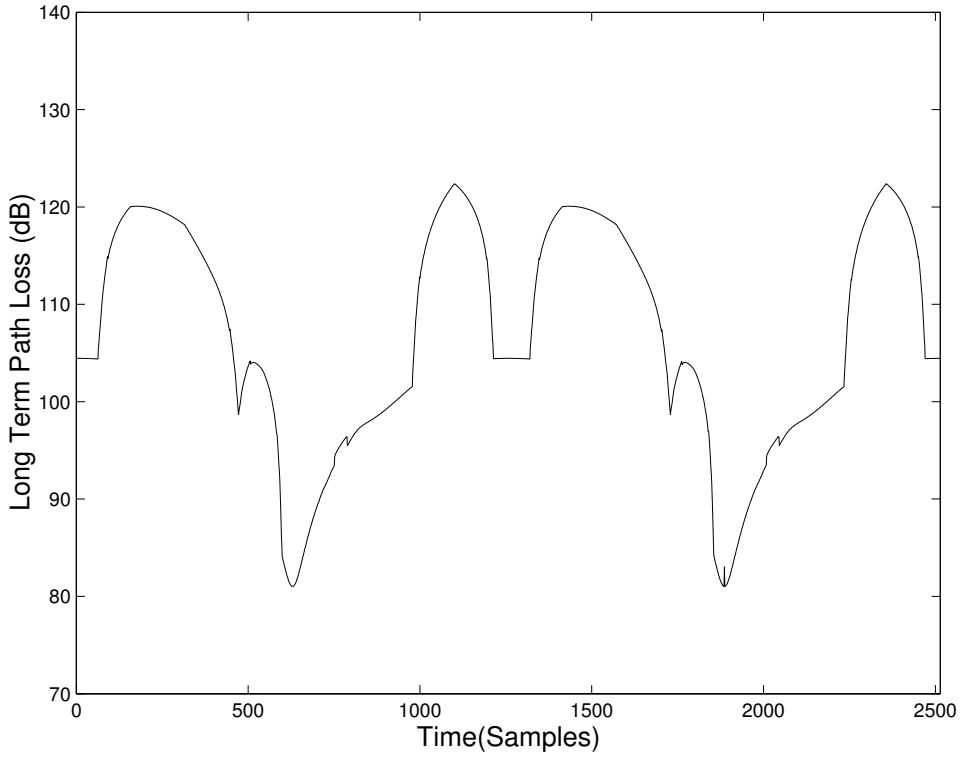


Figure 6.4: Circular Trajectory Corresponding to Item 3.

For item 4) we checked the translational and azimuthal autocorrelations. This was done by taking sample shadowing profiles at random locations in the grid. The sample autocorrelation was calculated and averaged over all realizations. The results are shown in Figures 6.5 and 6.6.

## 6.4 Conclusion

In this chapter we have developed a combined path loss and shadowing model. For the path loss model we derived from first principles the path loss given the

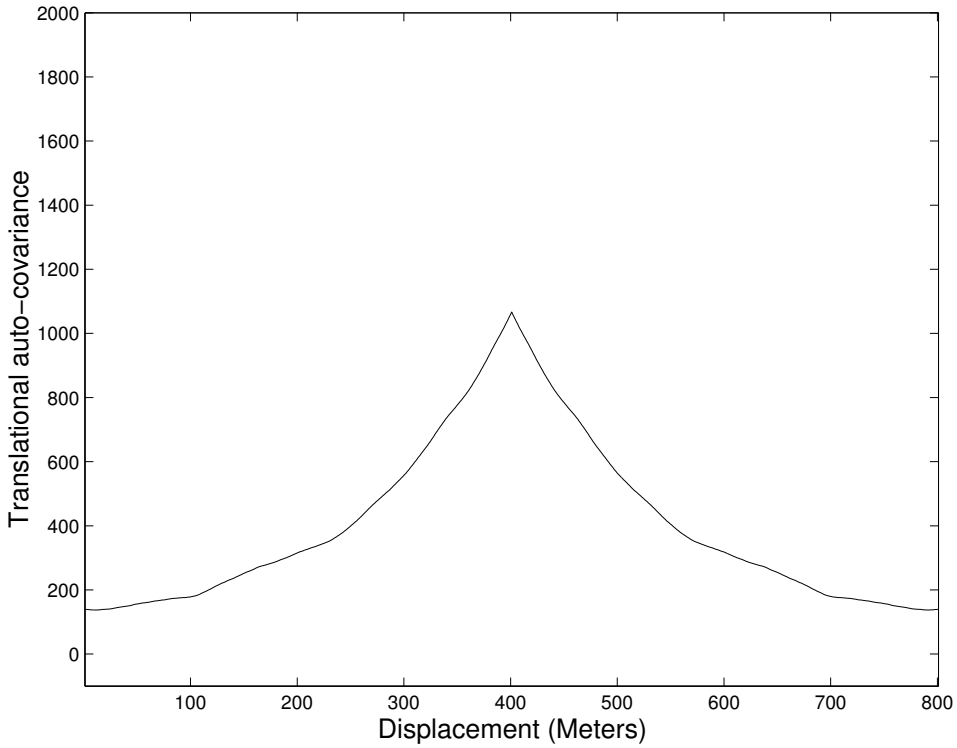


Figure 6.5: Circular Trajectory Corresponding to Item 4.

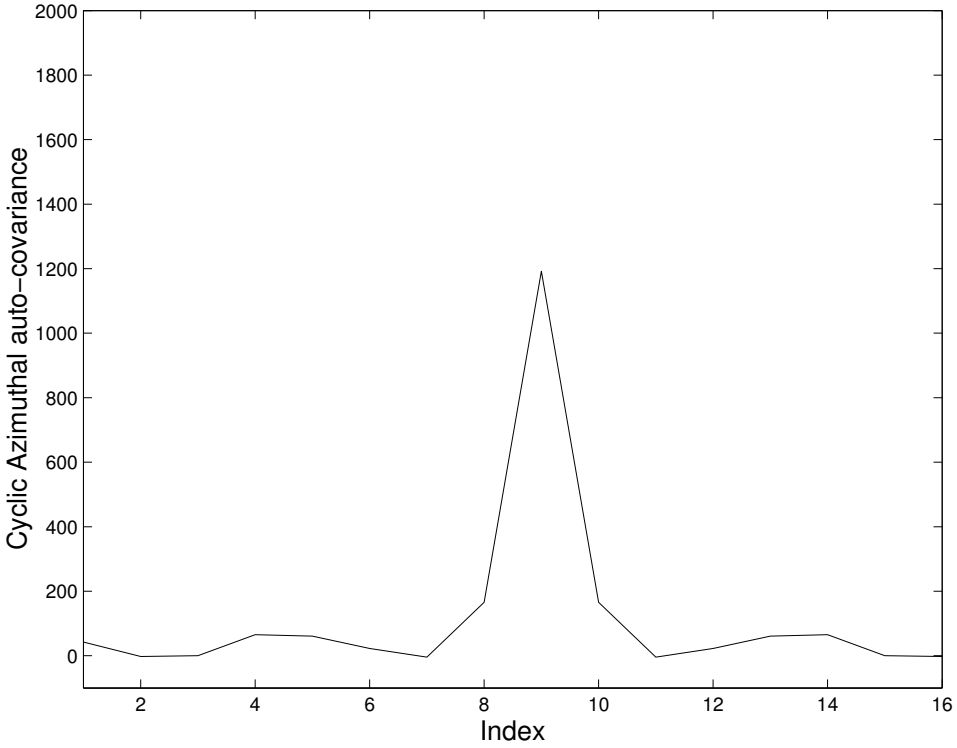


Figure 6.6: Azimuthal Autocovariance Corresponding to Item 4.

height of both antennas as well as the range between the antennas. This model provides an explanation for why there seems to be a change in the path loss exponent as a function of range as seen in [Rap96], Figure 11. The reason being that there is a transition between a free-space model and the plane-earth model at some frequency-dependent range or inflection-point. The inflection-point where the path loss exponent changes from $2^{nd}$ order to $4^{th}$ order is approximately $r > \frac{2\pi h_t h_r}{\lambda}$.

The basis for the shadowing model was work cited in [Ail02]. Both the old and new models are based on the notion that a return to positional pairings should result in the same shadowing loss. This is not the case with simulations which select shadowing from the lognormal distribution alone or generate it from a random position process. Additionally, we have incorporated into the our model an azimuthal correlation to the shadowing. This azimuthal correlation provides that signals arriving from angles that are closely spaced will have a highly correlated shadowing factor.

We performed a number of demonstration runs and plotted the results in Section 6.3.2. These demonstration runs included three runs having the antennas at fixed (but different for transmitter versus receiver) with varying range, one scenario having a circular trajectory which demonstrated the repeatability of the shadowing model, and two plots demonstrating the translational and azimuthal autocovariance.

Finally, to complete the suite of simulation models for shadowing and path loss, an additional area of study would be to determine a shadowing model that allows for the wave-guide effects. This effect is sometimes produced by obstacles confining the signal in a direction pointing toward the receive antenna and effectively results in a gain rather than the usual shadowing loss.

# CHAPTER 7

# Conclusion

This thesis has focused on two intersecting themes. The first was concerned with the modelling of the wireless channel impulse response (CIR). The emphasis was on deriving models of the CIR from a phenomenological perspective. That is, we began each model with a description of the physical underpinnings and proceeded to derive our models as directly as possible from their physical roots. The second theme of this thesis considered the effect of these models on several equalization strategies. The strategies considered were OFDM, diversity combining for a RAKE receiver, and MLSE (by sequential detection).

## 7.1 Contributions

1) We derived a new channel model for the air-to-ground (AtG) communications context. Adaptation of the original FIR model structure implies that the FIR coefficients are simply unknown constants to be estimated. The pattern of parameter evolution in the FIR model is intrinsically unpredictable. Our new model of this environment incorporates an element (one element for each channel tap) which allows us to extrapolate (predict) the complex channel coefficients in time. This element simply expresses the phase-rate-of-change for each channel coefficient.

2) To complement the model derived earlier we developed an extended Kalman

filter (EKF) to jointly estimate the channel taps along with the phase-rate-of-change elements. In conjunction with equalization (by inversion of the matrix $C_i = C_n H_i C_p$) we demonstrated that little SNR loss was incurred (assuming static parameters).

3) Noting the complexity of channel estimation and equalization using the EKF and equalization by matrix inversion, we then derived a performance measure for conventional OFDM based on our AtG channel model. The particular performance measure we obtained measures the average SINR (over all subchannels) for a particular input SNR.

4) Noting that a trade-off exists between inter-carrier interference (ICI) and sub-carrier bandwidth (which is controlled by selection of the number of sub-carriers), we obtained an expression to assist in optimizing throughput utilizing the previous performance measure. Our throughput expression yields the throughput obtainable for a particular input SNR, number of sub-carriers, and cyclic prefix length.

5) Recognizing that the Suzuki distribution only addresses the distribution of an impulse having a particular mean path loss, we leveraged on this fact to obtain the distribution of impulses within the CIR over a mean path loss range.

6) Since this distribution only exists in integral form, we obtained a simplified form under the assumption of a sufficiently large shadowing variance. Using published empirical data, we computed best-fit parameters for this new distribution and showed that it provides a better fit than other "popular" distributions such as the lognormal.

7) Utilizing results from the field of order statistics we derived the distribution for the sum of $m$ largest of $n$ random variables ($m < n$). Using similar arguments we also obtained the distribution of SINR of a RAKE MRC combiner.

8) We applied the sum-of-largest result to a RAKE receiver analysis problem using MRC combining to obtain "outage" performance curves (one curve corresponding to a particular number of RAKE fingers). We did this for both the exponential and (the more realistic) lognormal basis distributions. We concluded from this comparison that using the traditional exponential basis distribution leads to an optimistic result of approximately two dB.

9) Some researchers have obtained results that indicate the existence of so-called "worst-case" CIR for a particular channel length which result in very poor MLSE equalization performance. We showed by simulation that these worst-case-performance channels are so infrequent as to be not worth considering. Our simulation showed that only seven percent of channel realizations have $d^2_{free}$ less than the total channel energy. Of those channels with $d^2_{free}$ strictly less than the total channel energy, the vast majority suffered less than two dB loss.

10) We obtained a new path loss model that smoothly transitions between the Friis free-space and the 2-ray plane-earth path loss models as a function of range, carrier frequency, and antenna height.

11) We developed a program for simulating the total power loss for a narrow-band system. Shadowing losses were simulated using a synthesized terrain which provides a more true-to-life simulation than utilizing random lognormal fading simulation. We also included our new path loss model in the simulation program. Rayleigh fading was not included in the present simulation but could easily be generated using the usual statistical approach.

## 7.2 Suggestions for Future Research

1) The analysis and simulation we performed of OFDM performance in the high-mobility AtG environment was predicated on an implicit assumption of zero scattering near the ground vehicle. As a result of this assumption the channel tap gain and phase rate-of-change parameters were static. This assumption leads to an optimistic performance assessment of the EKF channel estimation. In order to arrive at a more realistic conclusion about the EKF channel estimation performance, it is necessary to incorporate a scattering simulation. The scattering simulation could simply involve a random complex gain (taken from a Gaussian distribution) applied to each channel tap. Simulation methods presently exist which model the time-evolution of this gain based on ground vehicle velocity.

2) In the AtG environment, there is a tendency for the CIR to be sparsely populated by impulse clusters. Attempting to adapt the entire CIR in such situations may be unadvisable since the convergence rate may be quite slow for such a lengthy CIR. An area of possible inquiry involves determining computationally efficient methods for adapting the few "active" (non-zero) CIR taps in this environment. One method that deserves enquiry is to probe the channel with a "comb" filter. That is, the comb can be used to identify the regions in the CIR where energy is concentrated and subsequently allocate additional taps in these regions for adaptation. Although this general topic has received some attention in the literature, the specific approach mentioned here has not.

3) An enhancement to the shadowing model could be realized that not only accounts for loss due to diffraction attenuation but gain due to the wave-front confinement that also exists in realistic environments.

4) By implementing Rayleigh fading into our total power loss simulation we could

utilize the result to compare the performance of several power-control algorithms. Power control algorithms need to be able to detect a change in long-term fading while not adapting too quickly to the short-term fades.

5) In this thesis we applied order statistics to the characterization of the CIR. There are many other applications to which order statistics could be applied. One application is in this area of OFDM modulation. In particular, order statistics could be applied in the study of the distribution of peak power. The knowledge of such a distribution might be useful in the design of power amplifiers due to the linearity issues involved. For instance, rather than design for worst-case power peaks, it might be acceptable to design according to an "outage-rate" threshold. Order statistics could also be applied in the study of peak power consumption of VLSI digital circuits. Hardware acceleration of algorithms is often realized through the parallelization possible using custom ASICs. For some applications, power consumption within a single algorithmic block might be described as a random variable having a particular distribution. If the other blocks in the ASIC do not operate in a coordinated fashion with respect to one another (their algorithmic processes are not synchronized), then we have the beginnings of a series of order statistics problems.

# References


[AC98] Leke Achankeng and John M. Cioffi. "Impact of imperfect channel knowledge on the performance of multicarrier systems." In *Proc. IEEE International Conference on Communications (IEEE ICC GLOBECOM '98)*, volume 2, pp. 951–955, Piscataway, NJ, November 1998.

[Ail02] Vishal Ailawadhi. *Mobility Issues in Hybrid Ad-Hoc Wireless Sensor Networks*. PhD thesis, University of California, Los Angeles, Los Angeles, California, May 2002.

[AM] John Anderson and Seshadri Mohan. *Source and Channel Coding*, chapter 6.

[BM96] Nevio Benvenuto and Rossano Marchesani. "The Viterbi Algorithm for Sparese Channels." *IEEE Transaction on Communications*, **44**(3), March 1996.

[BSB97] Jan-Jap van de Beek, M Sandell, and P.O Borjesson. "ML estimation of time and frequency offset in OFDM systems." *IEEE Trans. Signal Processing*, **45**:1800–1805, July 1997.

[CP02] Hong Chen and Greg Pottie. "An orthogonal projection-based approach for PAR reduction in OFDM." *Communications Letters*, **6**:169–171, May 2002.

[CT91] Thomas A. Cover and Joy A. Thomas. *Elements of Information Theory*, chapter 3, p. 50. John Wiley and Sons, Inc., New York, 1991.

[EQ89] M. Vedat Eyuboglu and Shahid U. H. Qureshi. "Reduced State Sequence Estimation for Coded Modulation on Intersymbol Interference Channels." *IEEE Journal on Selected Areas in Communications*, **7**(6), August 1989.

[Fos98] M.J Foschini, G.J.; Gans. "On Limits of Wireless Communications in a Fading Environment when Using Multiple Antennas." *Wireless Personal Communications*, **6**:311–335, March 1998.

[Gal87] Janos Galambos. *The Asymptotic Theory of Extreme Order Statistics*, chapter 3, p. 121. Robert Krieger Company, Florida, 1987.

[Lee99] Heung No Lee. *Adaptive Diversity Combining, Equalization and Sequence Decoding for Time-Varying Dispersive Channels*. PhD thesis, Univ. of California, Los Angeles, Los Angeles, May 1999.

[LWS02] Ye (Geoffrey) Li, Jack H. Winters, and Nelson R. Sollenberger. "MIMO-OFDM for Wireless Communications: Signal Detection With Enhanced Channel Estimation." *IEEE Trans. Commun.*, pp. 1471–1477, September 2002.

[MGB74] Alexander M. Mood, Franklin A. Graybill, and Duane C. Boes. *Introduction to the Theory of Statistics*, chapter 3, p. 121. McGraw-Hill, Inc., New York, 1974.

[Moo94] Paul H. Moose. "A Technique for Orthogonal Frequency Division Multiplexing Frequency Offset Correction." *IEEE Trans. Commun.*, **42**:2908–2914, October 1994.

[Pap84] Athanasios Papoulis. *Probability, Random Variables and Stochastic Processes*, chapter 5, p. 95. McGraw-Hill, Inc., New York, 1984.

[PH97] Ramjee Prasad and Shinsuke Hara. "An Overview of Multi-Carrier CDMA." *IEEE Commun. Mag.*, pp. 126–133, December 1997.

[Pot97] Gregory Pottie. "Low-Latency Sequential Decoding." In *1997 IEEE International Symposium on Information Theory*, p. 499, Ulm Germany, July 1997.

[Pro95a] John G. Proakis. *Digital Communications*, chapter 10, p. 601. McGraw Hill, Boston, MA, third edition, 1995.

[Pro95b] John G. Proakis. *Digital Communications*, chapter 10, p. 583. McGraw Hill, Boston, MA, third edition, 1995.

[Pro95c] John G. Proakis. *Digital Communications*, chapter 14, p. 760. McGraw Hill, Boston, MA, third edition, 1995.

[Pro95d] John G. Proakis. *Digital Communications*, chapter 10, p. 601. McGraw Hill, Boston, MA, third edition, 1995.

[Rap96] Theodore Rappaport. *Wireless Communications*, chapter 4, pp. 159–172. Prentice Hall, Inc., New Jersey, 1996.

[Say00a] Ali H. Sayed. *Adaptive Filtering*, chapter 7, p. 377. unpublished, Westwood, CA, 2000.

[Say00b] Ali H. Sayed. *Linear Estimation*, chapter 9, p. 340. Prentice Hall, Upper Saddle River, NJ, 2000.

[SC97] T.M. Schmidl and D.C. Cox. "Blind synchronisation for OFDM." *Electronics Letters*, **33**:113–114, January 1997.

[Sim90] Stanley J. Simmons. "Breadth-First Trellis Decoding with Adaptive Effort." *IEEE Transaction on Communications*, **38**(1), January 1990.

[SK95] Michael Schnell and Stefan Kaiser. "Diversity Considerations for MC-CMDA Systems in Mobile Communications." In *Proceedings of ISSSTA'95 International Symposium on Spread Spectrum Techniques and Applications*, pp. 131–135, Mainz, Germany, September 1995.

[SM00] Heidi Steendam and Marc Moeneclaey. "Sensitivity of orthogonal frequency-division multiplexed systems to carrier and clock synchronization errors." *Signal Processing*, **80**:1217–1229, July 2000.

[ST99] Yi Sun and Lang Tong. "Channel Equalization Using One-Tap DFE for Wireless OFDM Systems with ICI and ISI." In *Proc. of 1999 2nd Workshop on Signal Processing Advances in Wireless*, pp. 146–149, Annapolis, MD, May 1999.

[Suz77] Hirofumi Suzuki. "A Statistical Model for Urban Radio Propagation." *IEEE Trans. Commun.*, **25**:673–680, 1977.

[Tur72] G. L. Turin. "A Statistical Model of Urban Multipath Propagation." *IEEE Trans. Veh. Technol.*, **25**:1–12, February 1972.

[WC96] Richard Wesel and John M. Cioffi. "Fundamentals of coding for broadcast OFDM." In *Conference Record of The Twenty-Ninth Asilomar Conference on Signals, Systems and Computers*, volume 1, pp. 2–6, Piscataway, NJ, November 1996.

[WE71] S. B. Weinstein and P. M. Ebert. "Data transmission by frequency-division multiplexing using the discrete Fourier transform." *IEEE Trans. Commun. Technol.*, pp. 628–634, October 1971.

[Wes99] Richard D. Wesel. "Reduced Complexity Trellis Code Transfer Function Computation." In *Comunication Theory Mini-Conference at ICC 1999*, pp. 37–41, June 1999.

[Yac93] Michael David Yacoub. *Foundation of Mobile Radio Engineering*, chapter 3. CRC Press, Boca Raton, Florida, 1993.

[YL00] H. Jacobsson Yinggang Li, Harald Jacobsson and Thomas Lewin. "SiGe Analog ICs for Applications up to 60 GHz." In *2nd International Conference on Microwave and Millimeter Wave Technology, 2000*, pp. P20–P23, September 2000.

[YM91] Parviz Yegani and Clare D. McGillem. "A Statistical Model for the Factory Radio Channel." *IEEE Trans. Commun.*, **39**:1445–1454, 1991.

[YSB04] Kung Yao, Marvin K. Simon, and Ezio Biglieri. "A Unified Theory on Wireless Communication Fading Statistics based on SIRP." In *Fifth IEEE Workshop on Signal Processing Advances in Wireless Communications*, July 2004.